ANALYSIS OF 2x2 BRAIDED COMPOSITES

A Thesis

by

DEEPAK GOYAL

Submitted to the Office of Graduate Studies of
Texas A&M University
in partial fulfillment of the requirements for the degree of

MASTER OF SCIENCE

August 2003

Major Subject: Aerospace Engineering

ANALYSIS OF 2x2 BRAIDED COMPOSITES

A Thesis

by

DEEPAK GOYAL

Submitted to Texas A&M University
in partial fulfillment of the requirements
for the degree of

MASTER OF SCIENCE

Approved as to style and content by:

John D. Whitcomb
(Chair of Committee)

Junuthula N. Reddy
(Member)

Ozden O. Ochoa
(Member)

Walter E. Haisler
(Interim Head of Department)

August 2003

Major Subject: Aerospace Engineering

ABSTRACT

Analysis of 2x2 Braided Composites. (August 2003)
Deepak Goyal, B.E. (Hons.), Panjab University, Chandigarh, India
Chair of Advisory Committee: Dr. John D. Whitcomb

Textile composites can be tailored to meet specific thermo-mechanical requirements for structural applications. The focus of this research is on 2x2 biaxial braided composites since they have good stiffness and strength properties. Moreover, they have potentially better impact and fatigue resistance than laminated composites. Along with good properties, they have a reduced manufacturing cost because much of the fabrication can be automated. In order to exploit these benefits, thorough understanding of the effect of various factors on their material behavior is necessary.

Obtaining effective mechanical properties is the first order of concern in any structural analysis. This work presents an investigation of the effect of various parameters like braid angle, waviness ratio, stacking sequence and material properties on the effective engineering properties of the 2x2 braids. To achieve this goal, three dimensional finite element micromechanics models were developed first. Extensive parametric studies were conducted for two material systems: 1). Glass (S2) fiber / epoxy (SC-15) matrix and 2). Carbon (AS4) fiber / Vinyl Ester (411-350) matrix. Equivalent laminated materials with angle plies and a resin layer were also analyzed to compare the difference in predictions from the full three dimensional finite element analysis of the 2x2 braided composites.

A full three-dimensional stress state exists in braids even for very simple loading. In order to locate the potential damage spots, the stress distributions in both the matrix and the tows were predicted. The effect of braid angle on location and magnitude of peak stresses was determined.

To my parents, for their love, patience and sacrifices

ACKNOWLEDGEMENTS

First of all, I am thankful to GOD for HE has helped me so much in keeping the right attitude and always being there in tough times.

I wish to express my deep sense of gratitude to my advisor Dr. John D. Whitcomb for supporting me financially, morally and academically. Without his patience and constant guidance, this work would have never been complete. His emphasis on quality adds a great deal to the learning process.

I am thankful to Dr. Xiaodong Tang for being such a nice friend and mentor. I was very fortunate to get a chance to work with him. I will always be indebted to him for his tremendous help throughout this research and for the life lessons that help me be a better person. I also acknowledge his help allowing me to use several in-house computer codes.

I would like to express my gratitude to Dr. J.N. Reddy and Dr. Ozden O. Ochoa for serving on my thesis committee and for providing the valuable time from their busy schedules.

I am thankful to Dr. Ajit Kelkar and Jatindra Tate from North Carolina A&T University for providing the experimental results for this work.

My sincere thanks also go to Aerospace Engineering Department staff, especially Ms. Karen Knabe who is a wonderful person and Ms. Donna Hollick, for their kind help during my graduate studies.

I appreciate our research team members Dr. Jae Noh, Jongil Lim and Julian Varghese for providing a conducive environment for this research work. I am also thankful to all of my friends, especially Nishu, Atul, Sukhpreet, Chandan, Munish, Jatin, Paras and Sudharsan for their moral support at times whenever I suffered from nostalgia. I am thankful to all the people who have directly or indirectly helped me accomplish whatever I have.

Finally I wish to express my sincere appreciation to my mom, dad and sister for their unlimited support, love and sacrifice for making it possible for me to pursue graduate studies in US.

This work is based on research supported by Federal Aviation Administration (FAA) under Grant No. DTFA03-01-C00033. Any opinions, findings, recommendations or conclusions expressed herein are those of the author and do not necessarily reflect the views of the FAA.

TABLE OF CONTENTS

Page

LIST OF TABLES

LIST OF FIGURES

1. INTRODUCTION

1.1 Overview

Composite materials have found a wide variety of applications in the aerospace, automobile, sports and marine industries for the past three decades because of their high specific strength and stiffness as compared to conventional metals/alloys. But they have the limitations of high cost, low damage tolerance and impact resistance. Textile composites are the potential materials to overcome these limitations. They have good impact, crash and fatigue resistance and moreover, the textile industry has developed fully over the years for the cost-effective manufacturing of a wide variety of textile preforms [1].

There are a number of textile manufacturing techniques available to make fiber preforms. The dominant forms of textile manufacturing techniques can be classified into braiding, weaving and knitting. They all share the characteristic that fiber yarns (or tows- the terms will be used interchangeably in the text) are interlaced to create a preform that is impregnated with resin to make a composite laminate structure. Figure 1.1 shows some of the possible weave architectures that were developed in [2-3]. Figure 1.2 shows two types of braids: a 2x2 biaxial braid and a 2D triaxial braid [4].

Figure **1.3** illustrates a knitted tow architecture. References [5-6] show some knit architectures. Both the weaves and the braids can exhibit high performance. The extreme amount of undulation in the knit makes for a very flexible preform, but the performance tends to be low.

1.2 Classification of textiles

Apart from classifying on the basis of manufacturing technique, textile composites

---

This thesis follows the style and format of *Journal of Composite Materials*

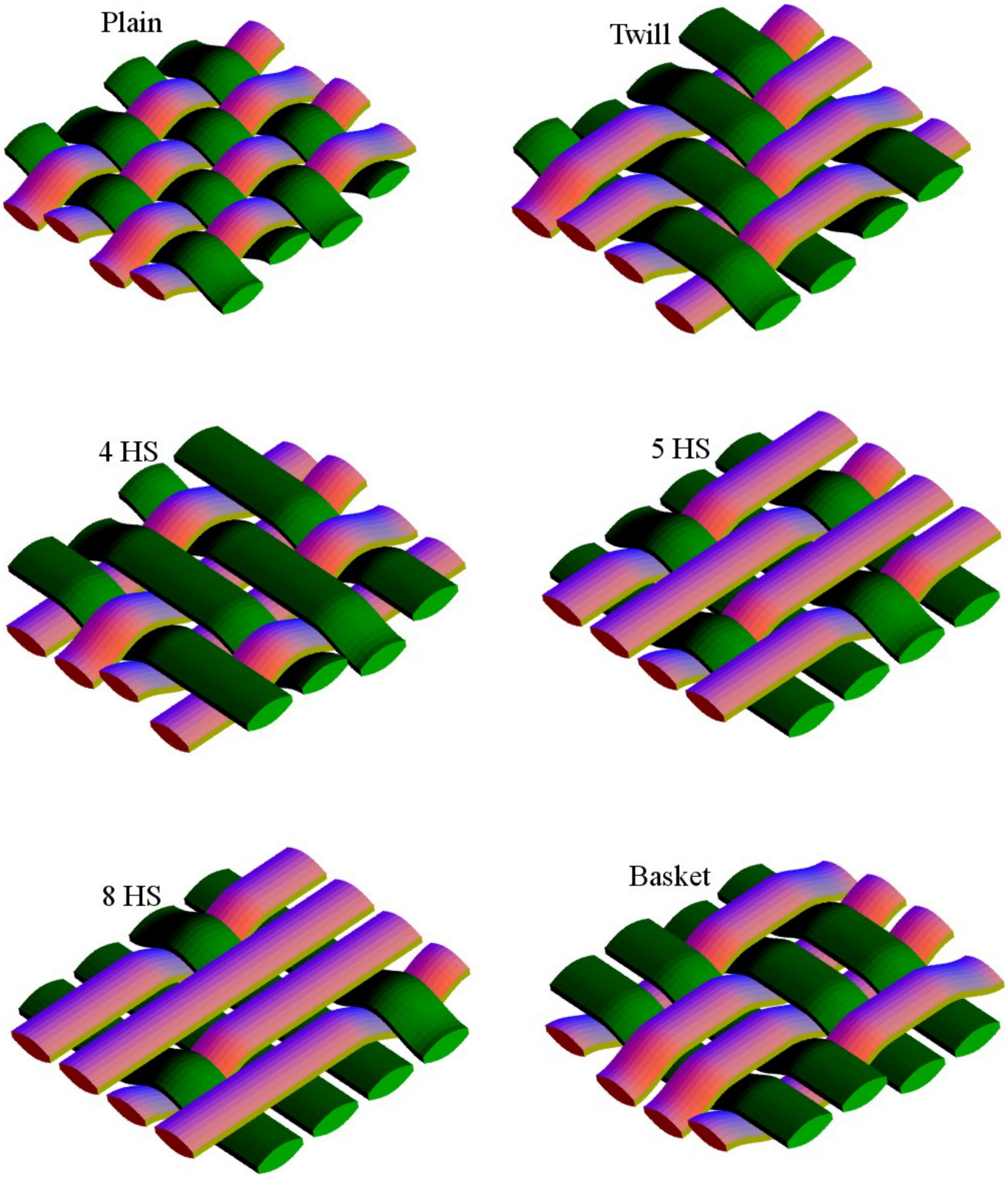

Figure 1.1. Schematics of woven composites (without matrix pockets)

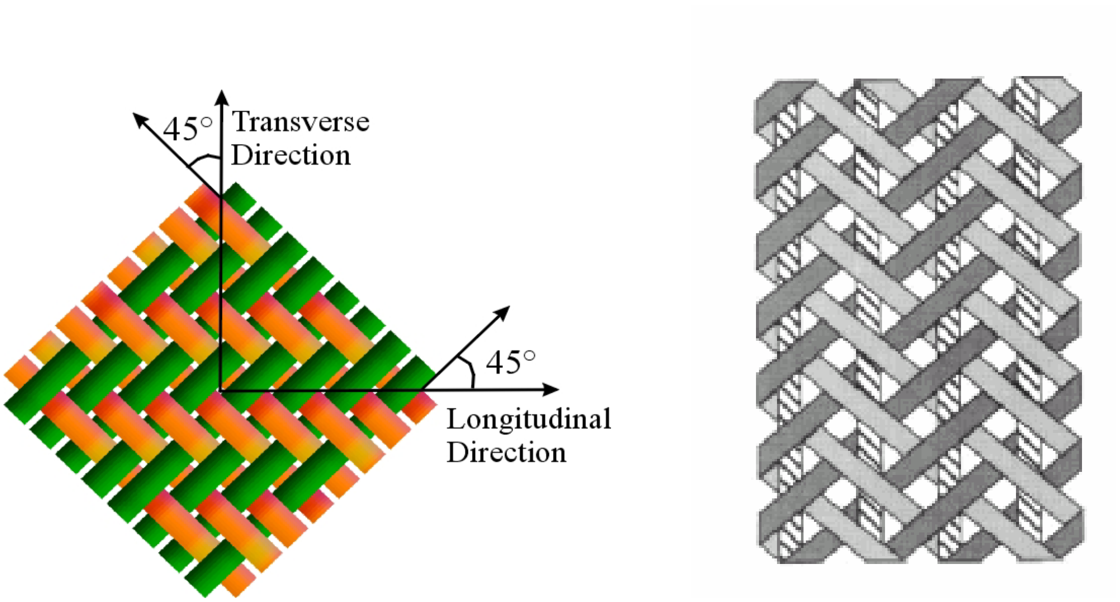

(a) 2x2 biaxial braid (b) Triaxial braid [4]*

Figure 1.2. Schematics of braids. (*Reprinted from composites science and technology, vol 60, no. 5, 2000, Byun et al., "The analytical characterization of 2-D braided textile composites," page no. 706, Copyright (2000), with permission from Elsevier.)

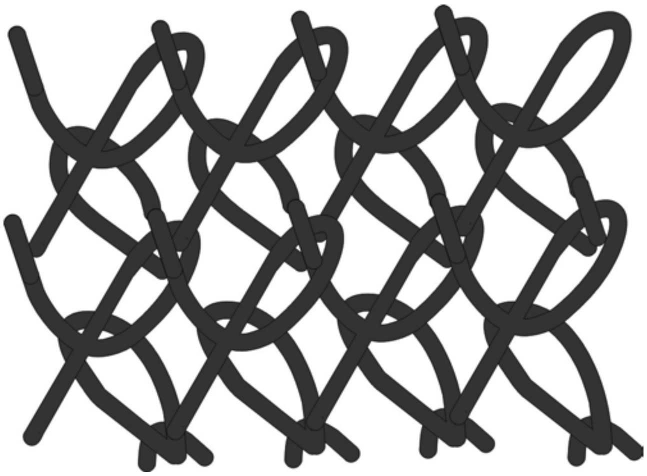

Figure 1.3. Schematics of knitted tows

can further be classified into 2-D or 3-D composites on the basis of preform geometry. According to the definition of Cox and Flanagan [7], a textile structure is classified into a 2-D or 3-D category based on the fact that it can transport a considerable amount of load (more than that carried by matrix alone) in two or three mutually perpendicular directions. A broad classification of textile composites is shown in Figure 1.4 [7]. Our area of interest, in this research, is braids. Braids can be 2-D or 3-D. In 2-D braids, we have 2-D biaxial braid or 2-D triaxial braid. A biaxial braid has braid yarns running along two directions (+θ and –θ), whereas a triaxial braid has these plus an additional yarn in the longitudinal direction.

1.3 Applications of 2x2 braids

The focus of this research is on 2-D biaxial braided composites as they have good stiffness and strength properties, and have potentially better fatigue and impact resistance than laminated composites [8]. Another benefit is in manufacturing cost reduction due to part count reduction. Because of these potential benefits, they are being considered for various applications like use in primary and secondary aerospace structures. These material systems are gaining popularity, in particular for the small business jets, where the Federal Aviation Administration requires take off weights of 12,500 lb or less. Braid is currently the reinforcement choice in components that are used in variety of market applications [9]. Examples include:

- Aerospace – Braids have found many aerospace applications. Some examples are aircraft propeller blades, missile nose cones, aircraft engine containment, aircraft engine stator vanes, self-lubricating bearings, control surfaces, aircraft ducting and tubing and satellite components. Some of these are shown in Figure 1.5.
- Industrial – With decreasing cost, braid is finding extensive use in industrial applications. It is being used as the primary load bearing reinforcement in many components. Applications include automobile crossbeams, automobile air bags and commercial furniture, restraint devices, industrial rollers, lamp and utility

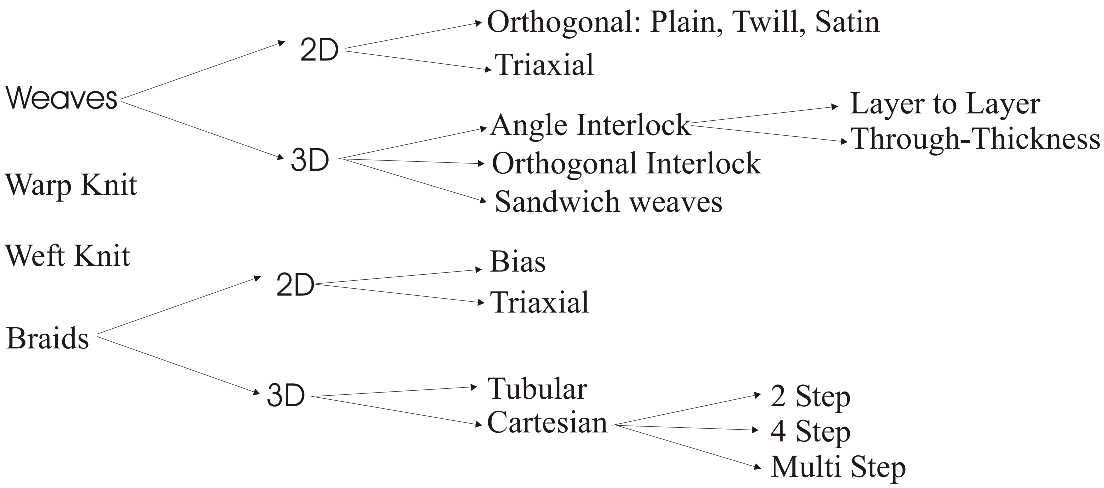

Figure 1.4. Classification of textiles [7]

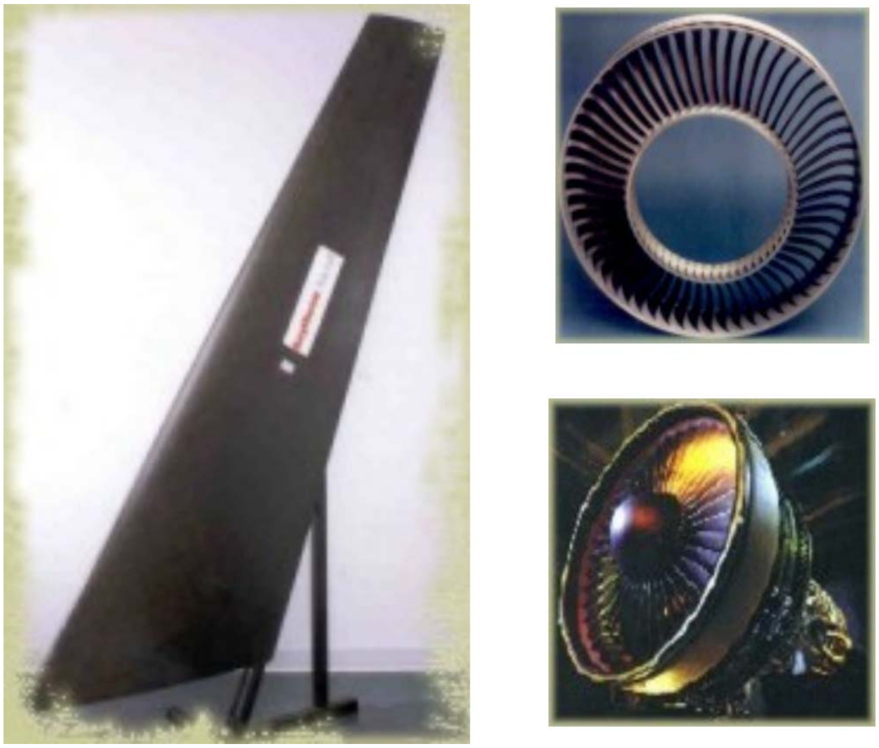

Figure 1.5. Application of braided composites in aerospace.

(Horizontal stabilizer*, jet engine vane*, jet engine containment*) [9]

*Reprinted with permission from http://braider.com/uses.html by A&P Technology Inc., 2000. Available at http://www.braider.com, copyright year 2000 by A&P Technology.

poles. It is a partial reinforcement in structures like shipping containers and boat hulls.

- Medical – In medical applications, braids are being used to make parts like prosthetic limbs and orthotic braces, surgical devices like endoscopes and catheters and implantable devices such as splints and stents.
- Recreational – Many recreational equipments also are using braided reinforcements. Some examples are wind surfing masts, snow boards, water skis, snow skis, boat hulls, hockey sticks, golf shafts, wake boards, sail masts, bicycle components, baseball bats, tennis and other racquets, and kayak and canoe paddles.

1.4 Advantages of braids

The advantage of the braids is the result of continuous fibers and the mechanical interlacing in their geometry [9]. This interlacing complicates the stress analysis thereby making it more difficult to design with confidence. A critical part of the work proposed herein will be identification of the critical complexities that must be considered, which will require an integrated experimental and analytical investigation. Some of the advantages [9] of the braids are presented here:

1. The components such as fan blade containment, that need good impact resistance, use braided structures. Good impact resistance of braids comes from the fact that braids have efficient distribution of load. In an impact loading event, all the fibers are involved so braids absorb a great deal of energy during failure.
2. Braid is the reinforcement choice for aircraft propellers and stator vanes in jet engines due to its better fatigue life. The microstructure of braids is such that it gives much better fatigue resistance. Braid fibers are coiled into a helix and are interlaced. When the structure is exposed to high cycle fatigue, the cracks propagate through the matrix of the filament wound structure. But due to the mechanical interlacing, cracks

propagation is arrested at the intersection of the yarns. This increases the fatigue life considerably.

3. As braid has good properties to bear torsional loads, it is a very good choice for parts like drive shafts and other torque transfer components. The reason is that the braids have good interlaminar properties. Although the adhesive material between the reinforcing layers is the same as other reinforcement products, the braid layers move together thereby making it difficult for cracks to initiate and propagate between layers.

4. There are wide varieties of fibers that can be braided. The fibers like aramid, carbon, ceramics, fiberglass, natural fibers, synthetic fibers, and thermoplastics can all be braided. All it needs is that the fiber should have a reasonable degree of flexibility and surface lubricity to be able to be economically braided.

5. Different forms and architectures of braids are available for different applications. To fit over applications involving rods (Like a connecting rod in an automobile), sleevings or tubes of braids are available. To use in sheet form, flat tapes are available.

6. For use in different applications, the braids are available in the wide range [9] like:
    - The biaxial and triaxial sleeves from 0.5" to 48" in diameter.
    - Biaxial and triaxial flat tapes up to 36" wide.
    - Braided slit fabrics (broad goods) can be produced up to 8' wide
    - Braid angles for sleevings and tapes can range from approximately 15° to 75°.
    - Areal weights can range from 0.5 to 200 ounces per square yard (17 to 6770 gm/m^2)
    - Overbraiding can be done on objects up to 8' in diameter and 15' in length.

7. Braid's structure is flexible. In a single component the same braid structure can have varying braid angle. For example, in the hockey stick made by braid, the braid angle changes at different cross-sections of the stick. Braid can expand open to fit over

molding tools and can accommodate straight as well non-uniform and irregular cross-sections.

8. As compared to other reinforcement choices, braid is cost competitive once an overall cost analysis is performed. Since it takes the exact shape of the part it is reinforcing, a lot of intermediate steps like cutting, stitching are eliminated. This reduces the scrap and labor hours and allows repeatability.
9. Braids have good balance in off-axis properties and are well suited for complex curved shapes as they have good drapability [10].

Although 2-D braided composites have numerous advantages, they have some disadvantages also. For example, they have size limitation due to machine unavailability and have low out-of-plane properties [10]. Still, braided composites have a wide range of applications and advantages. To exploit these materials fully, micromechanics analyses are required to obtain the effective engineering properties. As the geometry of textile composites is complex, a three-dimensional stress state exists at every point in the microstructure. Micromechanics analyses are also required to predict these complex stress states, which can give the information about potential damage spots in the microstructure during loading.

1.5 Literature review

Many researchers have developed models for textile composites. References [6, 7, 11-13] give an overview of the different models. These models try to predict the effective thermo-mechanical properties and do failure analysis. But, because of multiple scales involved and complex tow architecture, modeling of textiles has always been challenging.

It should be noted that since the precise control of fiber orientation and position is not possible for unidirectional composites, the geometry is defined in an average sense, whereas textile manufacturing process precisely determines the yarn architecture.

Hence textiles provide more opportunities to tailor the architecture to specific needs and their modeling should be done as close to reality as possible [13].

A lot of literature has been written on the analysis of textiles. Most of the research has been focused on weaves because of their relative geometric simplicity. It can be noted that away from boundaries, there exist some similarities in geometry of weaves and braids. For example, a 1x1 braid with braid angle of ±45° is similar to a plain weave and a 2x2 braid with braid angle ±45° is similar to a twill weave. However the weaving and braiding manufacturing processes are different, which subjects the tows to different manipulations, so details of the tow architecture can be different. Because of the similarities, the literature review herein will include the research done on braided as well as woven composites.

Many models have been proposed for analysis of textile composites. Some researchers have proposed simple analytical models and the others have full three-dimensional finite element (FE) models. All of them involve simplifying assumptions about geometric modeling of the tow path and boundary conditions. These models vary in terms of accuracy of the assumed displacement or stress field.

Ishikawa and Chou were two of the pioneers in the analysis of textile composites [14-15]. They did a good deal of work on the thermo-mechanical modeling of plain weaves. They used the classic laminate theory as a basic tool for developing their models. They developed three one-dimensional analytic models known as *the mosaic model, the 1D crimp model (also known as fiber undulation model) and the bridging model*. These models considered the undulation of yarns only in the loading direction and did not take the shape of the actual yarn cross-section into considerations. These models provide a good understanding of the basic aspects of the mechanical properties of woven composites.

Naik, Shembekar and Ganesh [16-17] have extended the 1-D models of Ishikawa and Chou into 2-D elastic models that take into account the undulation in both the warp and weft directions and the cross-section shape of the yarn. They have developed what they called *the parallel-series (PS) or the series-parallel model (SP)* depending on assembling the elements first in series or parallel. In both, the unit cell is divided into slices along and across the loading direction. These models are limited to uniaxial tensile loading only and do not provide the answer to when and why *SP* or *PS* models should be used.

Hahn and Pandey [18] extended the above 2-D models to a *3-D thermo-elastic model* that models the undulation of fibers in both directions along with a sinusoidal cross-section shape of the yarns. The condition of isostrain was assumed, whose accuracy still remains to be verified through experiments [19].

R Naik [20] developed an analysis tool called TexCad that calculates the 3-D effective properties by a yarn discretization scheme that again assumes iso-strain condition.

We see that many of the above-mentioned models are based on the extension of the laminated plate theory. Although there are many versions, they all basically consider the textile mat to consist of a collection of laminated plates that are arranged in series, in parallel, or in some combination of these. The assumption of isostress or isostrain conditions is widely used to simplify the homogenization process [20]. Increasingly, there has been full 3D modeling of the tow architecture [21-31]. Many researchers have reported finite element based numerical models as they make fewer assumptions than the analytical models and the geometry of the towpath can be modeled more faithfully. A review of the finite element based numerical models is given below.

Paumelle et al. [21-22] have used the finite element method to get all the 3-D effective properties by applying the different loading conditions and the periodic boundary conditions on the model. But his model needs large computation power and verification of model geometry.

Blackketter [23] developed an incremental iterating finite element model that had the capability to model non-linear constitutive behavior for plain-weave graphite/epoxy composites. A stiffness reduction method was used to model damage initiation and propagation.

Whitcomb et al. [2, 24-27] have developed finite element tools to analyze woven composites. Their work is not restricted to the plain weave only. They have done a comparative study for different kind of weaves like plain weave, twill weave, 4HS, 5HS and 8HS etc. It was made possible to reduce the model size to a considerable low value by exploiting the geometric and material symmetries [28-29]. The effect of the cross-section shapes and stacking sequence of mats was also analyzed.

Recently a *complementary energy model* [30-31] for the 2-D woven composites has also been developed that tries to capture the effect of both orientation and position of the tow elements. This model uses a multilevel decomposition scheme to split the unit cell and a multistep homogenization procedure to predict elastic moduli. The principle idea is based on the principle of minimum complementary energy i.e. out of all admissible stress fields the true field is the one that minimizes the total complementary energy of the system.

There has been very little 3D analysis of anything but the plain weave composites. Whitcomb et al. [2] have developed efficient 3D models of the weaves shown in Figure 1.1. Compared to the weaves, there has not been much analysis of braids because braids tend to be more complicated than weaves because the interlaced tows are not necessarily always orthogonal (like most weaves). Moreover, most analysts that have managed to develop the 3D models of a weave have done so only for the plain weave.

Ma et al. [32] have used FEM to analyze mechanical properties of 3-D braided composites. They proposed a *diagonal brick model* that had a brick shaped element of resin with bar elements at the edges and diagonal of the brick. This model neglected the crimping of fibers at the corners of the cell.

Yang et al. [33] proposed an analytical *fiber inclination model* that was an extension of the laminate theory to predict the elastic properties of 3-D braided composites. The unit cell consisted of inclined laminate plates. It was basically an extension of the aforementioned 1-D fiber undulation model of Ishikawa and Chou [14].

The above two models do not include the geometric and processing variables in the unit cell modeling, and therefore have the inherent limitation of not being able to be used for the optimization of braided composites for structural applications.

Byun et al. [34] developed a *micro-cell* and *a macro-cell* model to calculate the elastic properties of 2-step braided composites. The micro-cell model was developed for thin specimens where average compliances were calculated based on the pointwise application of the laminate theory. The macro-cell model was for the entire cross-section and took the yarn orientation variation into consideration. Although it showed a good agreement between the predicted and experimental axial tensile modulus, shear modulus results did not match.

Recently Byun [4] developed an analytical model for the characterization of the 2-D triaxial braided composites. The elastic model utilizes the coordinate transformations and the averaging of stiffness and compliance constants based upon the volume fraction of each reinforcement and matrix material to predict all the 3-D elastic constants. Parametric studies were also conducted to investigate the effect of the braid yarn angle and the axial yarn content on the elastic properties. Although seven different models were fabricated to verify the model, experimental data was not enough to support the predictions.

A geometric model for studying the effect of geometric parameters on the mechanical properties of the 2-D triaxially braided composites was proposed by Naik et al. [35]. A repeating unit cell that consisted of the straight yarn slices was isolated. A volume averaging technique with assumptions of iso-stress and iso-strain predicted the mechanical properties. The model was based upon the yarn discretization and the volume averaging technique to predict the 3D properties of the triaxially- braided composites. This model does not take into account the geometric characteristics and moreover, the yarn discretization involves much computational work.

Yang and Chou [36] extended the crimp model of Ishikawa and Chou [14] to analyze the triaxial woven composites. Although the geometry of a triaxial weave is different from that of a braid, the method described can be readily applied to a triaxial braid.

Masters et al. [37] have developed four different models to predict the elastic moduli of braided composites: *the laminate model, the laminate model with a correction factor, the diagonal brick model and the finite element model.* The laminate model can predict only in-plane properties whereas the diagonal model based upon the rod elements oversimplifies the geometry and neglects the yarn curvature. The FE model showed the best predictions, but it involves complicated reconstruction of the geometry every time fabric geometry changes and takes a long time for calculations.

Smith and Swanson [38] utilized 3 different models: the laminated plate theory, the 3-D laminated plate theory and the fiber inclination model to predict the stiffness and biaxial failure of the triaxially-braided composites. The fiber undulation was not taken into account. It allows calculation of only in-plane properties.

D'Amato [39] proposed a finite element model for the 2-D triaxial braids that allows detailed information on stresses and deformation. The geometric model was created from the graphic information obtained by the investigations carried out by electronic microscope. The modulus (E_X) contributions due to the axial yarns, the bias yarns and due to the effect of braiding were calculated separately. It was concluded that the contribution of the axial yarns depends on their number whereas the contribution of the bias yarns (which had an angle of ±60° in their analysis) depends on the model size. In the cases analyzed, it was observed that the biggest contribution, of more than 50% was related to braiding, whereas the contribution of inclined beams was about 2-4%. Sensitivity to the geometric characteristics was also analyzed and the stress distributions were also obtained. But no experimental verification of the predicted results was provided.

Fujita et al. [40-43] used an FEM approach called *semi-microscopic approach* that discretizes the fibers with beam elements, which correspond to the real geometry of the yarns. The cohesive effect of the matrix with other beam elements is simulated. This kind of approach is used to analyze the crack evolution inside the material and for the ultimate strength calculations. They characterized the failure mechanisms of the flat-braided glass/epoxy composites under tension loading and also considered various specimens with cut/uncut edges, formed and machined holes etc.

Lots of experimental work has also been done on the mechanical performance of braided composites. It basically has been focused on measuring the strength and the stiffness, particularly for the use of validating the analytical and the numerical models.

Dadhah et al. [44] measured the mechanical properties and characterized the failure mechanisms for triaxially braided glass/urethane composites under both tensile and compressive loading.

Fedro and Willden [45] compared experimentally the mechanical performance of the 2-D triaxially braided and the 3-D braided carbon/epoxy composites with those made from prepreg materials.

Falzon [46] has conducted the tension, shear and compression tests to evaluate the mechanical performance of the 2-D braided carbon/epoxy composites. It was found that braided composites have comparable tension and compression stiffness but considerably reduced strengths due to fiber damage and the fiber tow waviness. It was revealed that the tensile strength was 20% less due to the fiber damage during the braiding process and the shear tests remain inconclusive due to the unsuitability of current test methods.

It can be seen that the mechanical characterization of braided composites has not been completed yet. Moreover, the research so far has mainly focused carbon/epoxy composites only. Comparison of failure mechanisms between braided composites and those made from conventional materials, such as prepreg tape for a wide range of braid architectures is also required [46].

In summary, a few important observations can be made from the various efforts in the field. The first is that most engineering moduli can be predicted well by quite simple analyses. The reason is that in reality, comparatively flat weaves are used and their moduli are dominated by quite simple physics. Unfortunately, the accuracy of some of the simple models appears to be a result of fortuitous cancellation of errors rather than good approximation of the physics. Whitcomb and Tang [24] showed that all of the 3D engineering moduli can be predicted quite accurately even for the very wavy weaves if the behavior of the undulated regions is described adequately. It also showed that some of the most popular approximations appear to have little physical basis.

Many researchers have made efforts to predict the elastic properties of textile composites, but compared to the achievements in modeling of 2-D woven composites or even 3-D textile composites, very little has been done in 2-D braided composites [4]. Some of the methods proposed have the limitations of use in only limited situations [39].

Although the moduli can be predicted fairly easily, prediction of the local stress states is not so easy. Figure 1.6 shows sample stress contours for the σ_{33} stress component for a 2x2 braid subjected to a uniaxial load. The stress states are fully 3D even for the simplest loading. The interpretation of these stress states is a difficult job because the stresses can be so localized that the scale is small comparative to the size of the fibers in the tow. The real tow architecture has a more chaotic geometry than the idealized textile geometry. That will further increase the complexity of the stress states.

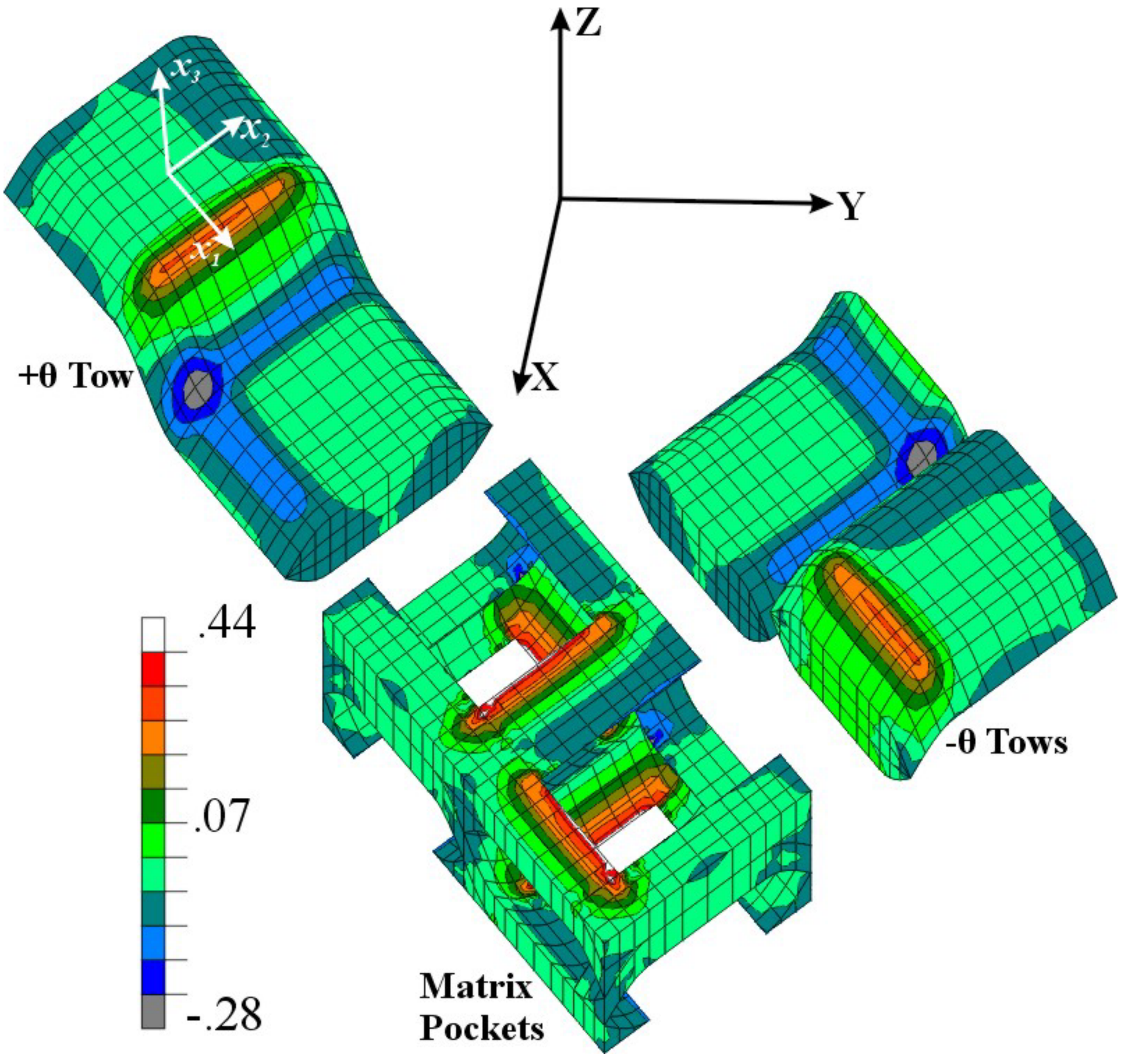

Figure 1.6. Normalized stress contours for σ_{33}

Uni-axial loading ($< \sigma_{xx} > = 1$) of ±24.75° braid (AS4/411-350) (WR=1/3)

Due to these complexities, comparatively less effort has been made to predict the failure behavior of textiles composites. There has been progress in predicting the progressive failure of woven composites. Most of the work has been done for the plain weave [20, 23, 47-51]. Detailed progressive failure analysis of braids has not been performed.

In summary, considerable progress has been made in the area of quasi-static analysis of woven composites. Relatively little has been done for quasi-static analysis of braids. Given this state of the art, in the next section, we propose the following research for the 2x2 biaxial braided composites.

1.6 Scope of research

As seen above, most of analyses have been focused on weaves and very little has been done for analyzing braids. A thorough understanding of the behavior of the 2x2 braids is required to exploit the advantages these materials offer. To achieve this, computational micromechanics analyses will be performed to predict the effective engineering properties and the three-dimensional stress state.

First of all, the finite element meshes for braids need to be generated. As parametric studies need to be conducted, we should be able to generate the meshes easily. Earlier [3], a strategy has been described for generating the finite element meshes for a wide variety of weaves using a general purpose preprocessor "*Meshweaver*". Since the 2x2 braid architecture is similar to that of the twill weave, a mapping technique [52] will be used to generate the braid meshes from the meshes of the twill weave. A description of the idealized geometry of the braid tow will be given and will be compared with the idealized geometry of the twill weave. Solid models of the braids will be generated for thorough understanding of its architecture and its effect on the effective properties and the stress distribution. In any finite element analysis, it is useful to minimize the analysis region to save computational time and computer memory. The boundary conditions will be imposed in such a way that periodicity and symmetries [29] that exist in the microstructure of the braids can be exploited to minimize the analysis region. Boundary conditions that include a number of multipoint constraints will be derived using a technique given in [29].

Obtaining effective engineering properties is the first order concern for any structural analysis. Parametric studies will be conducted to obtain effective properties. The effect of various parameters like braid angle, waviness ratio, material system and stacking sequence will be analyzed. Thus the dominant characteristics that determine the behavior of the 2x2 braids will be identified, which will be valuable in validating and evaluating simple analytical models. The effective property results produced by this 3-D finite element analysis will be compared with an equivalent laminate analysis. The reason is that the laminate theory codes are widely available and understood. It will be investigated whether the effective properties of the braids can be predicted using the laminate theory and how much error there is in doing so.

Some of the simple models like the laminate plate theory can do fairly accurate predictions of the effective properties, but they can not predict the local stress states since the stress states are very complex even for the simple loading cases. Full 3-dimensional stresses, both in the matrix and in the tows, will be predicted for various loading cases. The location and magnitude of peak stresses will be determined, which will be useful for identifying the potential damage initiation locations in the 2x2 braids.

Two material systems will be analyzed. One is made of S2 glass fibers and SC15 epoxy resin. The other consists of AS4 fibers and vinyl ester resin (311-450 epoxy, also called Derakane Momentum). The effect of the various parameters mentioned above will be compared for these two material systems. Also the stress distributions will be predicted for both the material systems. The predictions of the moduli and the Poisson’s ratio will be compared with the experimental data [53] for AS4/311-450.

1.7 Summary

Braided composites have a wide range of applications in many areas like aerospace, industry, medicine and recreation. The advantages of the braids are a result of their fiber continuity and the mechanical interlacing. To exploit the advantages that these materials offer, their mechanical behavior needs to be characterized. Not many attempts have been made to analyze the 2x2 braids. Mainly the research has been focused in the area of quasi-static analysis of woven composites and relatively little has been done for the braids because of their complex microstructure. A full three-dimensional stress state exists in braids and their stress analysis tends to be even more complicated than that of weaves. This research will be focused on the following topics:

1) Define the idealized tow architecture to analyze the microstructure of the 2x2 braids.

2) Study the effect of various parameters like braid angle, waviness ratio, tow cross-section, stacking sequence and material properties on the effective engineering properties of the 2x2 braids.

3) Compare the difference in predictions of the 3D finite element analysis and the simple 3D laminate analysis.

4) Predict the three-dimensional stress state. Determine the effect of the braid angle on location and magnitude of the peak stresses, which will be helpful in locating the potential damage spots for different braids.

2. COMPUTATIONAL MICROMECHANICS

2.1 Introduction

In this chapter, the idealized geometry of weaves and braids is discussed first. Then a mapping procedure to produce solid models of the 2x2 braids from models of the twill weave is discussed. The idealized braid tow architecture will be discussed in detail and the equations defining the tow geometry will be given. A typical finite element model used to do the analysis will be discussed. Material angle transformations will be derived and the boundary conditions for a typical model will be given. Because the twill weave and the 2x2 braid are related (and the twill is simpler), the twill weave will be discussed briefly and then the focus will be on the braid.

2.2 Idealized geometry

The textile composites have complex microstructure characterized by the tow undulation. For thorough understanding of the details of the microstructure of the textile composites, it is necessary to generate the solid models. A solid model gives the information about the microstructure of the textile under consideration. Solid models not only help in understanding the complex geometry, but they give insight in interpreting results also as will be seen in the discussion of the results. A strategy has been developed by Whitcomb et al. [3] to generate the solid models of weaves. Here, various parameters that go in the generation of the solid model of the weaves and braids are discussed.

2.2.1 Idealized geometry of weaves

The woven structure is characterized by the orthogonal interlacing of two sets of yarns called the warp and the weft yarns or tows. The weft yarns run perpendicular to the direction of the warp yarns and are also called fill yarns. Each of these yarn elements is straight for some part of the yarn and is undulated for some part. The yarn element is straight when it passes over or under another yarn and it is undulated when it passes from top to bottom of the yarn. Figure 1.1 shows different weaves with matrix pockets removed to show the geometry.

There can exist many forms of weaves, but the weaves shown in Figure 1.1 viz: the plain weave, twill weave, 4 harness satin, 5 harness satin, 8 harness satin and basket weave are the dominant forms. In all the cases the tows have both the undulated and straight regions except for the case of the plain weave with lenticular cross-section in which the entire length of the tow of both weft and warp yarns is undulated as the tow is continuously moving from top to bottom of the yarns without having any straight region. But in the case of other weaves, the yarns have some straight region before starting to undulate.

The complex microstructure produced by the fiber tow undulation of different types of weaves presents a challenge in modeling. The geometry should be modeled as accurately as possible. The idealized geometry of the weaves can be modeled using simple sine or cosine functions. To do so, first the cross-section of the warp and the fill tows needs to be modeled. The cross-section shape of a tow can be lenticular or flattened [see Figure 2.1]. The cross-section shape of the tow in the weave will actually depend on the volume fraction of the tow in the model. If the tow volume fraction is less than 2/л, then the cross-section will be lenticular, otherwise it will be flattened. The flattened cross-section leaves less space for the matrix pockets, thereby allowing more overall fiber volume fraction in the model. Tow volume fraction can be calculated using the following relation.

$$V_{fO} = V_T * V_{fT} \tag{2.1}$$

where V_{fO} is overall fiber volume fraction

V_T is tow volume fraction in the model

and V_{fT} is fiber volume fraction in the tow

Figure 2.1 shows the idealized cross-sections of the weaves. The cross-sections can be produced by using simple sine or cosine functions. For example, the cross-sections shown in Figure 2.1(a) and (b) were produced by using cosine function. Figure 2.1 (a) shows a flattened cross-section and 2.1(b) shows a lenticular cross-section. Then any of these cross-sections is swept throughout the length (the length also being defined

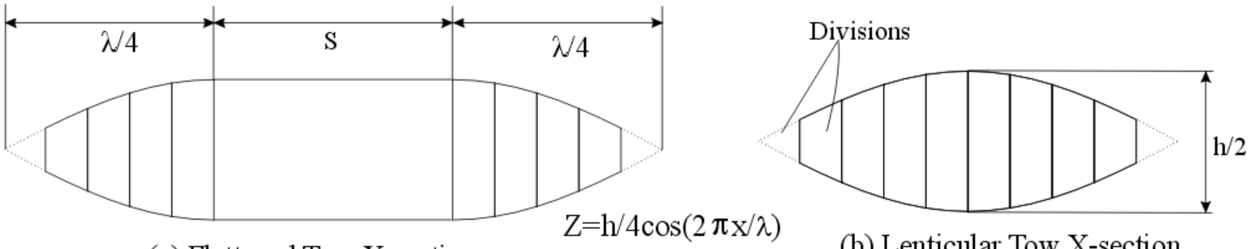

(a) Flattened Tow X-section
Tow width = λ/2 + S

(b) Lenticular Tow X-section
Tow width = λ/2

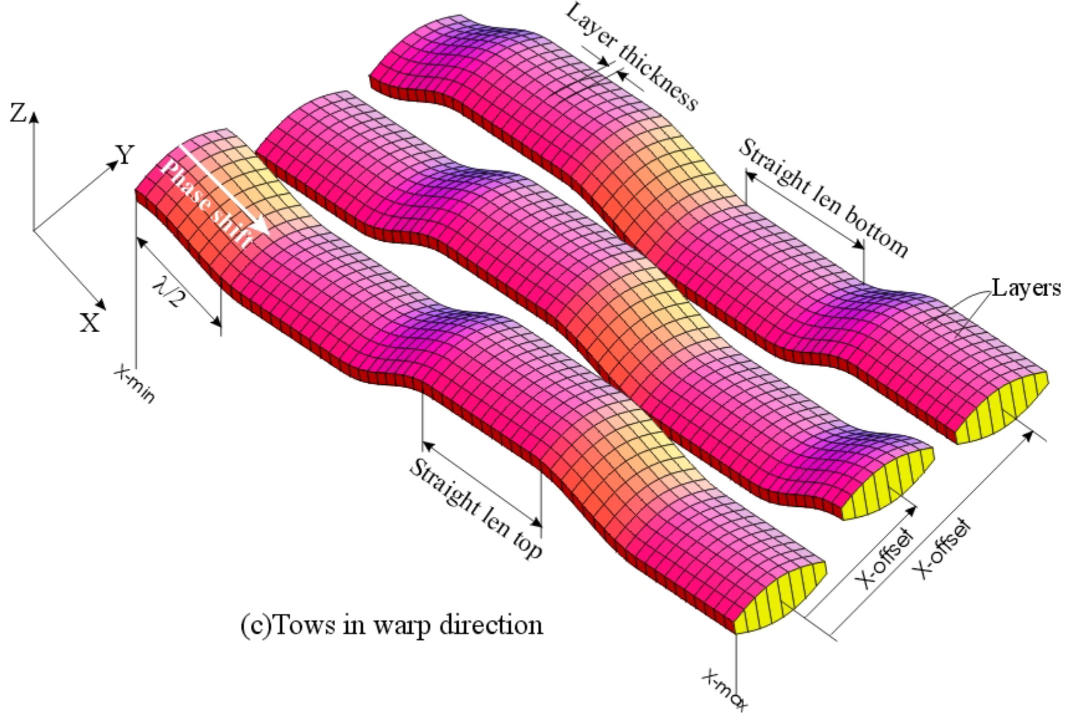

(c)Tows in warp direction

Figure 2.1. Generation of solid models

by the same sine/cosine function) of the tow to produce the complete warp tow. (The complete set of equations to produce tows of the twill weave will be given in section 2.3.1). Applying the same method in the weft direction can produce the weft tow. To produce the complete solid model, the tows can be duplicated and placed side by side. Figure 2.1(c) shows three warp tows of the twill weave that were produced using this strategy. A careful look at this figure shows that the cross-section of the tows is truncated from the sides. It is because the end portion of the lenticular cross-section (Figure 2.1(b)) was removed to show a good view of the undulation in different weaves. In reality, however, the cross-sections are not truncated for the studies herein.

There are certain parameters that govern the architecture of different weaves. For all the weaves the lenticular cross-section shape can be given by

$$Z = \frac{h}{4}\cos\left(\frac{2\pi x}{\lambda}\right) \tag{2.2}$$

where h is twice the height of the cross-section and λ is the wavelength of the wavy region (refer Figure 2.1). The weave pattern will depend on the length of the repeated straight region and on the phase shift. The length of the straight regions and the phase shift can be expressed in terms of the wavelength λ. Phase shift is the phase difference between the adjacent tows of a particular weave. For example, for a typical tow of the twill weave, the phase shift sequence is λ, 3λ/2, 0, λ/2 for the adjacent tows and this pattern keeps on repeating throughout the weave architecture. What this means is that if the phase of the first tow is λ, then that of the second is 3λ/2, of the third is 0 and of the fourth is λ/2 and then this pattern is repeated for 5th, 6th, 7th , 8th tow and so on. The length of the straight regions for this weave is λ/2. If N is the number of tows in one direction (warp or fill) and d is the number of cross-section divisions, then Table 2.1-2.2 gives the complete set of parameters to define the architecture of the different weaves. A layer is a smallest portion of the tow that is swept along the towpath. The layers are shown in the Figure 2.1(c). X-min and x-max refer to the starting and ending x-coordinates of the tow. Flag is a parameter used to specify whether the tow is warp or fill. And x, y, z offsets gives the offset distance between adjoining tows.

Table 2.1. Common parameter list for different weaves

Parameter List (Same for all weave types)		
Number of layers		$(N+1)*d$
Layer Thickness		Equal
x-min, x-max		$0, \frac{(N+1)*\lambda}{2}$
Rotate flag	Warp	0
	Fill	1
x, y, z offset	Warp	$0, \frac{i*\lambda}{2}, 0$ where i = 1..N
	Fill	$\frac{i*\lambda}{2}, 0, 0$ where i = 1..N

Table 2.2. Parameter list that differentiates weaves

		$\frac{\text{Straight length bottom}}{\lambda/2}$	$\frac{\text{Straight length top}}{\lambda/2}$	$\frac{\text{Phase shift}}{\lambda/2}$
Plain Weave	Warp	0	0	$(1, 0)^{\mathbf{r}}$
	Fill	0	0	$(0, 1)^{\mathbf{r}}$
Twill Weave	Warp	1	1	$(2, 3, 0, 1)^{\mathbf{r}}$
	Fill	1	1	$(1, 2, 3, 4)^{\mathbf{r}}$
4 HS	Warp	2	0	$(2, 0, 3, 1)^{\mathbf{r}}$
	Fill	0	2	$(2, 0, 1, 3)^{\mathbf{r}}$
5 HS	Warp	0	3	$(3, 5, 7, 9, 1)^{\mathbf{r}}$
	Fill	3	0	$(3, 1, 9, 7, 5)^{\mathbf{r}}$
8 HS	Warp	0	6	$(6, 3, 0, 5, 2, 7, 4, 1)^{\mathbf{r}}$
	Fill	6	0	$(5, 2, 7, 4, 1, 6, 3, 8)^{\mathbf{r}}$
Basket	Warp	1	1	$(1, 1, 3, 3)^{\mathbf{r}}$
	Fill	1	1	$(2, 0, 0, 2)^{\mathbf{r}}$

Using the Table 2.1-2.2, all the weave architectures can be conveniently generated. Figure 1.1 shows the different weave patterns generated by this method.

2.2.2 Translation vs. extrusion

One thing more worth mentioning at this point is that there are two methods of producing tows: extrusion and translation. When the cross-section is perpendicular to the curve along which it is being swept, the resulting tow is called an extruded tow. When the cross-section is always kept vertical and swept along the curve, the resulting tow is called a translated tow. The woven and braid tows being discussed here were produced by translation as there is less level of complexity in generating those. It was seen in [48] that the tows produced by the extrusion give better results as compared to the tows produced by the translation, as the thickness of the tows remains constant, but for low waviness ratios, for example waviness ratio of 1/10 to 1/20, which is a realistic range for the woven and braided composites, the error because of the translation method is very small and we can utilize translation because of its lesser level of complexity in modeling. Figure 2.2 shows curves produced by the translation and the extrusion. The curves shown are for large waviness ratio to exaggerate the difference.

2.2.3 Idealized geometry of the 2x2 braids:

Braids are formed by mutually intertwining or twisting two or more sets of yarns about each other. One set is called the axial yarn while the other is called the braid yarn. The braid yarns follow angles of +θ and -θ to the longitudinal direction while the axial yarns are placed in the longitudinal direction. If there are only braid yarns, then the resulting structure is called a biaxial braid (Figure 1.2(a)). If the axial yarns are also present with braid yarns, the resulting structure is called a triaxial braid (Figure 1.2(b)).

The angle θ is called the braid angle and it can vary from 15° to 75° [9], depending on the yarn size and size of the axial yarns. The braid structure can also vary depending upon the number of +θ braid yarns passed over and under the -θ braid yarns and vice versa. A 1x1 braid will have one +θ braid yarn passing over and under one -θ

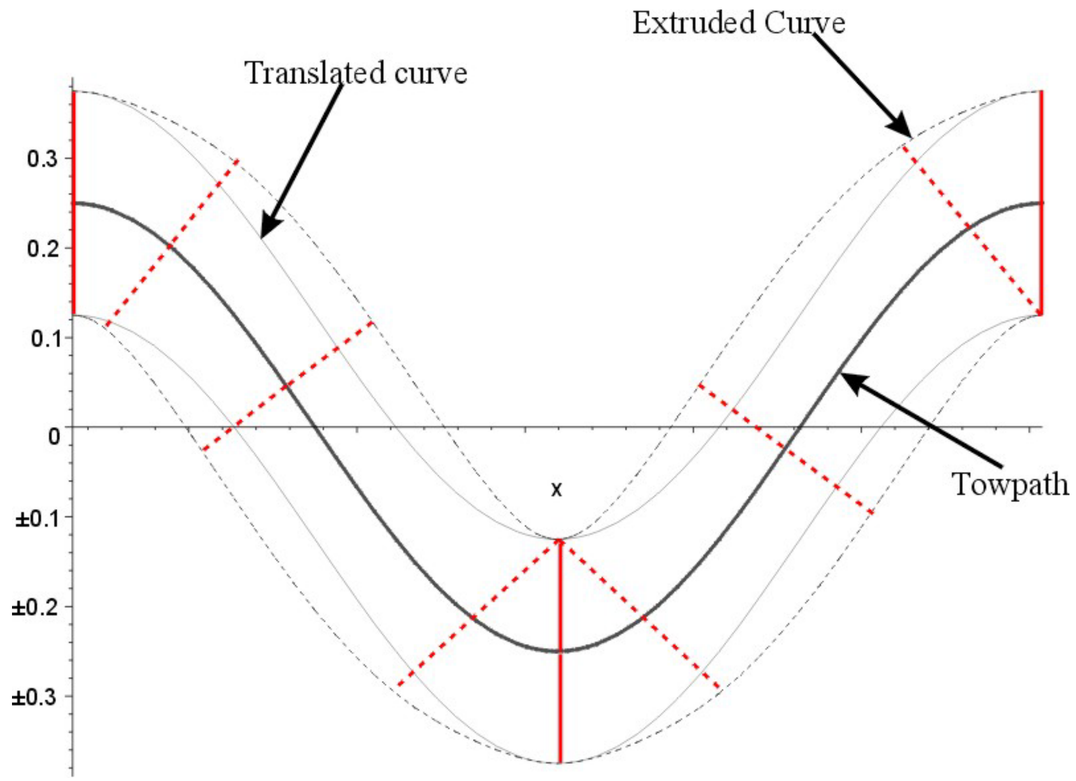

Figure 2.2. Curves produced by extrusion and translation

braid yarn and vice versa. The 2x2 braid structure has an intertwine structure characterized by any given yarn passing over two opposing yarns, then under two opposing yarns, and repeating this pattern. Similarly, there exists 3x3 braid structure characterized by three +θ yarns passing over and under three –θ yarns. Our area of focus in this research is the 2x2 braid. A complete specification of this can be given as "*2-D 2x2 biaxial ±θ braid*". 2-D means that it has two (in-plane) directions as the primary load bearing directions and 2x2 means that +θ yarns pass over and under two –θ yarns. Biaxial means that the yarns run in two directions (no yarns in the axial direction), and θ is the braid angle.

Since the tow cross-section along the tow path is not uniform for the braids, direct model generation is difficult. Careful examination of the tow architecture of the twill weave and the 2x2 biaxial braid (Figure 1.1 and 1.2 (a)) reveals that a ±45° 2x2 biaxial braid is geometrically indistinguishable from the twill rotated by 45°. Both configurations have orthogonal tows. Inspired by this fact, a mapping technique [51] was developed to generate the solid models and the finite element meshes for various 2x2 biaxial braids from the models of the twill weave, which had been developed in previous studies [16].

The mapping technique basically involves shearing the twill weave to produce the 2x2 braids. Giving the shear deformation is a convenient way of producing the braid model, and this strategy can be applied to produce solid models as well as finite element meshes for braids. The mapping technique produces the correct braid model if the shear is applied appropriately. The shear should be applied such that the warp and the weft tows do not change their width and are compatible with each other. That means that they fit together properly. After the shear is applied, the width and the waviness ratio of the warp and weft tows should not differ; otherwise we would get the incorrect model of the braid.

Two methods of mapping to give shear deformation will be discussed next to emphasize this point. To see the difference between two methods, two tows of twill weave will be used. Figure 2.3 shows the top view of a warp and a weft tow and the transformed tows.

First let us apply the shear such that the length of the tow is kept constant when we apply the shear and both x and y-coordinates change for all the points of the twill tows. Let the shear angle be ψ. Then the transformations to apply this shear are:

$$\begin{aligned} x &-> x * cos(\psi) \\ y &-> y + x * \sin(\psi) \end{aligned} \tag{2.3}$$

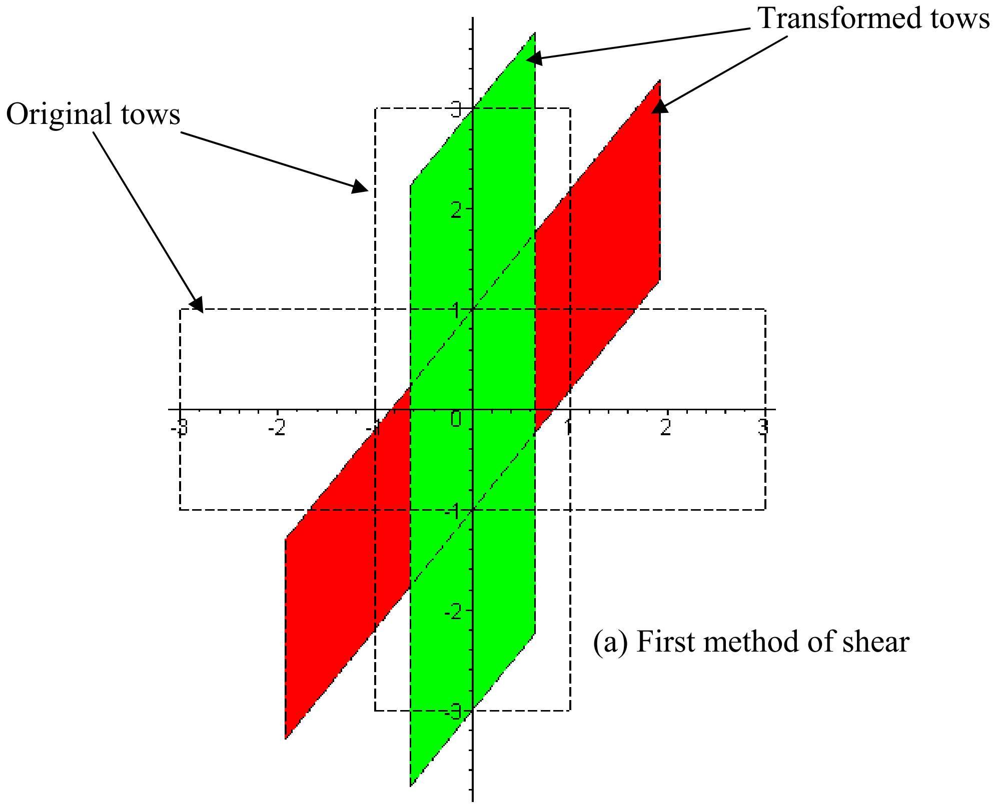

(a) First method of shear

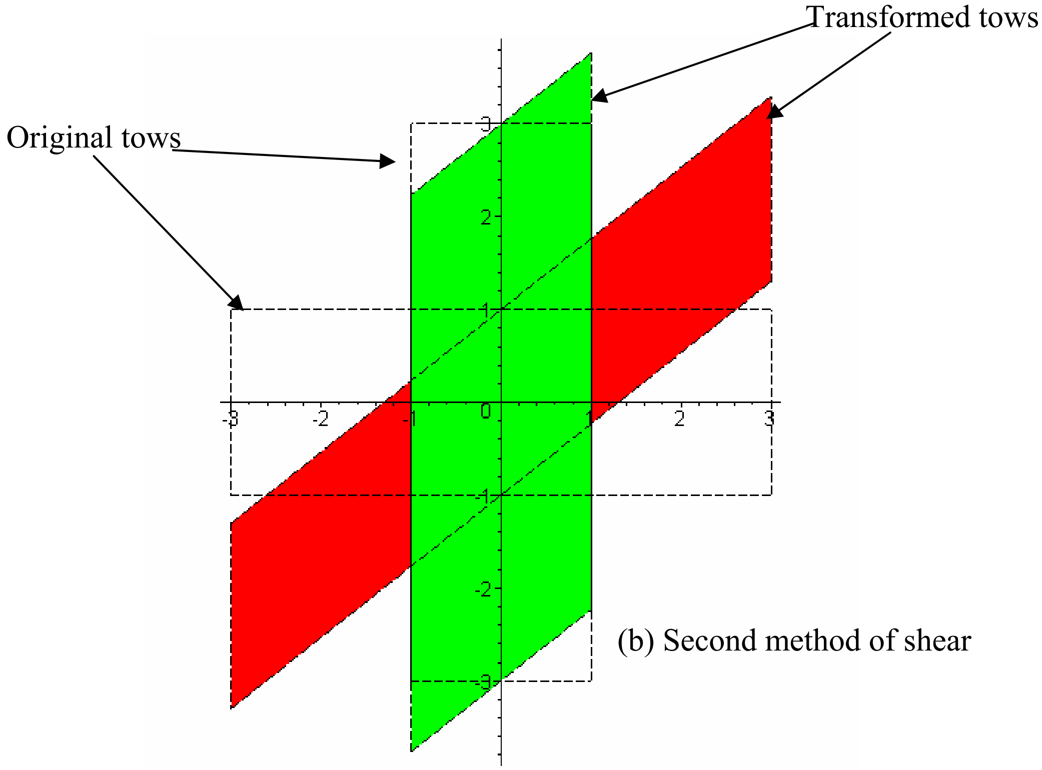

(b) Second method of shear

Figure 2.3. Two mapping techniques

Using this, the transformed tows shown in Figure 2.3(a) are obtained. Since the plot is to the scale, it is obvious that the width of both the tows is same. This kind of transformation produces braid tows with waviness ratio and width unaltered. So the tows produced are balanced and compatible to each other.

Now let us examine the case when shear is such that the length of the tow increases when we apply the shear. The x-coordinate of all the points of the transformed tow is same as the x-coordinate of the corresponding points of the original tow. Note that this method of shear is frequently used when we have infinitesimal small deformations and strain displacement relations are linear. The transformations to apply this shear are:

$$\begin{aligned} &x -> x \\ &y -> y + x * sin(\psi) \end{aligned} \tag{2.4}$$

After using these transformations, the tows obtained are shown in Figure 2.3(b). The figure clearly shows that the transformed tows have different width from each other. Their waviness ratio will also differ and they will not fit properly with each other making this an inaccurate method to produce braid tows. So the first method of shear has been chosen.

After transforming the tows using this shear method, they are rotated to bring the axis of the braids aligned to the global coordinate system. This is explained in Figure 2.4. First we shear the twill tows, which are shown dotted figure to get braid tows shown dark. The twill tows are sheared through an angle ψ called shear angle herein. The shear angle ψ and the braid angle θ are related with each other by the following relationship:

$$\Psi = 2\theta - 90° \tag{2.5}$$

Hence Equation 2.3 can be written as:

$$\begin{Bmatrix} x \\ y \end{Bmatrix} \rightarrow \begin{bmatrix} sin(2\theta) & 0 \\ -cos(2\theta) & 1 \end{bmatrix} \begin{Bmatrix} x \\ y \end{Bmatrix} \tag{2.6}$$

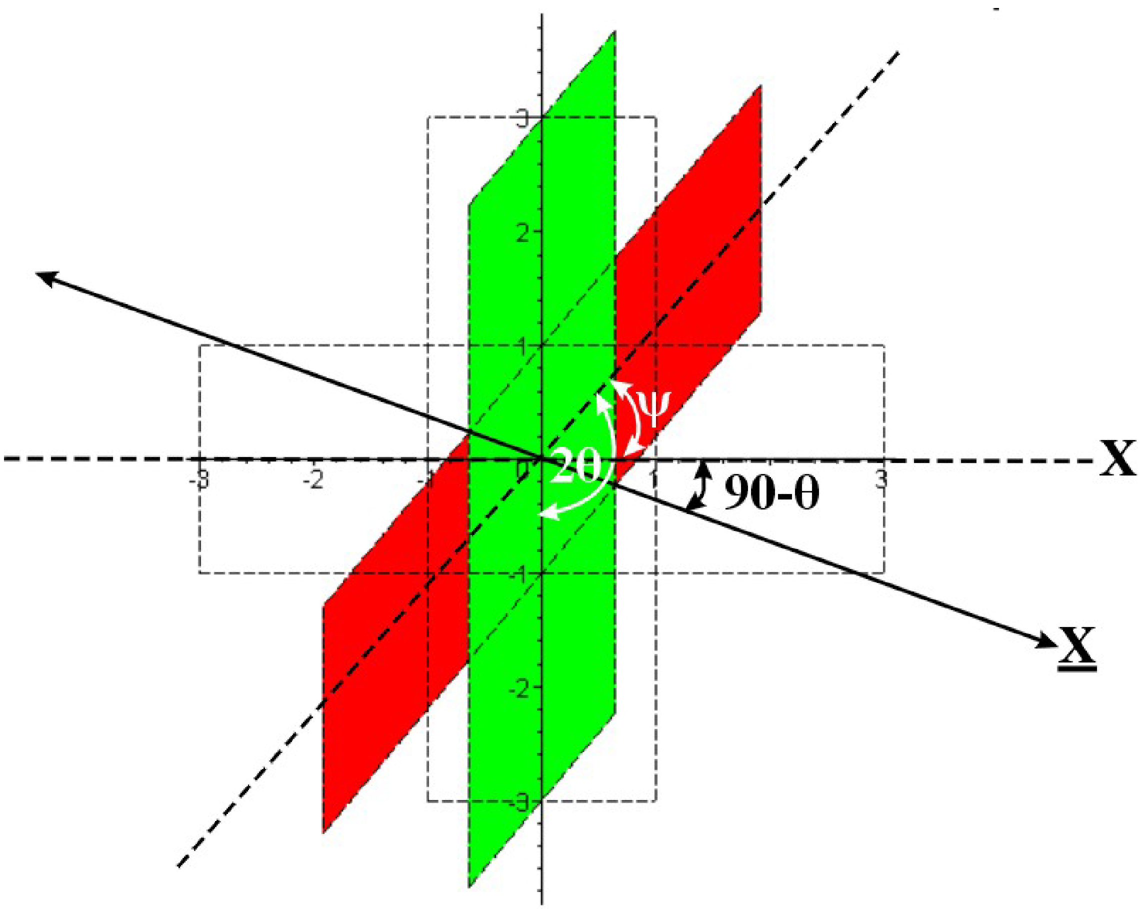

Figure 2.4.   Transformations for mapping from twill to 2x2 braid

The braid tows run at an angle of +θ and –θ with respect to its axis. As shown in the Figure 2.4, X are the braid axis. Now we want the braid axis to coincide with the global coordinate axes X. So the braid axes given by X need to be rotated through and angle of (90°-θ), so that X coincides with X. The necessary transformation matrix for this is given by:

$$T = \begin{bmatrix} sin\,\theta & -cos\,\theta \\ cos\,\theta & sin\,\theta \end{bmatrix} \tag{2.7}$$

Combining the above two transformation, the complete set of transformations can be written in terms of the braid angle as:

$$\begin{Bmatrix} x' \\ y' \end{Bmatrix} = \begin{bmatrix} sin\,\theta & -cos\,\theta \\ cos\,\theta & sin\,\theta \end{bmatrix} \begin{bmatrix} sin\,2\theta & 0 \\ -cos\,2\theta & 1 \end{bmatrix} \begin{Bmatrix} x \\ y \end{Bmatrix} \tag{2.8}$$

where (x,y) and (x',y') are the coordinates in the twill and the braid models, respectively; θ is the braid angle. By using this mapping, different solid models of braid were produced and are shown in Figure 2.5.

2.3 Description of a typical tow

The whole of the twill or the braid architecture can be produced by spatially translating and rotating the copies of a single tow. In this section, the idealized architecture of a typical twill and a braid tow is described in detail.

2.3.1 Description of the idealized geometry of the twill tow

Figure 2.6 shows a typical tow of the twill weave. The tow cross-section is lenticular and was produced by using simple cosine function as described in the previous section. The tow was produced by extruding the cross-section along its length, the tow length also being defined by cosine functions given as:

$$z(x,y) = \pm A * cos(\Omega y) \pm A * cos(\Omega x) \tag{2.9}$$

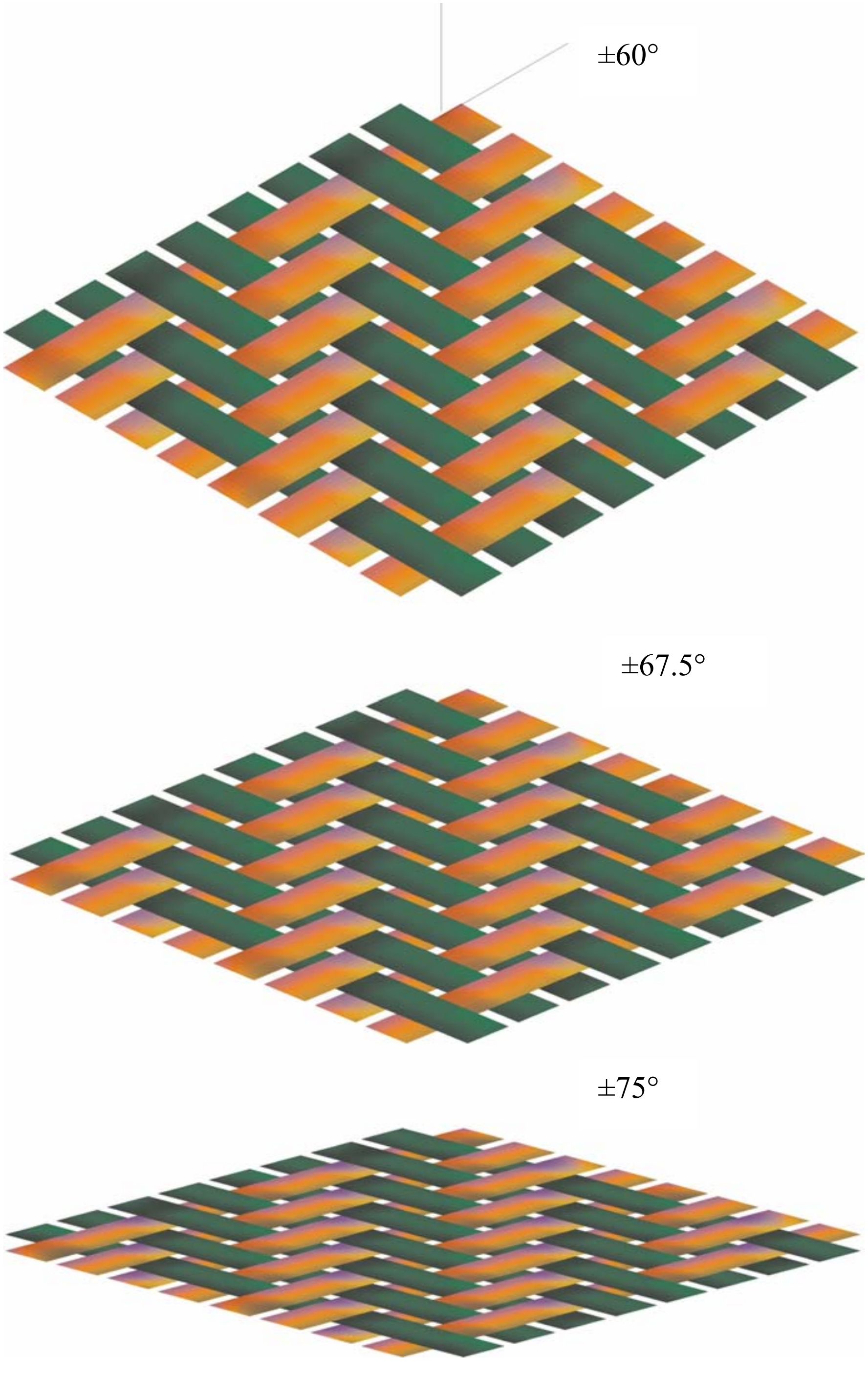

Figure 2.5. Some solid models of 2x2 braids

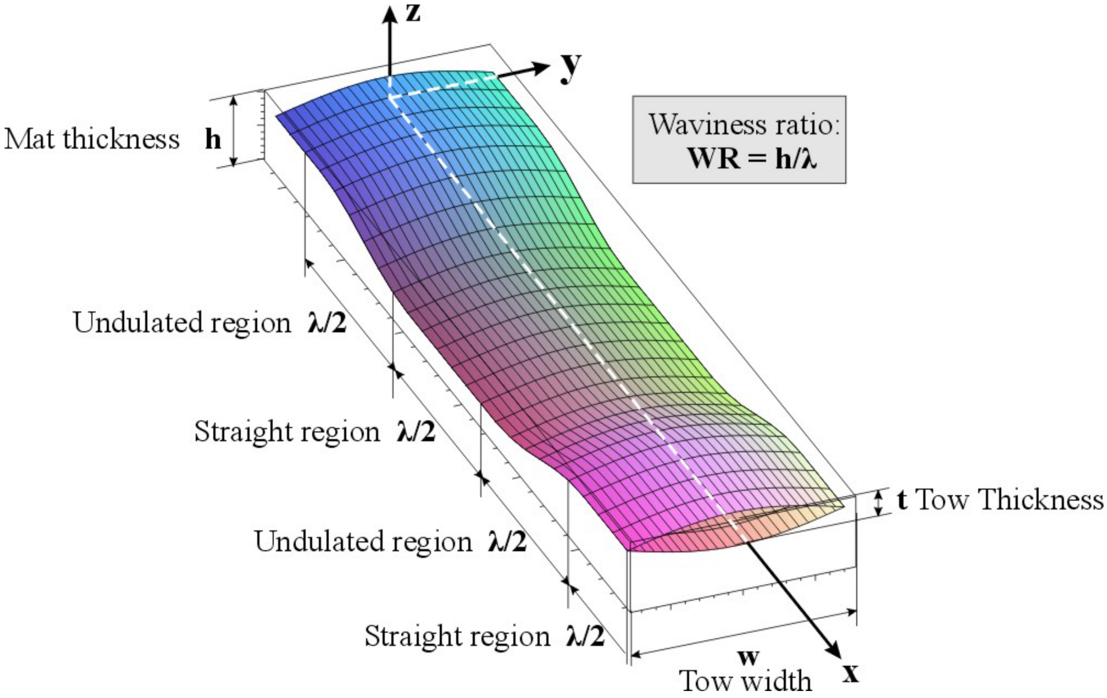

Figure 2.6. Tow architecture of the twill

where λ = wavelength of wavy region and $A = h/4$, where h is the height of the tow path, which is equal to mat thickness.

The tow has both the straight and undulated regions. The length of the straight and the undulated regions depends on the type of the weave we are looking at. The tow shown in Figure 2.6 belongs to the twill weave and hence in this case the straight and the undulated regions have equal length. Further, the straight and wavy regions can be separated by planes parallel to the YZ planes. The tow cross-section is constant and does not vary as we move along the length of the tow. The path of the fibers can be visualized by the lines on the surface of the towpath in Figure 2.6. The phase difference between various fibers running along a single tow is zero, which means that all the fibers start to undulate and straighten at the same x coordinate and the function defining their path is same for all the fibers. The complete set of equations defining the towpath is given next.

Let λ = wavelength of wavy region.

h = the height of the tow path = mat thickness

$\text{wavinessratio} = \rho = h/\lambda$, $A = h/4$

Let $\Omega = 2\pi/\lambda$, $F(y) = A * cos(\Omega y)$

$$For: \lambda/4 \le x \le 2\lambda/4$$
$$z_{top}(x,y) = F(y) + F(0\lambda/4)$$
$$z_{bottom}(x,y) = -F(y) + F(0\lambda/4)$$

$$For: 2\lambda/4 \le x \le 4\lambda/4$$
$$z_{top}(x,y) = F(y) - F(x)$$
$$z_{bottom}(x,y) = -F(y) - F(x)$$

$$For: 4\lambda/4 \le x \le 6\lambda/4$$
$$z_{top}(x,y) = F(y) + F(2\lambda/4)$$
$$z_{bottom}(x,y) = -F(y) + F(2\lambda/4) \qquad (2.10)$$

$$For: 6\lambda/4 \le x \le 8\lambda/4$$
$$z_{top}(x,y) = F(y) + F(x)$$
$$z_{bottom}(x,y) = -F(y) + F(x)$$

$$For: 8\lambda/4 \le x \le 9\lambda/4$$
$$z_{top}(x,y) = F(y) + F(4\lambda/4)$$
$$z_{bottom}(x,y) = -F(y) + F(4\lambda/4)$$

The function defining the tow path is the same for all fibers at any distance y from the origin. Further, we see that the cross-section shape of the tow does not change as we move along the towpath. It is lenticular for all the cross-sections. The purpose of including the discussion of the tow architecture of the twill weave here is twofold. Firstly, it will be easier to understand the more complex tow architecture of 2x2 braid by comparing it with the twill weave. Secondly it will show that the tow architectures of the twill and of the 2x2 braid are different except for the case when braid angle is ±45°.

2.3.2 Description of the idealized geometry of the braid tow

Figure 2.7 shows the 2x2 braid tow that was produced from the twill tow by the mapping technique discussed earlier. This tow has straight as well as undulated regions. Unlike the twill, where we could separate the straight and undulated regions by planes parallel to YZ planes, here the straight and undulated regions can not be separated by planes parallel to YZ plane except for the ±45° braid. This is due to the fact that the braid tow is sheared and the fibers in a single tow do not have the same phase angle. Now there exists a phase difference between different fibers. The phase of a fiber at y = -1 is not the same as that of a fiber that is running at any other value of y. This phase shift is $= \phi = y * \tan(\theta)$, where θ is the braid angle. This means that the different fibers of the tow do not undulate and straighten at the same x coordinate. One fiber may have started undulating and another may not have yet started to undulate. The phase shift is a measure of this. If the braid fibers present at y = -1 start undulating downwards at x = 0 then the braid fibers present at any distance y start undulating downwards at a distance $x = y * \tan(\theta)$. By joining these tow paths as we go along the y-axis the top and bottom surfaces of the braid tow can be found.

The complete set of equations defining the towpath at any distance y is:

Let ϕ = phaseshift = $y * tan(\theta)$ and $F(y) = A * cos(\Omega y)$

$$
\begin{aligned}
&For: \lambda/4 \le x \le 2\lambda/4 \\
&\qquad z_{top}(x,y) = F(y) + F(0\lambda/4 - \phi) \\
&\qquad z_{bottom}(x,y) = -F(y) + F(0\lambda/4 - \phi) \\
&For: 2\lambda/4 \le x \le 4\lambda/4 \\
&\qquad z_{top}(x,y) = F(y) - F(x - \phi) \\
&\qquad z_{bottom}(x,y) = -F(y) - F(x - \phi) \\
&For: 4\lambda/4 \le x \le 6\lambda/4 \\
&\qquad z_{top}(x,y) = F(y) + F(2\lambda/4 - \phi) \\
&\qquad z_{bottom}(x,y) = -F(y) + F(2\lambda/4 - \phi)
\end{aligned}
\tag{2.11}
$$

$For: 6\lambda/4 \le x \le 8\lambda/4$

$$z_{top}(x,y) = F(y) + F(x-\phi)$$

$$z_{bottom}(x,y) = -F(y) + F(x-\phi)$$

$For: 8\lambda/4 \le x \le 9\lambda/4$

$$z_{top}(x,y) = F(y) + F(4\lambda/4-\phi)$$

$$z_{bottom}(x,y) = -F(y) + F(4\lambda/4-\phi)$$

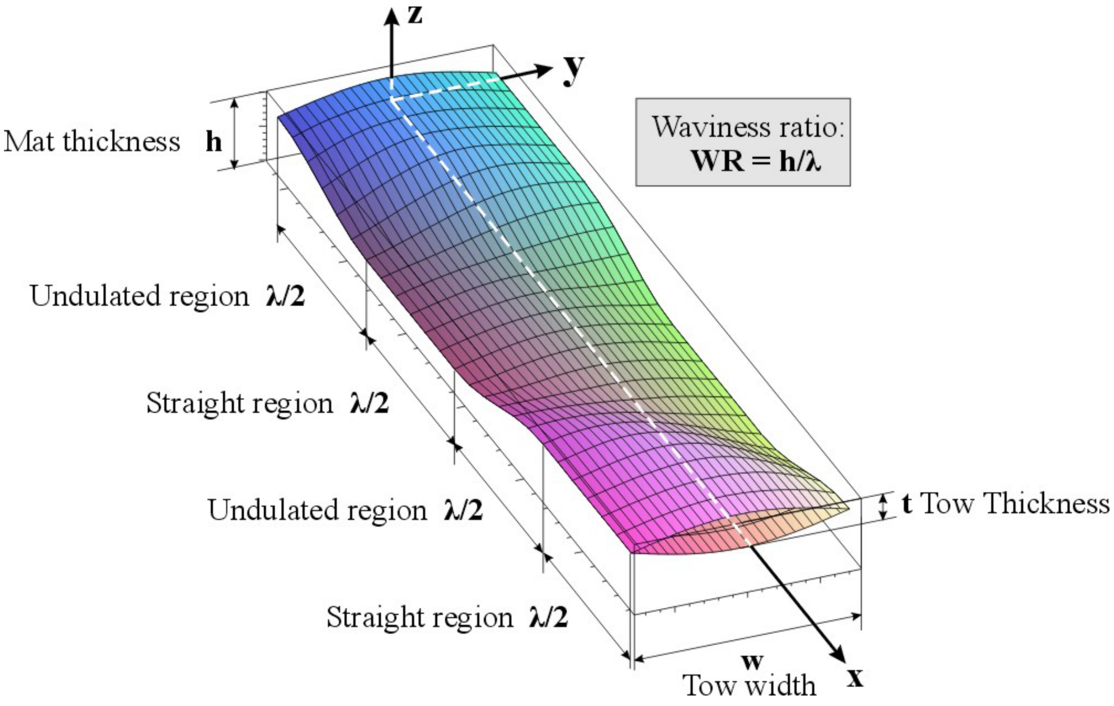

Figure 2.7. Tow architecture of a 2x2 Braid

2.3.3 Varying cross-sections of the braid tow

Note that the phase of the undulation varies across the tow width. This is because the interlaced tows are not orthogonal to each other. This causes the tow cross- sections to vary in an unusual fashion. This is illustrated in Figure 2.8(a), which shows the cross-sections at different points along the tow path. Clearly the cross-section shape is varying as we are moving along the tow path. It is no more lenticular everywhere unlike for the twill. Figure 2.8(b) shows the cross-section shapes at three sections along the length. The line of sight is parallel to a line joining the center points of two cross-sections of straight regions of the braid tow. The line of sight is marked as *central axis* in the Figure 2.9.

Figure 2.8(b) shows the difference in braid cross-sections at x = 1λ/4, 2λ/4, 3λ/4. It is worth noting here that the cross-section shape change so much that it just flattens at the bottom for some regions. For example at x = 2λ/4, the cross-section shape is perfectly flat at the bottom, towards negative y direction.

It should be noted that although the cross-sections are of different shapes, the cross-sectional area is constant. Hence, there is not a concern about "disappearing" material or variable fiber volume fraction in the tow. The cross-sectional areas for a particular wavelength and height of the tow have been calculated below to check this:

For x = 1λ/4

$$\text{The area of the cross-section} = A = \int_{-\frac{\lambda}{4}}^{\frac{\lambda}{4}} \left[Z_{top}\left(\frac{\lambda}{4}, y\right) - Z_{bot}\left(\frac{\lambda}{4}, y\right) \right] dy$$

$$= \frac{3\,(2+\pi)}{2\,\pi} - \frac{3\,(-2+\pi)}{2\,\pi} = \frac{6}{\pi}$$

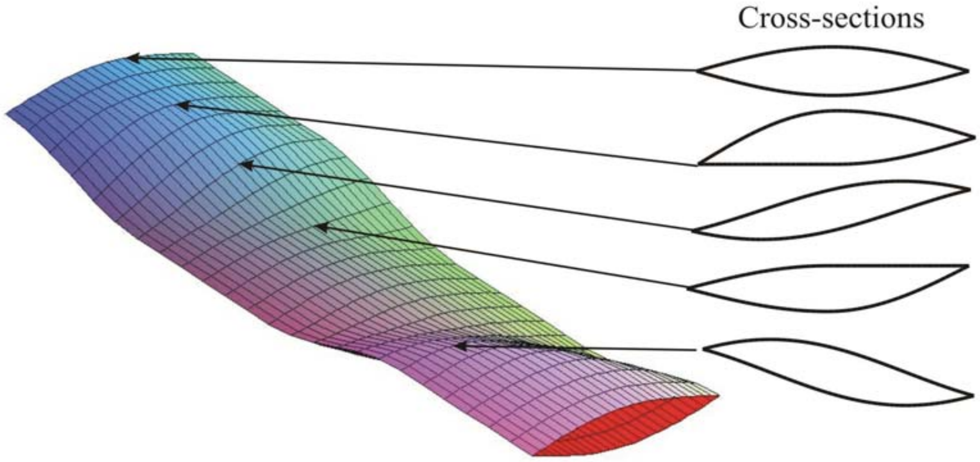

(a) Cross-section geometry in various regions

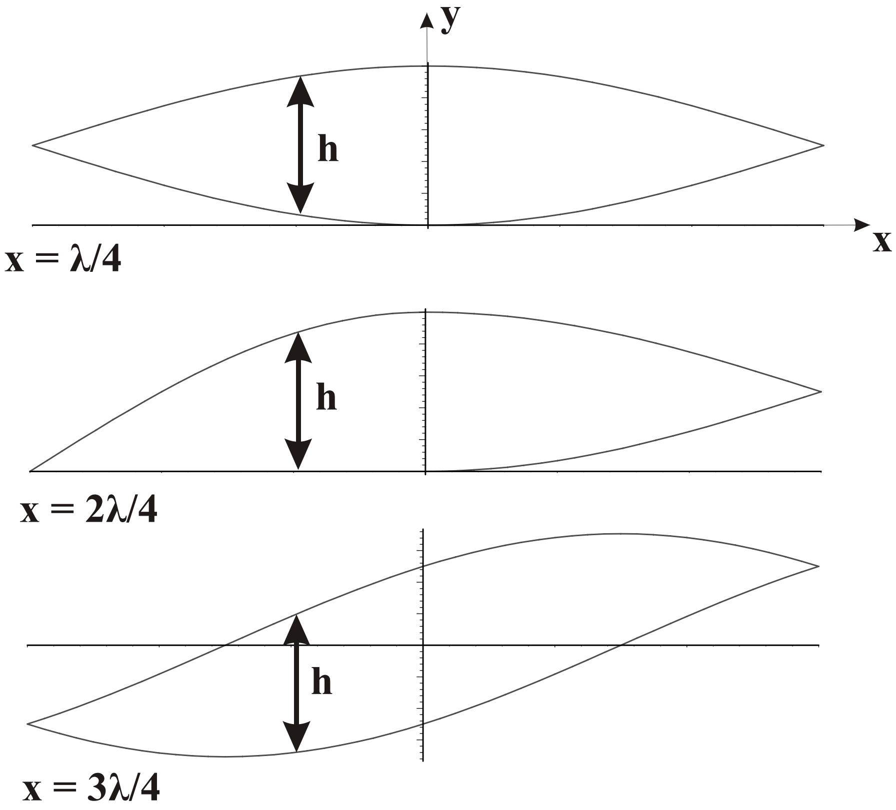

(b) Cross-section area remains the same

Figure 2.8. Variation in cross-sections of braid tow

For x = 2λ/4

$$\text{The area of the cross-section} = A = \int_{-\frac{\lambda}{4}}^{\frac{\lambda}{4}} \left[Z_{top}\left(\frac{2\lambda}{4}, y\right) - Z_{bot}\left(\frac{2\lambda}{4}, y\right) \right] dy$$

$$= \frac{3\,(6+\pi)}{4\,\pi} - \frac{3\,(-2+\pi)}{4\,\pi} = \frac{6}{\pi}$$

For x = 3λ/4

$$\text{The area of the cross-section} = A = \int_{-\frac{\lambda}{4}}^{\frac{\lambda}{4}} \left[Z_{top}\left(\frac{3\lambda}{4}, y\right) - Z_{bot}\left(\frac{3\lambda}{4}, y\right) \right] dy$$

$$= \frac{3}{\pi} + \frac{3}{\pi} = \frac{6}{\pi}$$

Hence we see mathematically that the area does remain the same for all the cross-sections. This is due to the fact that the height of the cross-section at a particular value of y is not changing. The constant height is at a particular value of y is shown in Figure 2.8(b). The height is just moving up and down to produce a different cross-section shape at different values of x.

2.3.4 Material angle transformations

We have the material properties in the material coordinate system, but to perform analysis, we must know the material properties in the global coordinate system. As seen in Figure 2.9, as we move along the braid tow, we observe that the tow is straight for some length and undulated for some, and the straight and undulated lengths run periodically. If we join the centers of two adjacent cross-sections of the tow where the tow is straight, we obtain an axis called central axis herein. The material angle Ψ at any point along the tow is the angle between any yarn element and the central axis at that location. In the straight region, the material angle Ψ is zero, but in the undulated region, the material angle Ψ is non-zero as the yarn elements are inclined to central axis. This material angle Ψ is changing at every point in the undulated region. The material angle Ψ at any point can be calculated as:

$$\psi = tan^{-1}\left[\frac{d}{dx}z(x,y)\right] \tag{2.12}$$

where the function z(x, y) describes the tow path and has already been discussed in the previous section. Further, the braid tows run at an angle of +θ and -θ. Hence we need to transform all the material properties through an angle of θ and Ψ to bring these to the global coordinate system. The required transformations are derived as follows:

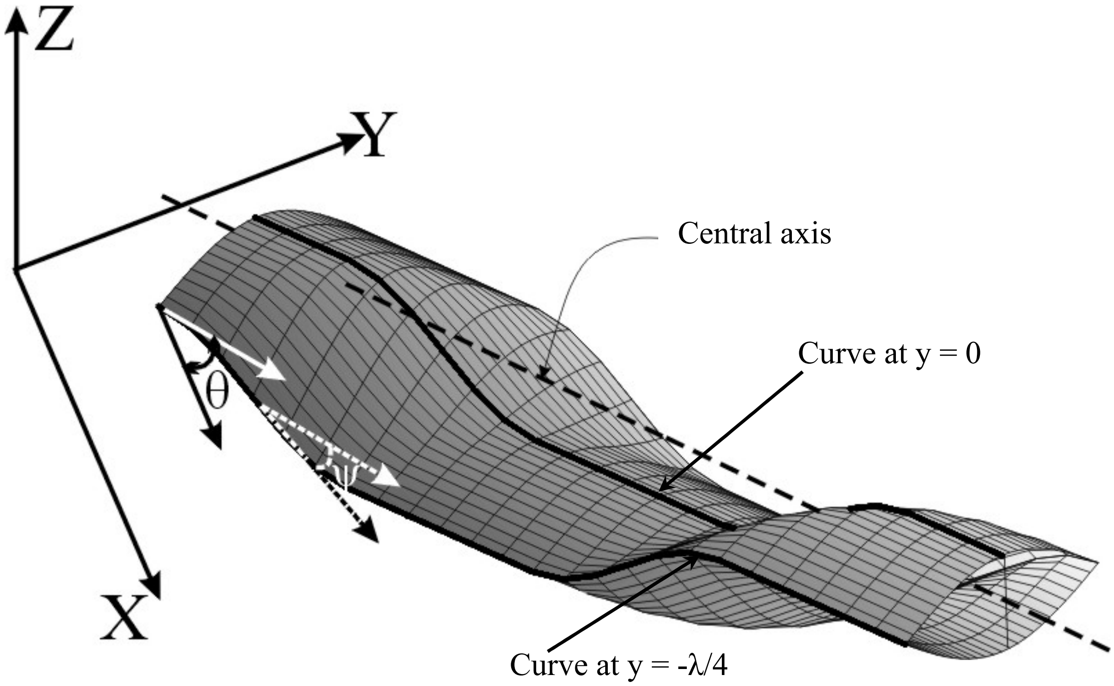

Figure 2.9. Material angle transformations

Let the body be rotated about the Z axis such that the coordinate system changes from XYZ to X'Y'Z' as shown in Figure 2.10. If we rotate the body with coordinate axes attached to the body, the coordinates of any arbitrary point P on the body do not change. Then

$$X = X' = X_p \tag{2.13}$$

But after rotation we want the coordinates of the same point P in the old coordinate system. They are found as follows:

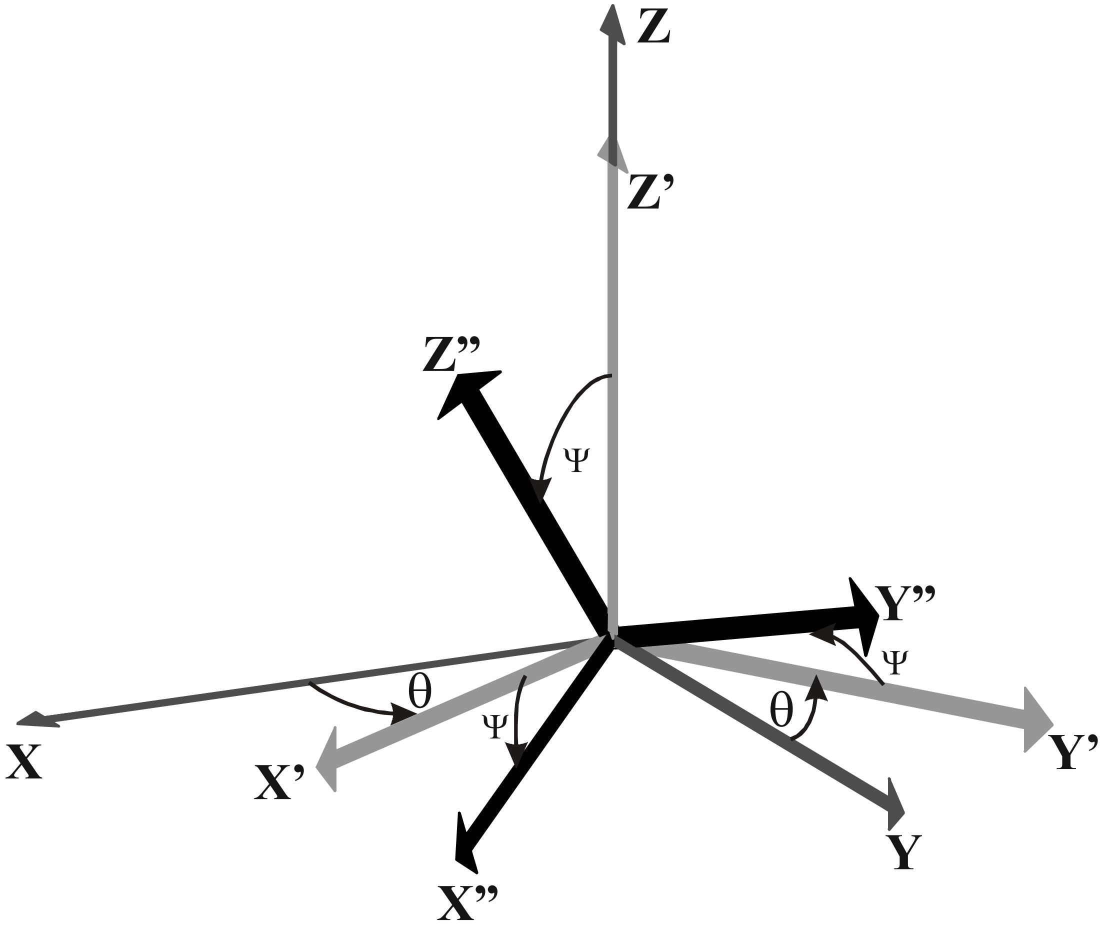

Figure 2.10. Coordinate transformations

The transformation rule while transforming from coordinate system XYZ to X'Y'Z' is given by:

$$X' = a * X$$

Substituting for X' from equation (2.13), we obtain

$$X_p = a * X$$

$$X = a^{-1} * X_p \tag{2.14}$$

Here X denotes the new coordinates of the same point P in the original coordinate system after transformation a and Xp denotes the coordinates of the same point P in the original coordinate system before transformation a.

Now further if we rotate the body about the origin with original coordinate system XYZ attached to body so that coordinate system changes to X", then the coordinates of the point P do not change in X and X" system i.e.

$$X = X''$$

Substituting for X from equation (2.14) in above equation, we get

$$X'' = a^{-1} * X_p \tag{2.15}$$

But after this rotation also, we want the coordinates of point P in the original coordinate system XYZ. They are found as follows:

The transformation law for transforming from coordinate system XYZ to X"Y"Z" is given by:

$$X'' = b * X$$

Substituting for X" from equation (2.15), we get

$$a^{-1} * X_p = b * X$$

Taking b to the left side of the equation, we get

$$b^{-1} * a^{-1} * X_p = X$$

Putting $a^{-1} = a^T$ and $b^{-1} = b^T$ in the above equation, we get

$$b^T * a^T * X_p = X$$

Taking b^T and a^T on the right side of the equation, we get

$$X_p = \left[b^T a^T \right]^{-1} X$$

$$\Rightarrow \qquad X_p = a * b * X \qquad \text{as} \quad \left[b^T a^T \right]^{-1} = a * b$$

Here X are the new coordinates of the point P in the original coordinate system after transformations a and b. And Xp are the coordinates of the point P in the original coordinate system before transformations a and b. Hence the transformation is:

$$X_p = a * b * X \tag{2.16}$$

Therefore, the transformation matrix for a vector is **ab**. This can then be used with the tensor transformation formula to transform the material properties.

Now we must determine the material angle variation along the tow path (Figure 2.9). Lets first see a particular curve of the tow path along the x-axis. The material angle (Ψ) here is changing at every point as we are going along the x-axis and moreover the material angle Ψ is also changing as we are moving in the y-direction.

Lets analyze three curves at distances of y = -λ/4, y = 0 and y = λ/4 . Two of these curves are shown in Figure 2.9. The material angle Ψ for curves at these values of y is given by the following relations:

$$\psi = tan^{-1}\left[\frac{d}{dx} z(x, \lambda/4)\right], tan^{-1}\left[\frac{d}{dx} z(x, 0)\right], tan^{-1}\left[\frac{d}{dx} z(x, \lambda/4)\right] \tag{2.17}$$

These material angles are drawn in Figure 2.11. We see that ψ is maximum at a point, which is in the middle of the undulating region. The maximum angle ψ is called the "*crimp angle*" and its value is approximately 24° for waviness ratio = 1/3 and is approximately 10° for waviness ratio = 1/9. In summary, following observations can be made about the material angle variation:

- ψ does not vary in the z-direction.
- ψ varies along the tow path.
- Variation of ψ along the tow path varies across the tow because there exists phase shift within the tow.

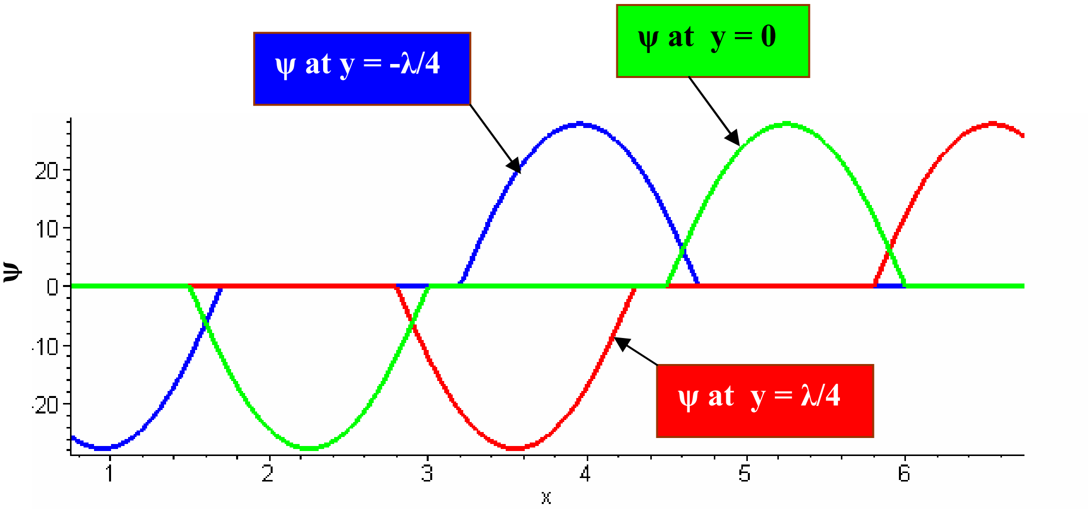

Figure 2.11. Material angle variation at y =-λ/4, 0 and λ/4

2.4 Finite element models

Figure 2.12 shows a micrograph [8] of a dry braid mat. As is obvious from the figure, there is a repeated pattern of interlacing. In micromechanics this is referred to as "*periodicity*". If the periodicity is exploited, finite element models can be developed for a single representative volume element (RVE) that will behave as though it is surrounded by many other RVEs. The unit cell of a periodic microstructure is the smallest region that can produce the whole structure by spatially translating itself without the use of rotation or reflection. One does not need to model the entire microstructure. A single unit cell can be modeled to reduce the analysis region. But in textile composites, modeling even a single unit cell can be very expensive because of the complex geometry involved. Fortunately, textile composites often exhibit symmetry inside a single unit cell. The analysis region can be further reduced from a single unit cell to a smaller subcell (for example half or one fourth of a unit cell etc.) by exploiting symmetry operations like mirroring, rotation or a combination of the two. Hence, the unit cell should be chosen such that it can offer some symmetry to reduce the analysis

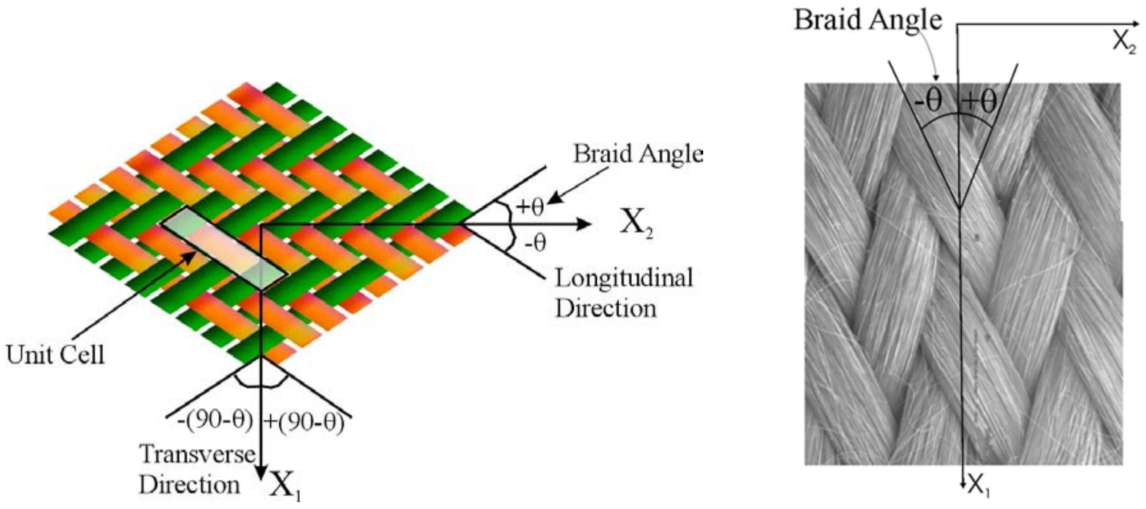

Figure 2.12. Schematics of braids

region. Here the symmetries were exploited and the analysis region was reduced to one fourth of the unit cell for the symmetric stacking and to one half for the simple stacking (see Figure 2.13) of the braided mats.

2.4.1 Some typical finite element models

The finite element models (Figure 2.14) were developed for the unit cell shown in Figure 2.12. As discussed earlier the cross-sections of the braid tow are not uniform, so direct finite element mesh generation was difficult. By the mapping technique described earlier to produce solid models, finite element models were also generated from models of the twill weave, which were produced in earlier studies by a building block technique in [3].

Depending upon the requirement, any number of mats can be stacked on the top of each other. Figure 2.13 shows the simple and symmetric stacking of mats. The analysis region can be reduced to one half for the simple stacking and to one fourth for the symmetric stacking. The results produced by full unit cell and a part of the unit cell were compared with each other to validate the methodology and it was seen that the results matched for the two cases.

For each braid angle or waviness ratio, a different finite element model must be generated. Figure 2.14 shows two unit cells for ±70° braid. One has very large waviness ratio (1/3) and the other has small waviness ratio (1/9).

Depending on the tow volume fraction in a model, the tow cross-section will either be lenticular or flattened. If the tow volume fraction is $\leq 2/\pi$, the cross-section will be lenticular and if the tow volume fraction is $> 2/\pi$, the cross-section will be flattened. For example, for the material systems used in the parametric studies (will follow in the next section), one material system had flattened cross-section and other had lenticular. The finite element models with flattened tow cross-section are shown in Figure 2.14 and ones with lenticular cross-section are shown in Figure 2.15.

A typical mesh used for obtaining effective properties contained 720 hexahedral 20-node brick elements and 3130 nodes. A 20-node brick element is shown in Figure 2.16. One coarse finite element model with 48 elements and 238 nodes is shown in Figure 2.15.

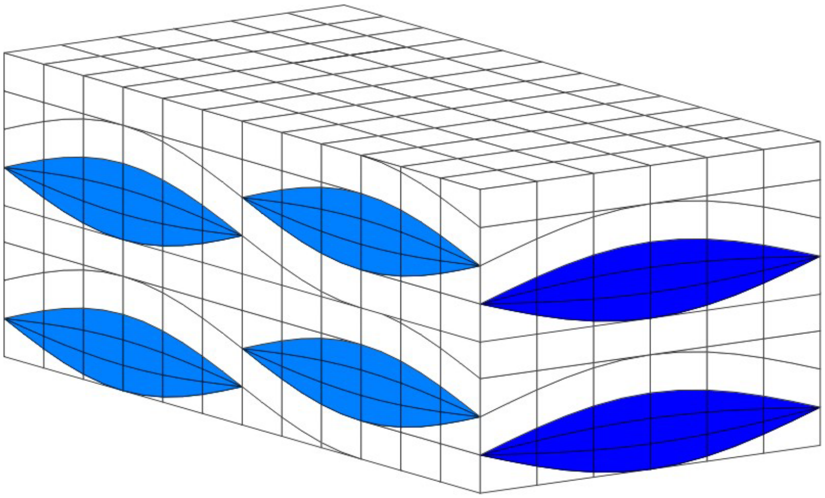

Simple stacking

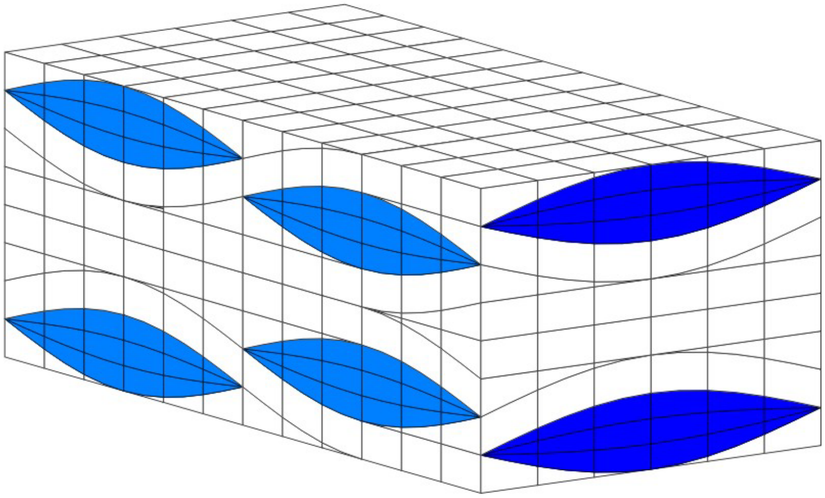

Symmetric stacking

Figure 2.13. Simple and symmetric stacking of mats

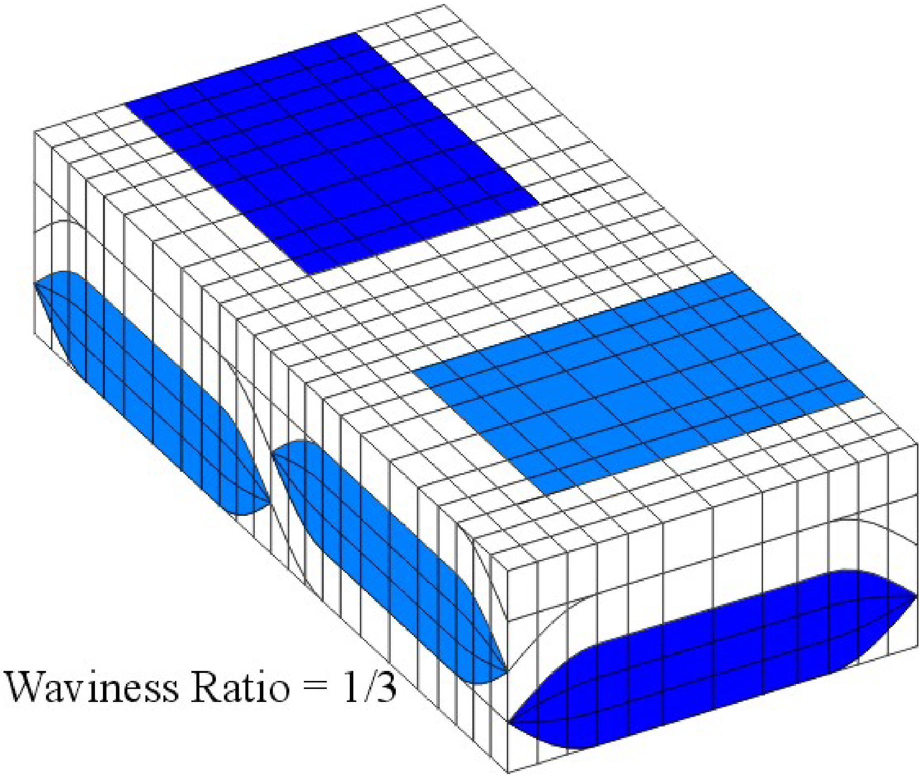

(a) Waviness Ratio = 1/3

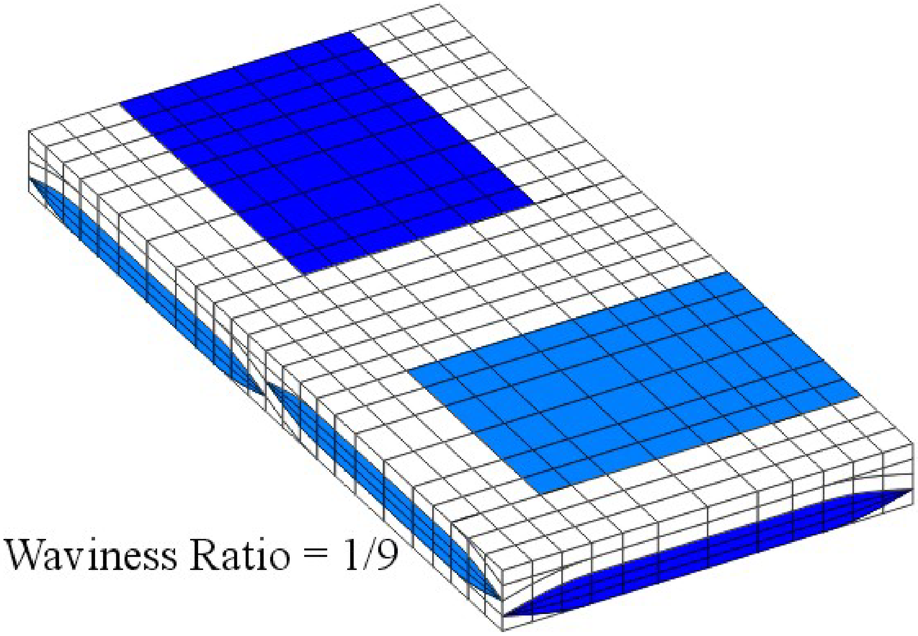

(b) Waviness Ratio = 1/9

Figure 2.14. Typical finite element models for flattened cross-sections

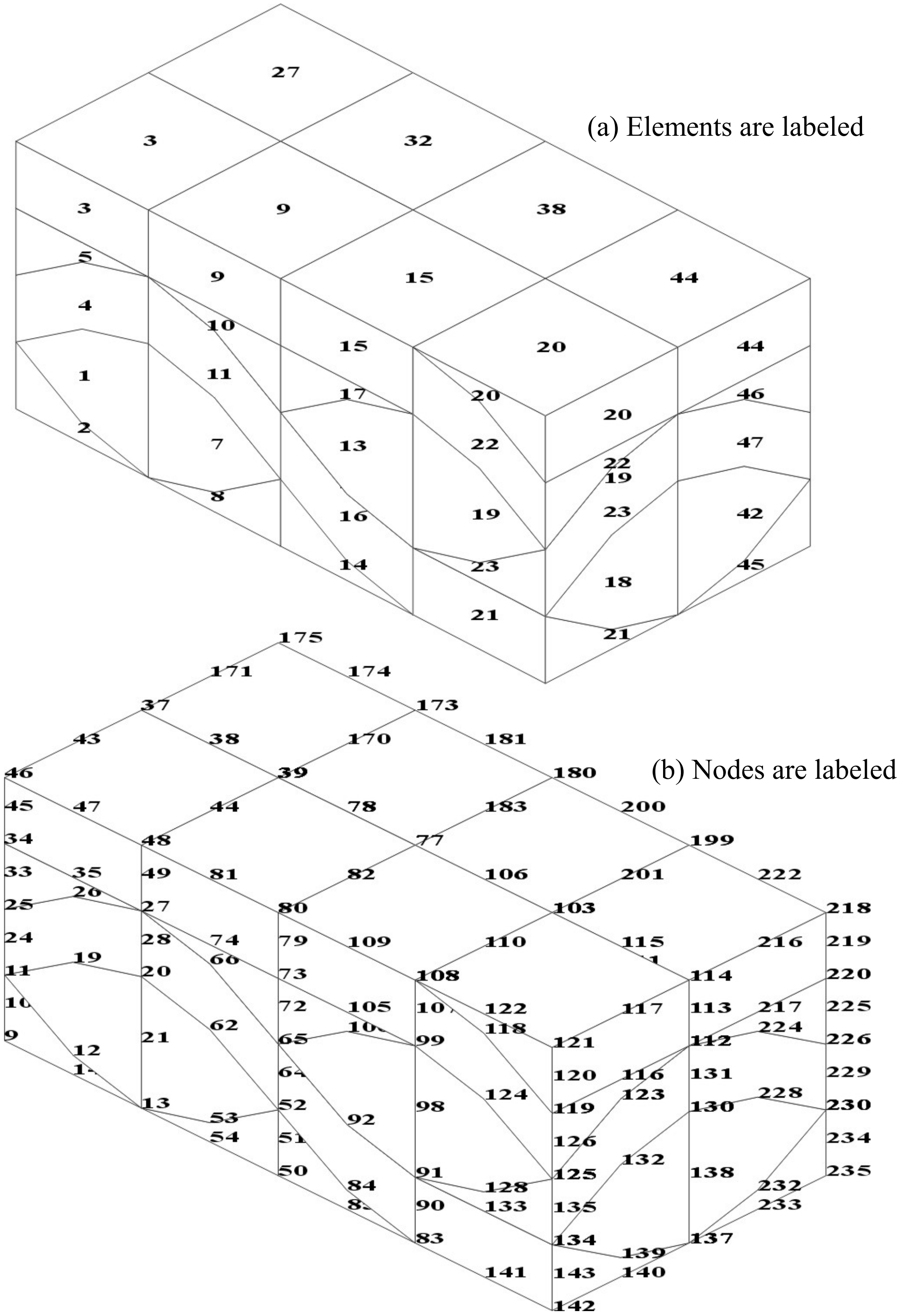

(a) Elements are labeled

(b) Nodes are labeled

Figure 2.15. Finite element model for lenticular cross-section with nodes and elements labeled

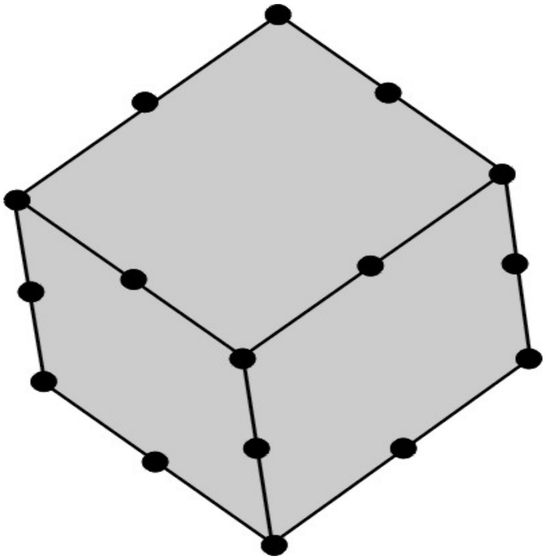

Figure 2.16. A 20-node brick element

2.4.2 Governing differential equations

The governing differential equations are reviewed in this section [54]. The equations of motion and deformation of a solid body can be classified into following four categories:

(1) Kinematics (strain-displacement relations)

(2) Kinetics (conservation of linear and angular momentum)

(3) Constitutive equations (stress-strain relations)

An overview of the above equations is presented below.

Kinematics involves the study of the geometric changes or deformations in the body without considering the forces acting on it. Let ε, the strain tensor in Voight's notation, be given by

$$\varepsilon = \left\{ \varepsilon_{xx}, \varepsilon_{yy}, \varepsilon_{zz}, \varepsilon_{xy}, \varepsilon_{yz}, \varepsilon_{zx} \right\}$$

Let **u** denotes the displacement vector and the coordinates **X** = (X_1, X_2, X_3) denote the material coordinates of the body. The coordinate system **X** is fixed on the given body in the undeformed configuration and its position **x** at any time is referred to the material coordinate **X** as:

$$\boldsymbol{x} = \boldsymbol{x}(X_1, X_2, X_3)$$

If **E** denotes the finite (Green-Lagrange) strain tensor, the strain-displacement relations are given as:

$$E_{ij} = \frac{1}{2}\left(\frac{\partial u_i}{\partial X_j} + \frac{\partial u_j}{\partial X_i} + \frac{\partial u_k}{\partial X_i}\frac{\partial u_k}{\partial X_j} \right)$$

If we assume the strains and rotations are infinitesimal, the above strain-displacement relations can be reduced to

$$\varepsilon_{ij} = \frac{1}{2}\left(\frac{\partial u_i}{\partial x_j} + \frac{\partial u_j}{\partial x_i} \right) \tag{2.18}$$

For infinitesimal deformations, components of the infinitesimal strain satisfy $\left|\varepsilon_{ij}\right| \ll 1$. The use of the infinitesimal strain tensor to characterize the infinitesimal deformation of the body is in fact linearization, which means that if $\varepsilon^{(1)}$ is the strain corresponding to displacement $u^{(1)}$ and $\varepsilon^{(2)}$ is the strain corresponding to displacement $u^{(2)}$, then $\varepsilon^{(1)}+\varepsilon^{(2)}$ is the strain corresponding to displacement $u^{(1)}+u^{(2)}$.

Compatibility equations

If a displacement field is given, the Cartesian components of the strain tensor are uniquely obtained by the strain-displacement relations of equation 2.18. But if a strain field is given for which a corresponding displacement field **u** is not given, one seeks to find the solution for the displacement field. In order to do that, one has to solve the strain-displacement relations for **u**. That involves six independent equations and only three unknown components of **u**. Hence a single valued solution for **u** might not exist. But if an allowable displacement field does exist, then the corresponding strain field is said to be compatible. The following are the compatibility equations to ensure that a single-valued displacement field exists:

$$\frac{\partial^2 \varepsilon_{kn}}{\partial x_l \partial x_m} + \frac{\partial^2 \varepsilon_{lm}}{\partial x_k \partial x_n} - \frac{\partial^2 \varepsilon_{km}}{\partial x_l \partial x_n} - \frac{\partial^2 \varepsilon_{ln}}{\partial x_k \partial x_m} = 0 \qquad (2.19)$$

This is a set of 81 equations out of which only 6 are linearly independent.

Kinetics

Forces acting on a body can be classified into internal and external forces. Kinetics is the study of static or dynamic equilibrium of forces acting on a body. If we consider a given mass with density ρ, on which some forces are acting, then from the balance of linear momentum, the equations of equilibrium can be written as:

$$\begin{aligned} \frac{\partial \sigma_{xx}}{\partial x} + \frac{\partial \sigma_{xy}}{\partial y} + \frac{\partial \sigma_{xz}}{\partial z} + \rho b_x = \rho a_x \\ \frac{\partial \sigma_{yx}}{\partial x} + \frac{\partial \sigma_{yy}}{\partial y} + \frac{\partial \sigma_{yz}}{\partial z} + \rho b_y = \rho a_y \\ \frac{\partial \sigma_{zx}}{\partial x} + \frac{\partial \sigma_{zy}}{\partial y} + \frac{\partial \sigma_{zz}}{\partial z} + \rho b_z = \rho a_z \end{aligned} \qquad (2.20)$$

where $\sigma = \left\{ \sigma_{xx}, \sigma_{yy}, \sigma_{zz}, \sigma_{xy}, \sigma_{yz}, \sigma_{zx} \right\}$ denotes the Voight's stress tensor, **b** is the body force and **a** is the acceleration of the body. If there are no body forces and no acceleration, then the terms containing body force **b** and acceleration **a** vanish. In the absence of any body moments, the conservation of angular momentum leads to symmetry of the stress-tensor.

Constitutive equations

The kinematics, mechanical principles are applicable to any material body irrespective of its constitution. The constitutive equations characterize the individual material response of a body. They relate the dependent variable introduced in the kinetic equations to those in the kinematic relations. Constitutive equations give a relationship between stresses and strains. In general, the stress-strain relation for infinitesimal deformation of an elastic material is non-linear, as stress does not have to be linearly proportional to strain. But if components of stress are assumed to be in linear proportion to components of stress, then the constitutive equations can be written in the following general form:

$$\sigma_i = C_{ij}\varepsilon_j$$

where C_{ij} is the stiffness matrix, which is symmetric and has at most 21 independent stiffness coefficients. The inverse of stiffness tensor is the compliance tensor (S_{ij}) and is given as:

$$\varepsilon_i = S_{ij}\sigma_j$$

$$\text{where } S_{ij} = \begin{bmatrix} \frac{1}{E_{11}} & \frac{-\upsilon_{12}}{E_{11}} & \frac{-\upsilon_{13}}{E_{11}} & \frac{\eta_{14}}{E_{11}} & \frac{\eta_{15}}{E_{11}} & \frac{\eta_{16}}{E_{11}} \\ \frac{-\upsilon_{21}}{E_{22}} & \frac{1}{E_{22}} & \frac{-\upsilon_{23}}{E_{22}} & \frac{\eta_{24}}{E_{22}} & \frac{\eta_{25}}{E_{22}} & \frac{\eta_{26}}{E_{22}} \\ \frac{-\upsilon_{31}}{E_{33}} & \frac{-\upsilon_{32}}{E_{33}} & \frac{1}{E_{33}} & \frac{\eta_{34}}{E_{33}} & \frac{\eta_{35}}{E_{33}} & \frac{\eta_{36}}{E_{33}} \\ \frac{\eta_{41}}{G_{12}} & \frac{\eta_{42}}{G_{12}} & \frac{\eta_{43}}{G_{12}} & \frac{1}{G_{12}} & \frac{\eta_{45}}{G_{12}} & \frac{\eta_{46}}{G_{12}} \\ \frac{\eta_{51}}{G_{23}} & \frac{\eta_{52}}{G_{23}} & \frac{\eta_{53}}{G_{23}} & \frac{\eta_{54}}{G_{23}} & \frac{1}{G_{23}} & \frac{\eta_{56}}{G_{23}} \\ \frac{\eta_{61}}{G_{31}} & \frac{\eta_{62}}{G_{31}} & \frac{\eta_{63}}{G_{31}} & \frac{\eta_{64}}{G_{31}} & \frac{\eta_{65}}{G_{31}} & \frac{1}{G_{31}} \end{bmatrix} \tag{2.21}$$

Here E_{11}, E_{22}, E_{33} denote the Young's moduli in the 1, 2 and 3 material directions respectively, G_{12} is the in-plane shear modulus and G_{23} and G_{13} are out of plane shear moduli. The Poisson's ratio ν_{ij} is defined as the negative of the ratio of transverse strain in the j^{th} direction to the axial strain in the i^{th} direction when stressed in the i^{th} direction. The shear coupling coefficient η_{ij} is the ratio of strain in the j^{th} direction to the strain in the i^{th} direction when stresses in the i^{th} direction. The compliance matrix shown in equation 2.21 is fully populated. When the analysis is done, it will be seen though that some of the engineering constants are zero for 2x2 braids and the material is orthotropic with only 9 independent constants.

2.4.3 Boundary conditions

The purpose of micromechanics analysis is to obtain macroscopically homogenized properties, so that structures can be conveniently analyzed. Homogenized properties of the structure that have periodicity can be obtained by analyzing an RVE of their periodic structure. The response of the RVE is volume averaged to get the effective properties. A volume averaged variable is defined as:

$$\langle \bullet \rangle = \frac{1}{V}\int_V \bullet dV \tag{2.22}$$

where $\bullet$ is the variable of interest. For example, effective moduli in longitudinal direction (E_{11}) can be found as:

$$E_{11} = \frac{\langle \sigma_{11} \rangle}{\langle \varepsilon_{11} \rangle}, \text{ where } \langle \sigma_{11} \rangle = \frac{1}{V}\int_V \sigma_{11} dV \text{ and } \langle \varepsilon_{11} \rangle = \frac{1}{V}\int_V \varepsilon_{11} dV$$

To get the volume averaged stresses and strains, we need to know microscopic stress and strain fields. To obtain these, we must solve the boundary value problem for the RVE. Generally speaking, for periodic microstructures, one of the following three boundary conditions can be applied to set the problem up [27].

Uniform tractions: $T = \langle \sigma \rangle n$ on S

Uniform strain: $U = \langle \varepsilon \rangle X$ on S

Periodicity: $U = \langle \varepsilon \rangle X + U^*(X)$ and $U^*(X) = U^*(X+D)$ in V

where V is the volume of body, S its boundary and D is the period of periodic displacement function U*, which is the local perturbation to the macroscopic displacement field.

The boundary conditions can be obtained for a full unit cell by exploiting periodicity. Symmetry within the unit cell can be exploited to find the boundary conditions for part of the unit cell. For this particular braid, exploiting the symmetries allows FEA analysis using only one fourth of the RVE for a symmetrically stacked laminate. For some textiles, there are greater symmetries and the savings are even greater. For example for a plain weave, the analysis region was reduced to as low as 1/32 of the unit cell [27].

If two regions are brought equivalent to each other in terms of geometry, material distribution, load conditions and mechanical response, then they are called equivalent subcells. Symmetry operations like mirroring or rotating brings the coordinate system of one subcell the same as the coordinate system of the other. For example in the Figure 2.17, subcell A is equivalent to subcell B, because it is same as B after π rotation about x_3 axis. The basic formulas to find the boundary conditions are derived in [27]. These formulas have the capability to exploit periodicity as well as symmetry operations like mirroring, rotation or a combination of two within a unit cell, so that the size of analysis region can be reduced to a part of unit cell. The formulas are reproduced here:

$$d = X^{ox} - c \cdot X^{oy}$$

$$X^A = c \cdot X^B + d$$

$$U(X^A) = \gamma c \cdot U(X^B) + \left\langle \frac{\partial U}{\partial X} \right\rangle \cdot d + R \tag{2.23}$$

$$\varepsilon(X^A) = \gamma c \cdot \varepsilon(X^B) \cdot c^T$$

$$\sigma(X^A) = \gamma c \cdot \sigma(X^B) \cdot c^T$$

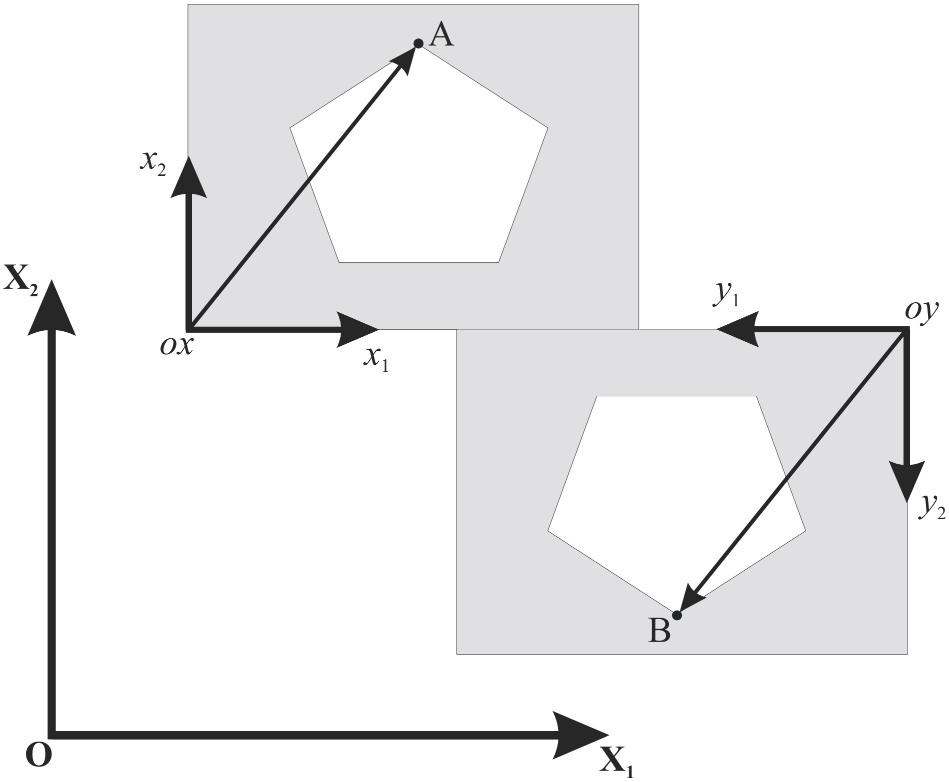

Figure 2.17. Equivalent subcells

where X^{ox} and X^{oy} are the coordinates of the origin of the subcells A and B respectively with respect to global coordinate system X. X^A and X^B are the global coordinates of two equivalent points A and B in the equivalent subcells; γ (+1 or -1) is the load reversal factor, which depends on various load conditions and symmetry operations. $c = a^T b$, where a and b are the orthogonal transformation tensors between the global coordinate system and local coordinate systems. R is a constant and its non-zero components are determined by the equation $-\gamma c \cdot R = R$. Interested readers are highly recommended to go through ref [27] for the understanding the derivation of Equations 2.23.

Figure 2.18 shows the microstructure of the 2x2 braid in which the subcells are marked M, A, B, C, D, E and F. A complete unit cell can be obtained by combining M and B subcells or C and D subcells. Then the translation of one unit cell produces the entire microstructure of the braid. Since one unit cell has symmetries within it, the analysis region can further be reduced. Subcell M is one-fourth of the full unit cell for the symmetric stacking and one-half of the unit cell for the simple stacking of mats. To find the boundary conditions for the subcell M, we will use formulas given by Equation 2.23. The adjoining subcells A, B, C, D, E and F will be used in deriving the boundary conditions for all the faces of subcell M. One has to use formulas given by Equation 2.23 for each loading case and for all the adjoining subcells one by one. For the 2x2 braid, the derivation for boundary conditions for some loading cases is exactly the same with each other thereby reducing the labor considerably.

In Figure 2.18, the subcells are also shown apart also with their respective local coordinate systems. The local coordinate system is found such that if one moves through a certain distance in any of the local coordinate system of the subcells, the same equivalent point is reached in each subcell. For example, if we move through a distance of {a/2, 0, 0} in the local coordinate systems of each subcell, we reach the same point at the boundary of all the subcells. In this way the subcells are geometrically equivalent with each other. The subcells also need to be equivalent to each other with respect to loading conditions and should also exhibit material symmetry. The symmetry operations that make the coordinate system of subcell M the same as the coordinate system of adjoining subcells are listed in Table 2.3.

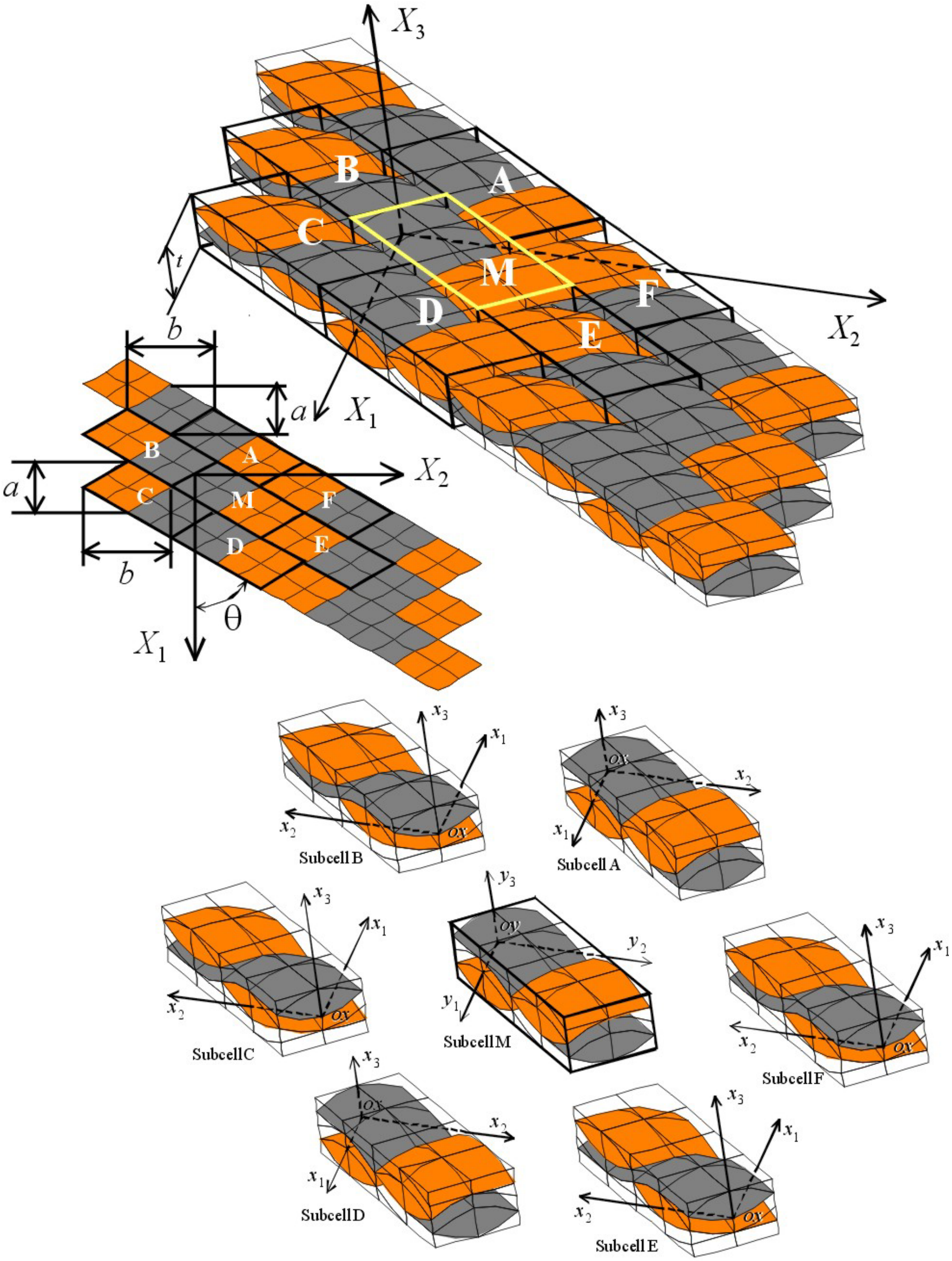

Figure 2.18. Derivation of boundary conditions for 2x2 braids

Table 2.3. Symmetry operations to bring the subcells equivalent to each other

Pair	Symmetry Operation
Subcells M and A	None
Subcells M and B	π rotation about X_3 axis
Subcells M and C	π rotation about X_3 axis
Subcells M and D	None
Subcells M and E	π rotation about X_3 axis
Subcells M and F	π rotation about X_3 axis

The boundary conditions for M will be found in terms of the multi-point constraints that exist between the faces of the subcell M. The multi-point constraints will now be found by utilizing the symmetry operations enlisted in Table 2.3. First of all, the parameters for different loading cases and different combinations of subcells with subcell M are found and then they are substituted in Equation 2.23 to find the complete set of multi-point constraints. Here we will demonstrate the use of formulas only for the $\langle\sigma_{11}\rangle$ loading condition. The $\langle\sigma_{11}\rangle$ loading condition means that only $\langle\sigma_{11}\rangle$ stress component is zero and all other volume averaged stresses: $\langle\sigma_{22}\rangle$, $\langle\sigma_{33}\rangle$, $\langle\sigma_{12}\rangle$, $\langle\sigma_{23}\rangle$ and $\langle\sigma_{31}\rangle$ are zero. The procedure for finding the boundary conditions for other loading conditions is exactly the same. First we find the relations utilizing equivalency between subcells M and F. The subcell *M* plays the role of type "B" subcell in Equation 2.23 and F play the role of type "A" subcell. This will give the boundary conditions for the shaded faces in Figure 2.19. The steps to derive boundary conditions, for non zero $\langle\sigma_{11}\rangle$ loading case, are mentioned below:

(1) First of all the coordinates of the origin of local coordinate systems of M and F are found as: (*x* is associated with subcell F and *y* is associated with subcell M).

$X^{ox} = \{a, 2b, 0\}$

$X^{oy} = \{0, 0, 0\}$

(2) The orthogonal transformations between global coordinate system and local coordinate systems of M and F are:

a = Transformation between local coordinate system of F and Global coordinate system = $\begin{bmatrix} -1 & 0 & 0 \\ 0 & -1 & 0 \\ 0 & 0 & 1 \end{bmatrix}$

It can be seen here that the local coordinate system of subcell M is the same as the global coordinate system although that is not a requirement for use in formulas given by Equation 2.23. So b is an identity matrix.

b = Transformation between local coordinate system of F and Global coordinate system

$$= \begin{bmatrix} 1 & 0 & 0 \\ 0 & 1 & 0 \\ 0 & 0 & 1 \end{bmatrix}$$

$$\mathbf{c} = \mathbf{a}^T \cdot \mathbf{b} = \begin{bmatrix} -1 & 0 & 0 \\ 0 & -1 & 0 \\ 0 & 0 & 1 \end{bmatrix}$$

(3) $\mathbf{d} = \mathbf{X}^{ox} - \mathbf{c} \cdot \mathbf{X}^{oy} = \{a \quad 2b \quad 0\}$

(4) $\mathbf{X}^{ox} - \mathbf{X}^{oy} + c.(\mathbf{X}^{ox} - \mathbf{X}^{oy}) = \begin{bmatrix} a \\ 2b \\ 0 \end{bmatrix} + \begin{bmatrix} -1 & 0 & 0 \\ 0 & -1 & 0 \\ 0 & 0 & 1 \end{bmatrix} \begin{bmatrix} a \\ 2b \\ 0 \end{bmatrix} = \begin{bmatrix} 0 \\ 0 \\ 0 \end{bmatrix}$

Hence no translation is required.

(5) $\mathbf{X}^B$ = The coordinates of any point on the shaded face in Figure 2.19 in global coordinate system

$$= \left\{ -\frac{a}{2} + \frac{aX_2}{b}, X_2, X_3 \right\}$$

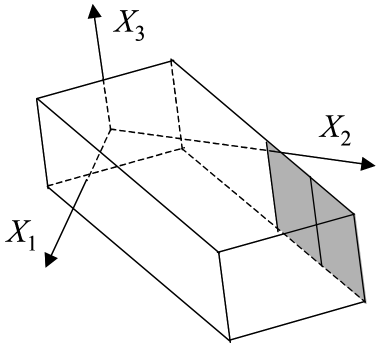

Figure 2.19. Faces under considerations for deriving MPC's

then $\mathbf{X}^A = \mathbf{c} \cdot \mathbf{X}^B + \mathbf{d} = \left\{ \frac{3a}{2} - \frac{aX_2}{b}, -X_2 + 2b, X_3 \right\}$

(6) For the loading case (non zero $\langle \sigma_{11} \rangle$) and the symmetry operation (π rotation about X3) at hand the value of γ is =1 as indicated in the table below.

Table 2.4. Value of load reversal factor γ

	<σ11>	<σ22>	<σ33>	<σ12>	<σ23>	<σ13>
Mirroring about X1	1	1	1	-1	1	-1
Mirroring about X2	1	1	1	-1	-1	1
Mirroring about X3	1	1	1	1	-1	-1
π rotation about X1	1	1	1	-1	1	-1
π rotation about X2	1	1	1	-1	-1	1
π rotation about X3	**1**	1	1	1	-1	-1

(7) The non-zero components of vector R can be found by using the equation –γcR = R and can be solved as part of the finite element solution. But for all the loading cases for the braid, the constant vectors **R** are found to be identically zero for all the pairs of equivalent subcells.

(8) The displacement gradient tensor $\left\langle \frac{\partial U_i}{\partial X_j} \right\rangle$ is symmetric. Using the equation $\left\langle \frac{\partial U}{\partial X} \right\rangle = \gamma c \cdot \left\langle \frac{\partial U}{\partial X} \right\rangle . c^T$, the non-zero components of the displacement gradient tensor $\left\langle \frac{\partial U}{\partial X} \right\rangle$ are found for all the combinations of subcell M with adjoining subcells (A, B, C, D, E, F). Then the intersection of non-zero components of all above combinations gives the overall non-zero components of the matrix $\left\langle \frac{\partial U}{\partial X} \right\rangle$. For the case at hand, we have: $\left\langle \frac{\partial U}{\partial X} \right\rangle = \begin{bmatrix} \left\langle \frac{\partial U_1}{\partial X_1} \right\rangle & \left\langle \frac{\partial U_1}{\partial X_2} \right\rangle & 0 \\ \left\langle \frac{\partial U_1}{\partial X_2} \right\rangle & \left\langle \frac{\partial U_2}{\partial X_2} \right\rangle & 0 \\ 0 & 0 & \left\langle \frac{\partial U_3}{\partial X_3} \right\rangle \end{bmatrix}$, so we have four independent non-zero components of displacement gradient.

(9) Finally these parameters are introduced in the equation

$$U(X^A) = \gamma c \cdot U(X^B) + \left\langle \frac{\partial U}{\partial X} \right\rangle \cdot d + R\,,$$

to get the following multipoint constraints for the shaded faces of the Figure 2.19 shown above.

$$U_1\left(\frac{3}{2}a - \frac{a X_2}{b}, -X_2 + 2b, X_3\right) = -U_1\left(-\frac{1}{2}a + \frac{a X_2}{b}, X_2, X_3\right) + \left\langle \frac{\partial}{\partial X_1} U_1 \right\rangle a + 2 \left\langle \frac{\partial}{\partial X_2} U_1 \right\rangle b$$

$$U_2\left(\frac{3}{2}a - \frac{a X_2}{b}, -X_2 + 2b, X_3\right) = -U_2\left(-\frac{1}{2}a + \frac{a X_2}{b}, X_2, X_3\right) + \left\langle \frac{\partial}{\partial X_2} U_1 \right\rangle a + 2 \left\langle \frac{\partial}{\partial X_2} U_2 \right\rangle b$$

$$U_3\left(\frac{3}{2}a - \frac{a X_2}{b}, -X_2 + 2b, X_3\right) = U_3\left(-\frac{1}{2}a + \frac{a X_2}{b}, X_2, X_3\right)$$

(10) If some of the displacement relations are trivially satisfied, the equation $\sigma(X^A) = \gamma c \cdot \sigma(X^B) \cdot c^T$ is used to find the traction boundary condition, although that is not the case at hand.

Using a similar exercise all the parameters are found for different combinations of the subcell M with adjoining subcells. The parameters are tabulated for loading case $\langle \sigma_{11} \rangle$ in Table 2.5. Plugging the parameters into the Equation 2.23 gives the multi-point constraint relationships for all the faces of the subcell M. The boundary conditions are imposed on the paired regions as labeled by the paired letters in Figure 2.20 through multipoint constraints. Figure 2.20 shows a typical finite element model. The elements are outlined lightly. The dark lines and labeling indicate the coupling between the four vertical faces of the model. The boundary conditions for the top and bottom were found by going through exactly the same exercise as above and are relatively simpler. Hence, they are not shown in the Figures 2.18 and 2.20 to reduce the clutter in the figures.

For example, the displacements on the partial planes E and $\overline{\text{E}}$ are related through the multi-point constraints, which mean the displacements on one face are slave (dependent) to the displacements on the other face. As is obvious from the Figure2.20, the boundary conditions are a bit unusual and are not intuitively obvious.

Following a similar approach, the boundary conditions for other loading conditions like $\langle \sigma_{22} \rangle, \langle \sigma_{33} \rangle, \langle \sigma_{12} \rangle, \langle \sigma_{23} \rangle$ and $\langle \sigma_{31} \rangle$ can be also found. By using these six loading cases, the complete set of effective engineering properties for the 2x2 braids can be found. The complete set of BC's is given in Table 2.6.

Table 2.5. Parameters describing the relationships between each pair of equivalent subcells of 2x2 braid under loading condition $\langle \sigma_{11} \rangle$

Parameters	M and A	M and B	M and C	M and E	M and F
$\mathbf{c} = \mathbf{a}^T \cdot \mathbf{b}$	$\begin{bmatrix} 1 & 0 & 0 \\ 0 & 1 & 0 \\ 0 & 0 & 1 \end{bmatrix}$	$\begin{bmatrix} -1 & 0 & 0 \\ 0 & -1 & 0 \\ 0 & 0 & 1 \end{bmatrix}$	$\begin{bmatrix} -1 & 0 & 0 \\ 0 & -1 & 0 \\ 0 & 0 & 1 \end{bmatrix}$	$\begin{bmatrix} -1 & 0 & 0 \\ 0 & -1 & 0 \\ 0 & 0 & 1 \end{bmatrix}$	$\begin{bmatrix} -1 & 0 & 0 \\ 0 & -1 & 0 \\ 0 & 0 & 1 \end{bmatrix}$
$\mathbf{X}^{ox}$	$\{-a \quad 0 \quad 0\}$	$\{0 \quad 0 \quad 0\}$	$\{a \quad 0 \quad 0\}$	$\{2a \quad 2b \quad 0\}$	$\{a \quad 2b \quad 0\}$
$\mathbf{X}^{oy}$	$\{0 \quad 0 \quad 0\}$	$\{0 \quad 0 \quad 0\}$	$\{0 \quad 0 \quad 0\}$	$\{0 \quad 0 \quad 0\}$	$\{0 \quad 0 \quad 0\}$
$\mathbf{d} = \mathbf{X}^{ox} - \mathbf{c} \cdot \mathbf{X}^{oy}$	$\{-a \quad 0 \quad 0\}$	$\{0 \quad 0 \quad 0\}$	$\{a \quad 0 \quad 0\}$	$\{2a \quad 2b \quad 0\}$	$\{a \quad 2b \quad 0\}$
$\mathbf{X}^B$	$\left\{\frac{a}{2} + \frac{aX_2}{b}, X_2, X_3\right\}$	$\left\{-\frac{aX_2}{b}, X_2, X_3\right\}$	$\left\{\frac{a}{2} + \frac{aX_2}{b}, X_2, X_3\right\}$	$\left\{2a - \frac{aX_2}{b}, X_2, X_3\right\}$	$\left\{-\frac{a}{2} + \frac{aX_2}{b}, X_2, X_3\right\}$
$\mathbf{X}^A = \mathbf{c} \cdot \mathbf{X}^B + \mathbf{d}$	$\left\{-\frac{a}{2} + \frac{aX_2}{b}, X_2, X_3\right\}$	$\left\{\frac{aX_2}{b}, -X_2, X_3\right\}$	$\left\{\frac{a}{4} - \frac{aX_2}{b}, -X_2 - \frac{b}{4}, X_3\right\}$	$\left\{\frac{aX_2}{b}, -X_2 + 2b, X_3\right\}$	$\left\{\frac{3a}{2} - \frac{aX_2}{b}, -X_2 + 2b, X_3\right\}$
$(\mathbf{X}^{ox} - \mathbf{X}^{oy})$ $+ \mathbf{c} \cdot (\mathbf{X}^{ox} - \mathbf{X}^{oy})$	$\{0 \quad 0 \quad 0\}$	$\{0 \quad 0 \quad 0\}$	$\{0 \quad 0 \quad 0\}$	$\{0 \quad 0 \quad 0\}$	$\{0 \quad 0 \quad 0\}$
γ	1	1	1	1	1
$\mathbf{R}$	$\{0 \quad 0 \quad 0\}$	$\{0 \quad 0 \quad 0\}$	$\{0 \quad 0 \quad 0\}$	$\{0 \quad 0 \quad 0\}$	$\{0 \quad 0 \quad 0\}$

* **b** = Identity matrix

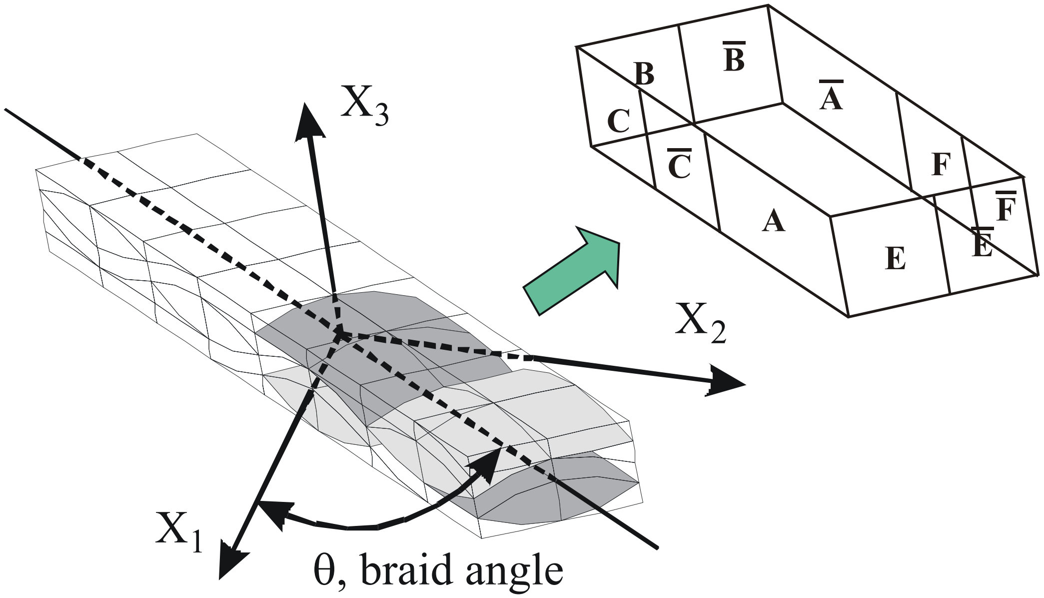

Figure 2.20. A coarse finite element mesh of the full unit cell.

The half unit cell model is the region in which the matrix pockets are shown transparent.

Multipoint constraints are imposed on the paired regions (e.g. A and $\overline{A}$, B and $\overline{B}$, etc.)

Table 2.6. Multipoint constraint relationships for all loading cases for 2x2 braids

$$\langle \frac{\partial}{\partial X_1} u_1 \rangle , \langle \frac{\partial}{\partial X_2} u_1 \rangle , \langle \frac{\partial}{\partial X_2} u_2 \rangle , \langle \frac{\partial}{\partial X_3} u_3 \rangle$$

Figure	Subcells (Fig. 2.18)	Faces (Fig. 2.20)	Multi-point Constraint Relationships
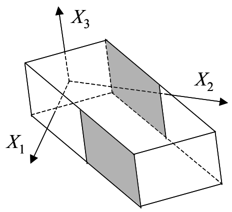	M and A	A and $\overline{\text{A}}$	$u_1\left(-\frac{1}{2}a+\frac{a X_2}{b}, X_2, X_3\right)=u_1\left(\frac{1}{2}a+\frac{a X_2}{b}, X_2, X_3\right)-\langle \frac{\partial}{\partial X_1}u_1 \rangle \ a$ $u_2\left(-\frac{1}{2}a+\frac{a X_2}{b}, X_2, X_3\right)=u_2\left(\frac{1}{2}a+\frac{a X_2}{b}, X_2, X_3\right)-\langle \frac{\partial}{\partial X_2}u_1 \rangle \ a$ $u_3\left(-\frac{1}{2}a+\frac{a X_2}{b}, X_2, X_3\right)=u_3\left(\frac{1}{2}a+\frac{a X_2}{b}, X_2, X_3\right)$
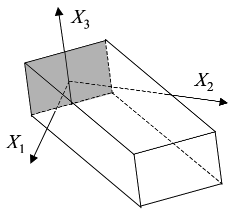	M and B	B and $\overline{\text{B}}$	$u_1\left(\frac{a X_2}{b}, -X_2, X_3\right)=-u_1\left(-\frac{a X_2}{b}, X_2, X_3\right)$ $u_2\left(\frac{a X_2}{b}, -X_2, X_3\right)=-u_2\left(-\frac{a X_2}{b}, X_2, X_3\right)$ $u_3\left(\frac{a X_2}{b}, -X_2, X_3\right)=u_3\left(-\frac{a X_2}{b}, X_2, X_3\right)$
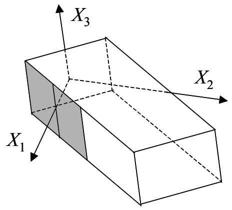	M and C	C and $\overline{\text{C}}$	$u_1\left(\frac{1}{4}a-\frac{a X_2}{b}, -X_2-\frac{1}{4}b, X_3\right)=-u_1\left(\frac{1}{2}a+\frac{a X_2}{b}, X_2, X_3\right)+\frac{3}{4}\langle \frac{\partial}{\partial X_1}u_1 \rangle \ a-\frac{1}{4}\langle \frac{\partial}{\partial X_2}u_1 \rangle \ b$ $u_2\left(\frac{1}{4}a-\frac{a X_2}{b}, -X_2-\frac{1}{4}b, X_3\right)=-u_2\left(\frac{1}{2}a+\frac{a X_2}{b}, X_2, X_3\right)+\frac{3}{4}\langle \frac{\partial}{\partial X_2}u_1 \rangle \ a-\frac{1}{4}\langle \frac{\partial}{\partial X_2}u_2 \rangle \ b$ $u_3\left(\frac{1}{4}a-\frac{a X_2}{b}, -X_2-\frac{1}{4}b, X_3\right)=u_3\left(\frac{1}{2}a+\frac{a X_2}{b}, X_2, X_3\right)$

Table 2.6.   Continued

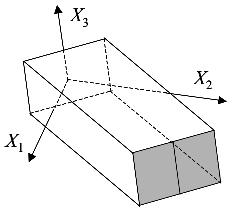	M and E	E and $\overline{\mathrm{E}}$	$u_1\left(\frac{a X_2}{b}, -X_2+2 b, X_3\right)=-u_1\left(2 a-\frac{a X_2}{b}, X_2, X_3\right)+2 \left\langle \frac{\partial}{\partial X_1} u_1 \right\rangle a+2 \left\langle \frac{\partial}{\partial X_2} u_1 \right\rangle b$ $u_2\left(\frac{a X_2}{b}, -X_2+2 b, X_3\right)=-u_2\left(2 a-\frac{a X_2}{b}, X_2, X_3\right)+2 \left\langle \frac{\partial}{\partial X_2} u_1 \right\rangle a+2 \left\langle \frac{\partial}{\partial X_2} u_2 \right\rangle b$ $u_3\left(\frac{a X_2}{b}, -X_2+2 b, X_3\right)=u_3\left(2 a-\frac{a X_2}{b}, X_2, X_3\right)$
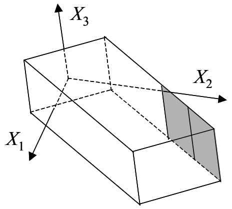	M and F	F and $\overline{\mathrm{F}}$	$u_1\left(\frac{3}{2} a-\frac{a X_2}{b}, -X_2+2 b, X_3\right)=-u_1\left(-\frac{1}{2} a+\frac{a X_2}{b}, X_2, X_3\right)+\left\langle \frac{\partial}{\partial X_1} u_1 \right\rangle a+2 \left\langle \frac{\partial}{\partial X_2} u_1 \right\rangle b$ $u_2\left(\frac{3}{2} a-\frac{a X_2}{b}, -X_2+2 b, X_3\right)=-u_2\left(-\frac{1}{2} a+\frac{a X_2}{b}, X_2, X_3\right)+\left\langle \frac{\partial}{\partial X_2} u_1 \right\rangle a+2 \left\langle \frac{\partial}{\partial X_2} u_2 \right\rangle b$ $u_3\left(\frac{3}{2} a-\frac{a X_2}{b}, -X_2+2 b, X_3\right)=u_3\left(-\frac{1}{2} a+\frac{a X_2}{b}, X_2, X_3\right)$
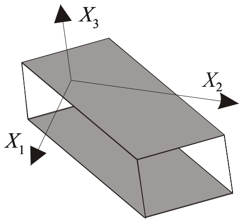	Simple Stacking	Top & Bottom	$u_1\left(X_1, X_2, \frac{1}{2} t\right)=u_1\left(X_1, X_2, -\frac{1}{2} t\right)$ $u_2\left(X_1, X_2, \frac{1}{2} t\right)=u_2\left(X_1, X_2, -\frac{1}{2} t\right)$ $u_3\left(X_1, X_2, \frac{1}{2} t\right)=u_3\left(X_1, X_2, -\frac{1}{2} t\right)+\left\langle \frac{\partial}{\partial X_3} u_3 \right\rangle t$
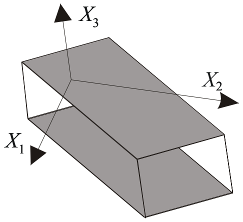	Symmetric Stacking	Top & Bottom	$T_1\left(X_1, X_2, \frac{1}{2} t\right)=0$ $T_2\left(X_1, X_2, \frac{1}{2} t\right)=0$ $u_3\left(X_1, X_2, \frac{1}{2} t\right)=\frac{1}{2} \left\langle \frac{\partial}{\partial X_3} u_3 \right\rangle t$

Table 2.6. Continued

$$\left\langle \frac{\partial}{\partial X_3} u_1 \right\rangle, \ \left\langle \frac{\partial}{\partial X_3} u_2 \right\rangle$$

Figure	Subcells (Fig. 2.19)	Faces (Fig. 2.20)	Multi-point Constraint Relationships
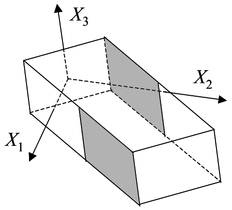	M and A	A and $\overline{\text{A}}$	$u_1\left(-\frac{1}{2}a+\frac{a X_2}{b}, X_2, X_3\right)=u_1\left(\frac{1}{2}a+\frac{a X_2}{b}, X_2, X_3\right)$ $u_2\left(-\frac{1}{2}a+\frac{a X_2}{b}, X_2, X_3\right)=u_2\left(\frac{1}{2}a+\frac{a X_2}{b}, X_2, X_3\right)$ $u_3\left(-\frac{1}{2}a+\frac{a X_2}{b}, X_2, X_3\right)=u_3\left(\frac{1}{2}a+\frac{a X_2}{b}, X_2, X_3\right)-\left\langle \frac{\partial}{\partial X_3} u_1 \right\rangle a$
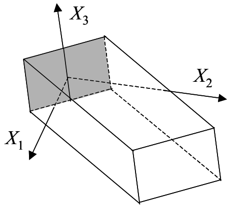	M and B	B and $\overline{\text{B}}$	$u_1\left(\frac{a X_2}{b}, -X_2, X_3\right)=u_1\left(-\frac{a X_2}{b}, X_2, X_3\right)$ $u_2\left(\frac{a X_2}{b}, -X_2, X_3\right)=u_2\left(-\frac{a X_2}{b}, X_2, X_3\right)$ $u_3\left(\frac{a X_2}{b}, -X_2, X_3\right)=-u_3\left(-\frac{a X_2}{b}, X_2, X_3\right)$
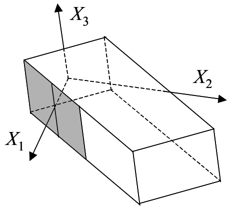	M and C	C and $\overline{\text{C}}$	$u_1\left(\frac{1}{4}a-\frac{a X_2}{b}, -X_2-\frac{1}{4}b, X_3\right)=u_1\left(\frac{1}{2}a+\frac{a X_2}{b}, X_2, X_3\right)$ $u_2\left(\frac{1}{4}a-\frac{a X_2}{b}, -X_2-\frac{1}{4}b, X_3\right)=u_2\left(\frac{1}{2}a+\frac{a X_2}{b}, X_2, X_3\right)$ $u_3\left(\frac{1}{4}a-\frac{a X_2}{b}, -X_2-\frac{1}{4}b, X_3\right)=-u_3\left(\frac{1}{2}a+\frac{a X_2}{b}, X_2, X_3\right)+\frac{3}{4}\left\langle \frac{\partial}{\partial X_3} u_1 \right\rangle a-\frac{1}{4}\left\langle \frac{\partial}{\partial X_3} u_2 \right\rangle b$

Table 2.6. Continued

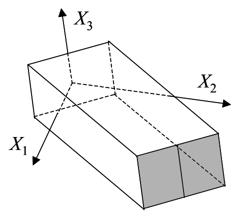	M and E	E and $\overline{\text{E}}$	$u_1\left(\frac{a X_2}{b}, -X_2 + 2 b, X_3\right) = u_1\left(2 a - \frac{a X_2}{b}, X_2, X_3\right)$ $u_2\left(\frac{a X_2}{b}, -X_2 + 2 b, X_3\right) = u_2\left(2 a - \frac{a X_2}{b}, X_2, X_3\right)$ $u_3\left(\frac{a X_2}{b}, -X_2 + 2 b, X_3\right) = -u_3\left(2 a - \frac{a X_2}{b}, X_2, X_3\right) + 2 \langle \frac{\partial}{\partial X_3} u_1 \rangle a + 2 \langle \frac{\partial}{\partial X_3} u_2 \rangle b$
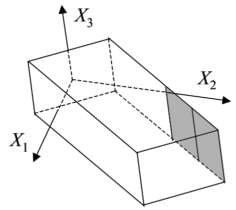	M and F	F and $\overline{\text{F}}$	$u_1\left(\frac{3}{2} a - \frac{a X_2}{b}, -X_2 + 2 b, X_3\right) = u_1\left(-\frac{1}{2} a + \frac{a X_2}{b}, X_2, X_3\right)$ $u_2\left(\frac{3}{2} a - \frac{a X_2}{b}, -X_2 + 2 b, X_3\right) = u_2\left(-\frac{1}{2} a + \frac{a X_2}{b}, X_2, X_3\right)$ $u_3\left(\frac{3}{2} a - \frac{a X_2}{b}, -X_2 + 2 b, X_3\right) = -u_3\left(-\frac{1}{2} a + \frac{a X_2}{b}, X_2, X_3\right) + \langle \frac{\partial}{\partial X_3} u_1 \rangle a + 2 \langle \frac{\partial}{\partial X_3} u_2 \rangle b$
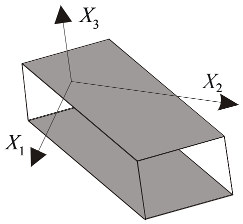	Simple Stacking	Top & Bottom	$u_1\left(X_1, X_2, \frac{1}{2} t\right) = u_1\left(X_1, X_2, -\frac{1}{2} t\right) + \langle \frac{\partial}{\partial X_3} u_1 \rangle t$ $u_2\left(X_1, X_2, \frac{1}{2} t\right) = u_2\left(X_1, X_2, -\frac{1}{2} t\right) + \langle \frac{\partial}{\partial X_3} u_2 \rangle t$ $u_3\left(X_1, X_2, \frac{1}{2} t\right) = u_3\left(X_1, X_2, -\frac{1}{2} t\right)$
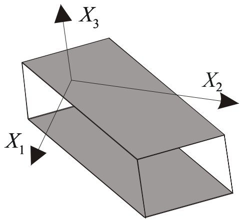	Symmetric Stacking	Top & Bottom	$u_1\left(X_1, X_2, \frac{1}{2} t\right) = \frac{1}{2} \langle \frac{\partial}{\partial X_3} u_1 \rangle t$ $u_2\left(X_1, X_2, \frac{1}{2} t\right) = \frac{1}{2} \langle \frac{\partial}{\partial X_3} u_2 \rangle t$ $T_3\left(X_1, X_2, \frac{1}{2} t\right) = 0$

To check the boundary conditions, the finite element models for both the half and quarter unit cells were developed and analyzed for a symmetrically stacked composite. The half unit cell is a reasonable substitute for the full unit cell model as a reference since the boundary conditions on the top and bottom of the model are extremely simple. Figure 2.21 shows "in-plane" shear stress contours for the tows in half and quarter unit cell models. The matrix pockets are removed so that the tows can be seen. The loading is uniaxial and is aligned such that the tows are at an angle of ±20° relative to the load direction. Note that the stress distribution in the smaller model is identical to that in the lower part of the larger model. Also, the stress distribution in the other part of the larger model can be determined from that in the smaller model. Finally, because of the symmetry in both the loading and the tow orientations, the stress distributions in the +20° tow should be related to that in the -20° tow. The contours in Figure 2.21 show that is the case.

2.5 Material systems used

Two material systems were used for the parametric studies. One consists of S2-Glass fibers and SC-15 Epoxy resin. The other consists of AS4 Carbon fibers and 411-350 Derakane Momentum matrix. The 411-350 or Derakane momentum is also called Vinyl Ester. The tow consists of resin and fibers. A typical tow consists of 10K fibers. The glass fiber is isotropic whereas carbon fibers are transversely isotropic. The matrix is purely isotropic for both the material systems. The fibers are assumed to be arranged in a hexagonal array [Figure 2.22] in the matrix in the tow, which makes the tow transversely isotropic. The tow properties were found using three dimensional finite element micromechanics analysis using a code called *"hexcurve"*. One fourth of the unit cell that was used to calculate to the tow properties is shown in Figure 2.23.

The material properties of the fiber, matrix and the tow are given in Table 2.7 for both the material systems.

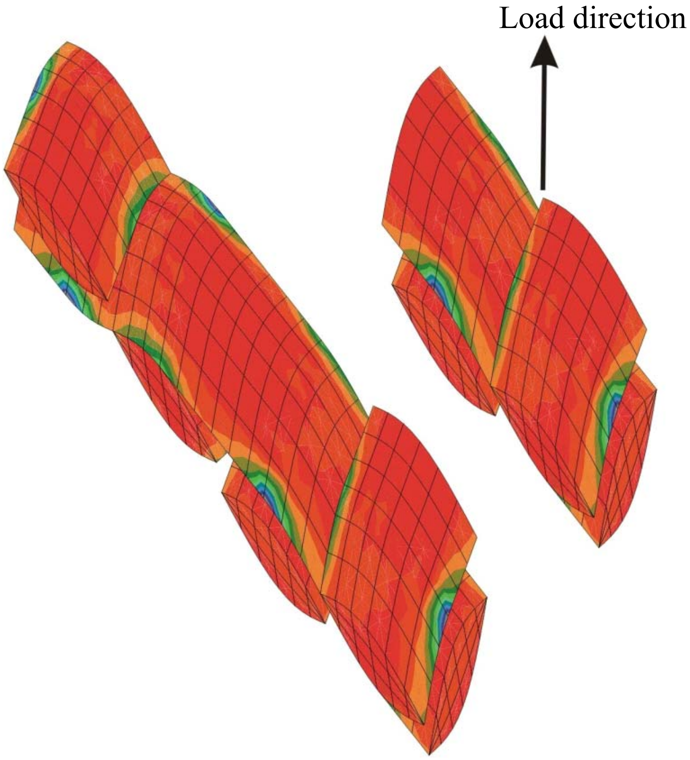

Figure 2.21. Validation of symmetry condition

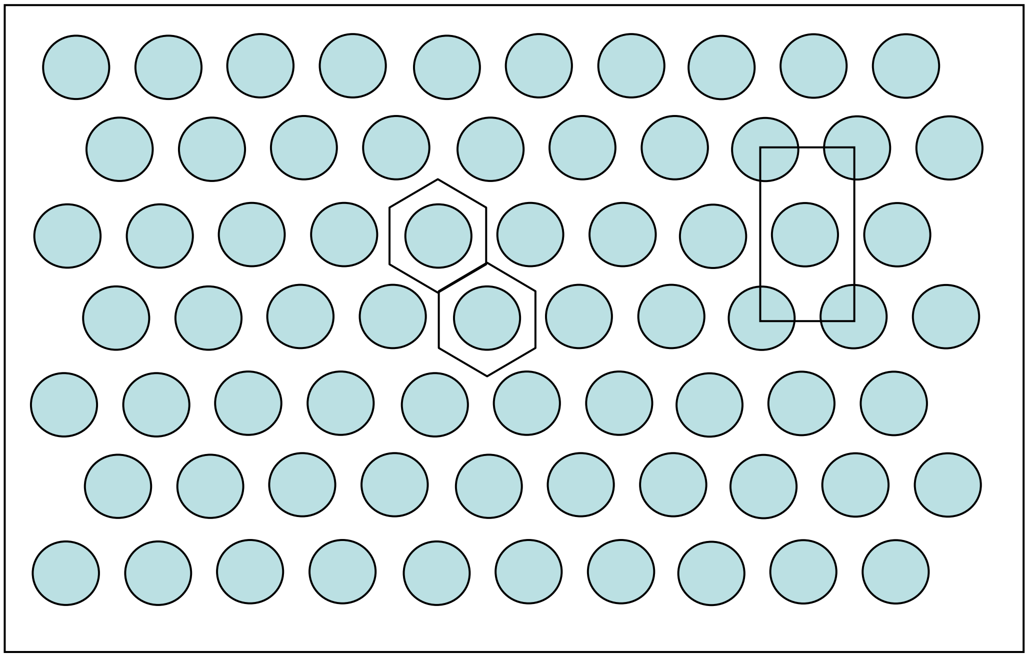

Figure 2.22. Distribution of fibers inside the tow

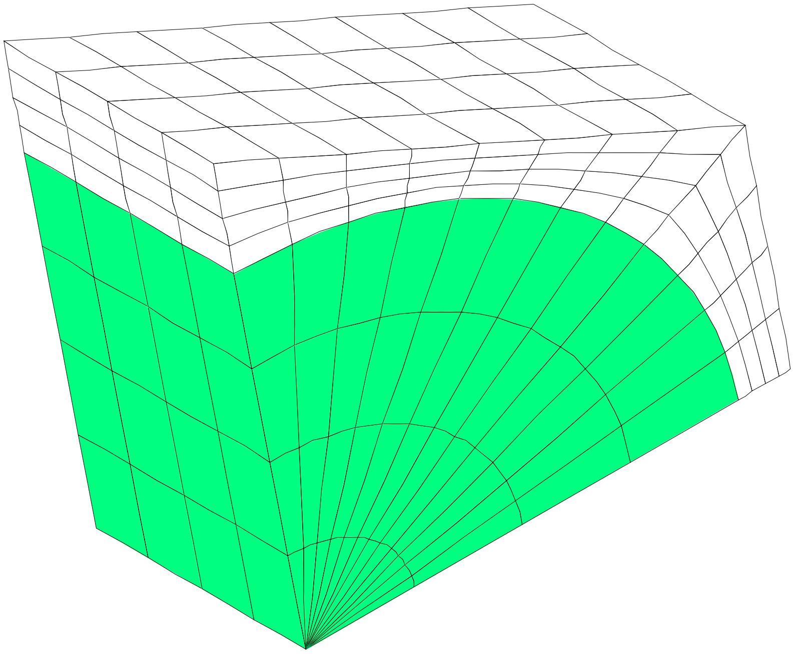

Figure 2.23. Finite element mesh for calculating tow properties

Table 2.7. Material properties for fiber, matrix and tow

(a) For S2/SC-15 material system

Property	Fiber	Resin	Tow[a]
E11	96.53 GPa	2.82 GPa	76.42 GPa
E22	96.53 GPa	2.82 GPa	20.18 GPa
E33	96.53 GPa	2.82 GPa	20.18 GPa
ν12	0.23	0.395	0.2654
ν23	0.23	0.395	0.3352
ν13	0.23	0.395	0.2654
G12	39.23 GPa	1.01 GPa	7.4 GPa
G23	39.23 GPa	1.01 GPa	4.03 GPa
G13	39.23 GPa	1.01 GPa	7.4 GPa

[a] Fiber volume fraction in tow = 0.7854

(b) For AS4/311-450 material system

Property	Fiber	Resin	Tow[a]
E11	228 GPa	3.1 GPa	157.95 GPa
E22	16.54 GPa	3.1 GPa	9.027 GPa
E33	16.54 GPa	3.1 GPa	9.027 GPa
ν12	0.2	0.35	0.2412
ν23	0.25	0.35	0.3749
ν13	0.2	0.35	0.2412
G12	24.82 GPa	1.15 GPa	5.12 GPa
G23	6.89 GPa	1.15 GPa	3.34 GPa
G13	24.82 GP	1.15 GPa	5.12 GPa

[b] Fiber volume fraction in tow = 0.69

2.6 Summary

In this section, the solid model and finite element models of 2x2 braids were discussed. As the braid tow cross-section varies unusually, direct mesh generation for braids is quite complex. Similarities that exist between the twill and the 2x2 braid were exploited and a mapping technique was used to produce the models of braid from the models of the twill that had already been developed in previous studies. The equations defining the tow path of the braids were given. The symmetries that exist within the unit cell of the 2x2 braid were exploited to reduce the analysis region. The boundary conditions that involve numerous multipoint constraint relationships were derived using a general technique to exploit periodicity and symmetry [27].

3. RESULTS AND DISCUSSION

3.1 Introduction

In order to characterize the mechanical behavior of braided composites, we need to find their effective engineering properties. A full three-dimensional stress state exists in braids and their stress analysis needs to be performed to predict the potential damage spots. In this section, we will study the effect of various parameters like braid angle, waviness ratio, tow cross-section, stacking sequence and material properties on the effective engineering properties of the 2x2 braids. Then the predictions of the finite element analyses will be compared with the predictions of a simple 3D laminate analysis. Braid tows run at an angle of $+\theta$ and $-\theta$, so a laminate configuration essentially consists of two unidirectional laminas (with properties of the tow) in $+\theta$ and $-\theta$ direction with a third layer as matrix to account for matrix pockets in the braid. Lastly, the three-dimensional stress state that exists in braids will be predicted. The effect of braid angle on location and magnitude of the peak stresses will be determined in order to locate the potential damage spots for different braids.

The effect of various parameters like braid angle, waviness ratio, stacking sequence and material system on the effective engineering properties (E_{11}, E_{22}, E_{33}, υ_{12}, υ_{23}, υ_{13}, G_{12}, G_{23}, G_{13}) of the braids is discussed. Extensive parametric studies were conducted to find the effective properties for a wide range of braid angles (BA) and waviness ratio's (WR). Two material systems were considered in the studies: S2/SC15 glass/epoxy material and AS4/411-350 carbon/vinyl ester. The properties of both the material systems were given in the previous chapter. The braid angle can vary from 15° to 75° [9]. Hence, the properties were calculated for this range of the braid angle. Although the realistic range of waviness ratio is 1/15 to 1/9, a wider range of 1/30 (very flat) to 1/3 (very wavy) was chosen to see what happens at very low and very high waviness ratios and whether the behavior reaches that of the laminate at very low waviness ratio. Extensive parametric studies were conducted for symmetric stacking of mats and then the spot checks were done for simple stacking sequence, for properties that had high sensitivity to changes in braid angle and waviness ratio. The effect of various parameters on the effective properties will be discussed in terms of the sensitivity of the properties to change in waviness ratio and braid angle and in terms of the deviation of the predictions from laminate theory.

If the braid angle is ±θ, then its complementary braid angle is defined here to be ±(90-θ). Furthermore, the property pairs (E11, E22), (υ23, υ13) and (G23, G13) are defined to be complementary of each other if the first property in any pair belongs to ±θ braid and second belongs to ±(90-θ) braid. The complementary properties are equal for a laminate. But this is not the case for braids. This effect, which is not intuitively obvious, is due to the difference in material architecture that exists in braids. This difference in material architecture is called "*unbalance*" herein and its effect in the context of advantages in selecting one braid over its complementary braid will be discussed.

Even for the simple loading cases (for example, uniaxial loading), the stress state in braids is complex. A fully three-dimensional stress state exists in both tows and matrix. The characteristic stress distribution will be discussed. This will be useful for identifying the potential damage initiation locations in the braids.

Overall, for both material systems, the effective properties show varying degrees of sensitivity to the change of braid angle and waviness ratio. To have both qualitative and quantitative observation of the results, the following discussion will proceed in terms of the sensitivity of the properties to the change of braid angle and waviness ratio, the deviation of the properties from the value of the laminate theory, the effect due to unbalance in material architecture and the stress distribution in braids. Finally the predictions will be compared with the experimental results.

3.2 Sensitivity of the properties to change in waviness ratio and braid angle

To develop robust simple analytical models or for the optimal design of materials, it is imperative to know the sensitivity of a property to changes in various parameters. Hence, sensitivity of the properties to changes in various parameters is discussed here. Further all the results are compared with the predictions of laminate theory. The reason is that the laminate theory codes are widely available and understood by designers. So it will be seen how much difference it makes if one predicts the properties of the 2x2 braids using an equivalent laminate configuration. Also the properties predicted by three-dimensional FE analysis of braids can be normalized by the laminate predictions to see the exclusive effect of braid angle and waviness ratio. An equivalent laminate configuration is shown in Figure 3.1. The finite element model of 2x2 braids has braid tows that run at an angle of $+\theta$ and $-\theta$ and the matrix pockets. The laminate essentially consists of two layers with the properties of the tow and stacked at $+\theta$ and $-\theta$ orientations. The third layer consists of the properties of the matrix and its orientation does not matter, as the matrix is isotropic for both the material systems under investigations. A three-dimensional finite element analysis was performed for the laminate to be able to predict the out-of-plane properties also.

Figure 3.2 shows the variation of E_{11} with braid angle and waviness ratio for the S2/SC-15 material. The dots in the figure are finite element data. The data were curve fitted in both directions to produce smooth curves to see changes with waviness ratio and braid angle. The outlined curve shows the values for the reference laminate. The figure shows that most of the effect of braid angle on the E_{11} can be predicted using laminate theory. This is the case for other effective properties also. Hence to reveal the exclusive effects of the braid architecture and in order to filter out the braid angle effect that can be predicted by the laminate theory, the results were normalized by the respective value for the reference laminate. The reference laminate values vary with variation in braid angle, but they don't vary with waviness ratio, as there is no waviness in laminate by definition. The following discussion will follow with all the property results normalized by the respective value of the reference laminate.

Figures 3.3 and 3.4 show the normalized effective engineering properties as a function of braid angle and waviness ratio for S2/SC-15 and AS4/411-350, respectively. The range for the waviness change is from 0.03 (very flat) to 0.33 (very wavy) for both

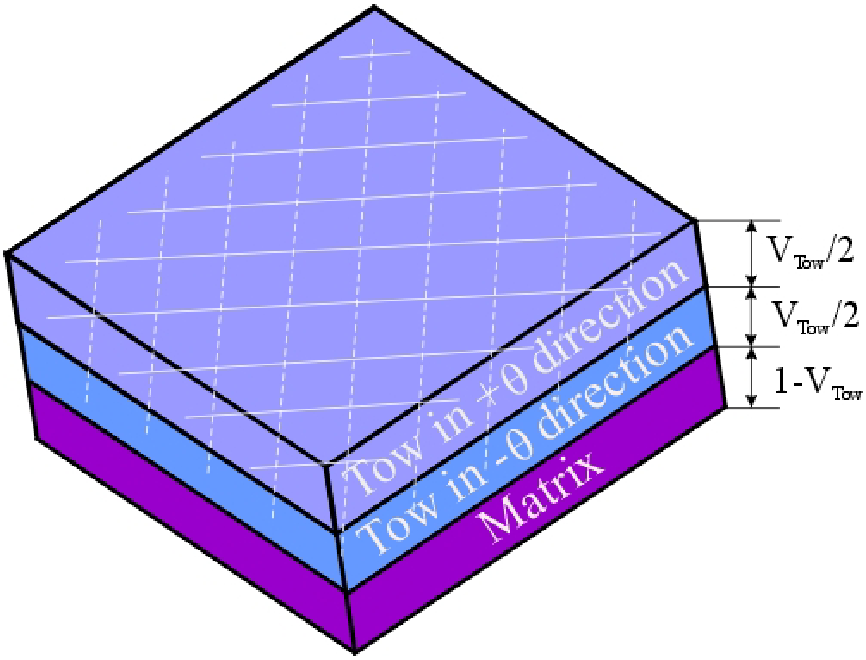

Figure 3.1. An equivalent laminate configuration

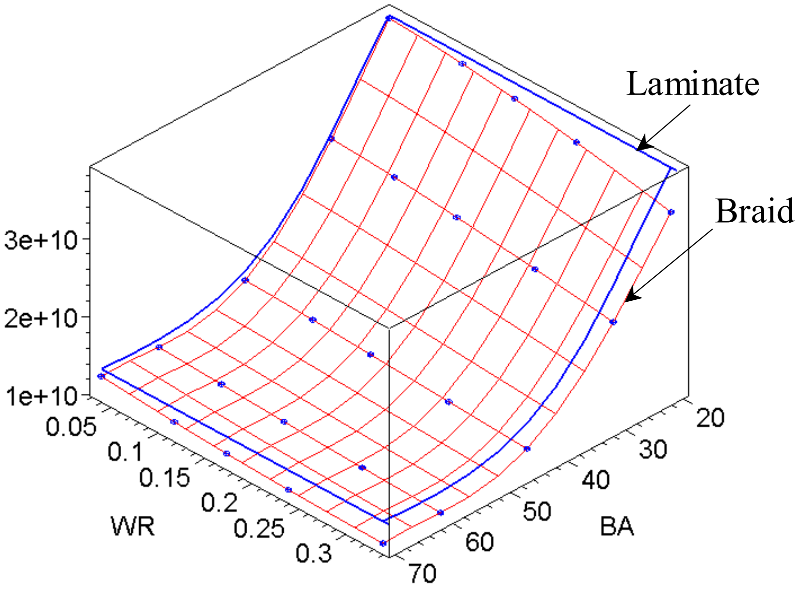

Figure 3.2. Effective longitudinal modulus E11 versus braid angle (BA) and waviness ratio (WR) for S2/SC-15 material. The symbols are the data from the FE analysis.

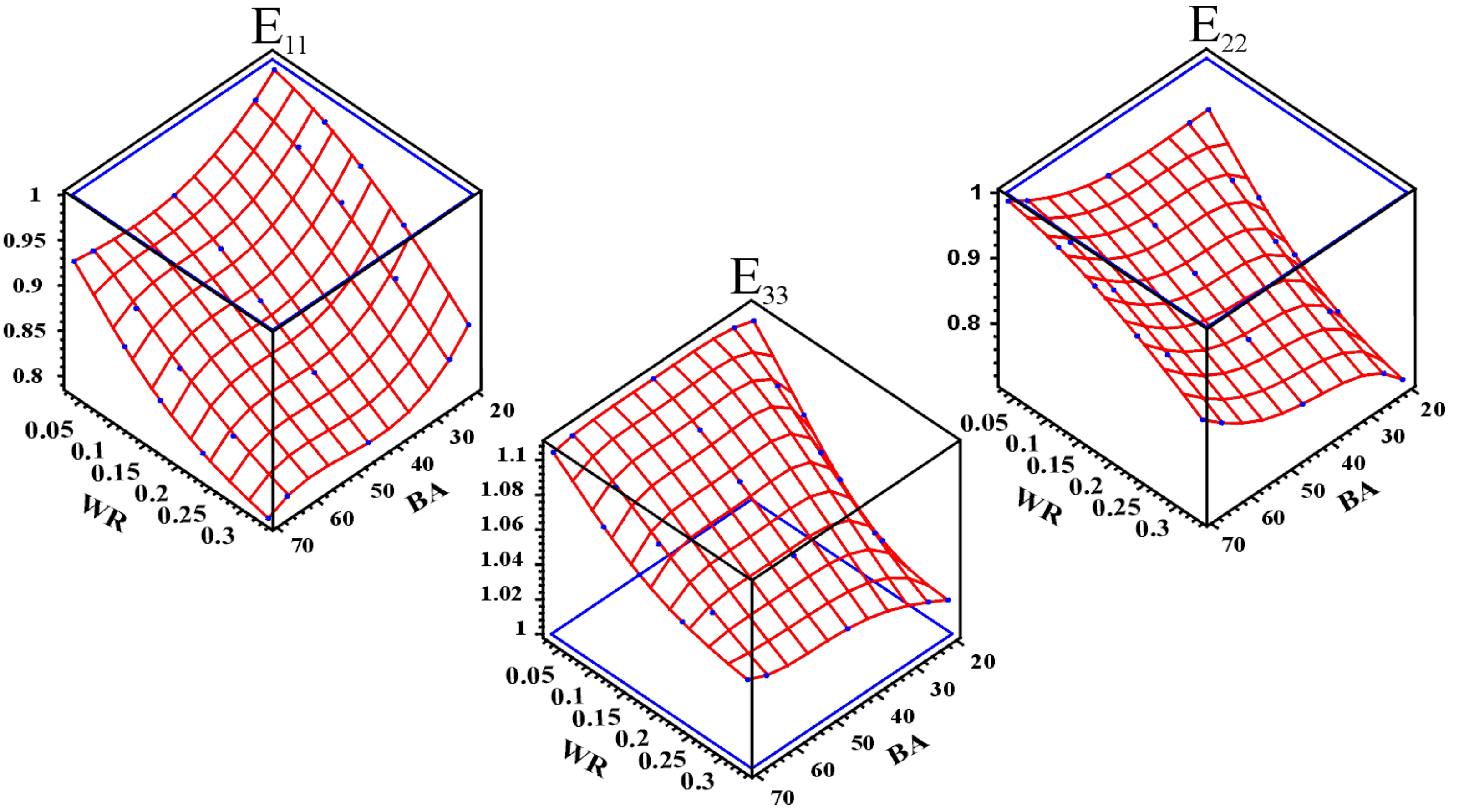

(a) Variation of longitudinal and transverse moduli

Figure 3.3. Normalized effective properties vs braid angle (BA) and waviness ratio (WR) for S2/SC-15 material

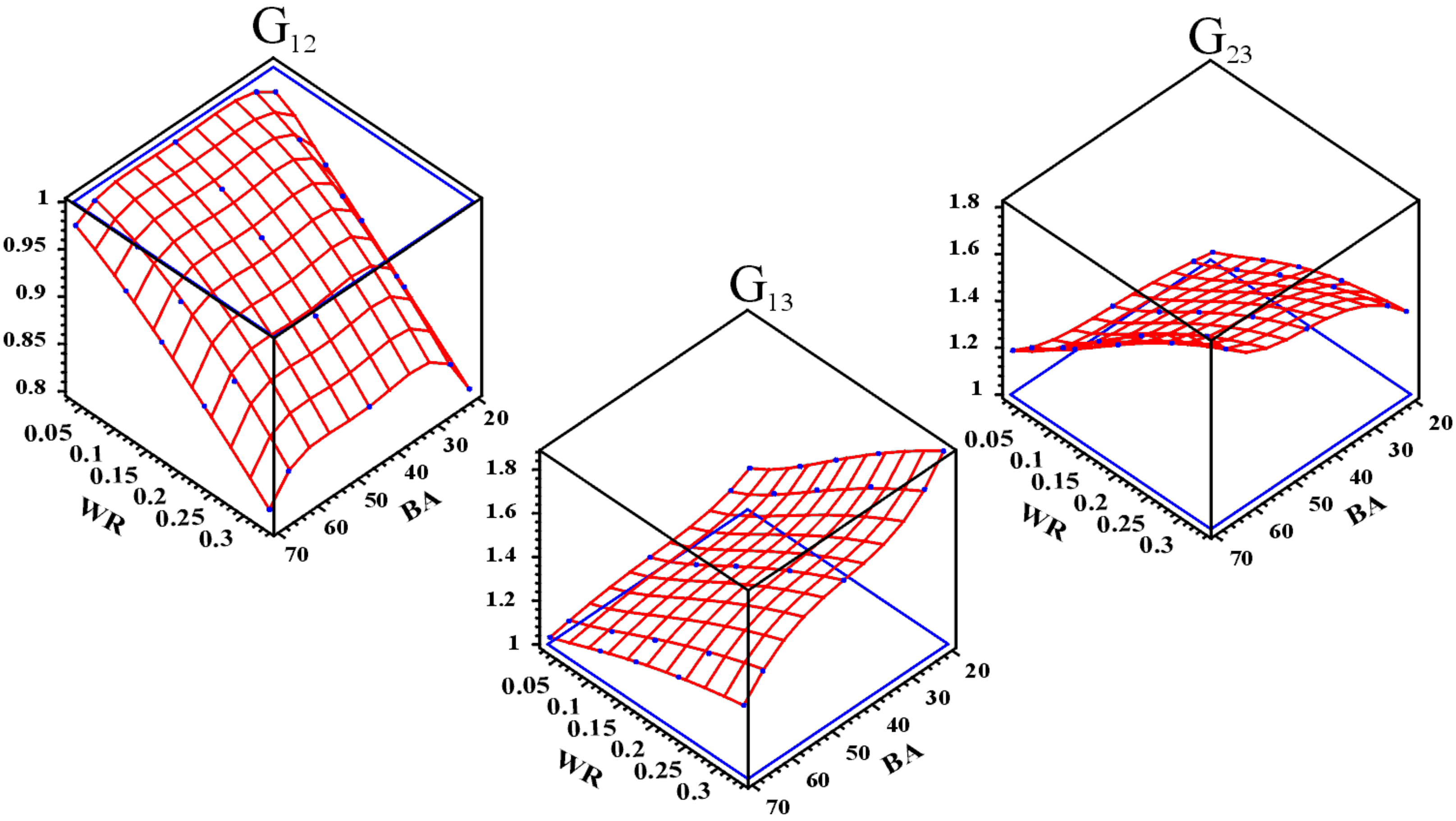

(b) Variation of shear moduli

Figure 3.3. Continued

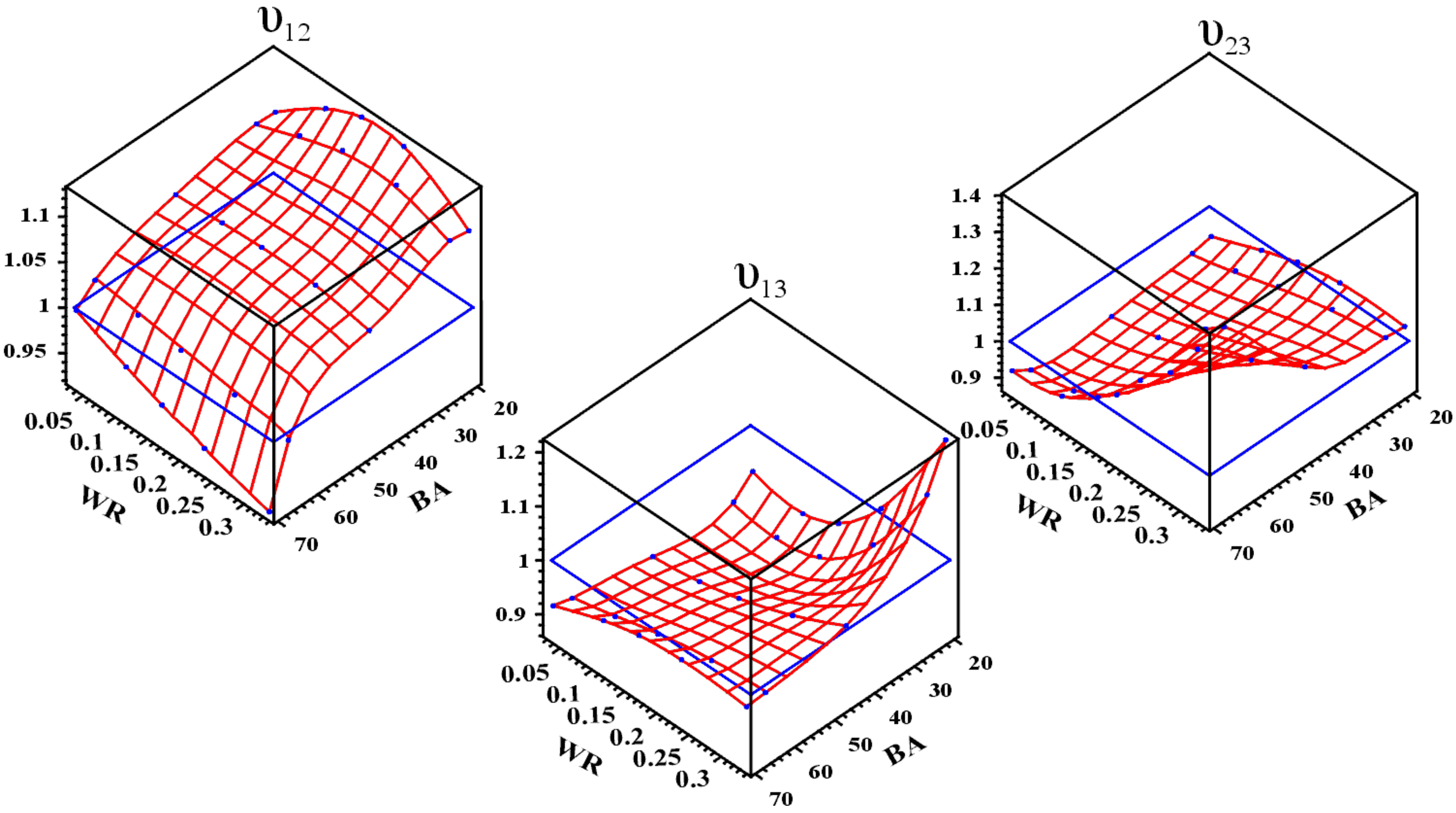

υ_{12}

υ_{13}

υ_{23}

(b) Variation of Poisson's ratio

Figure 3.3. Continued

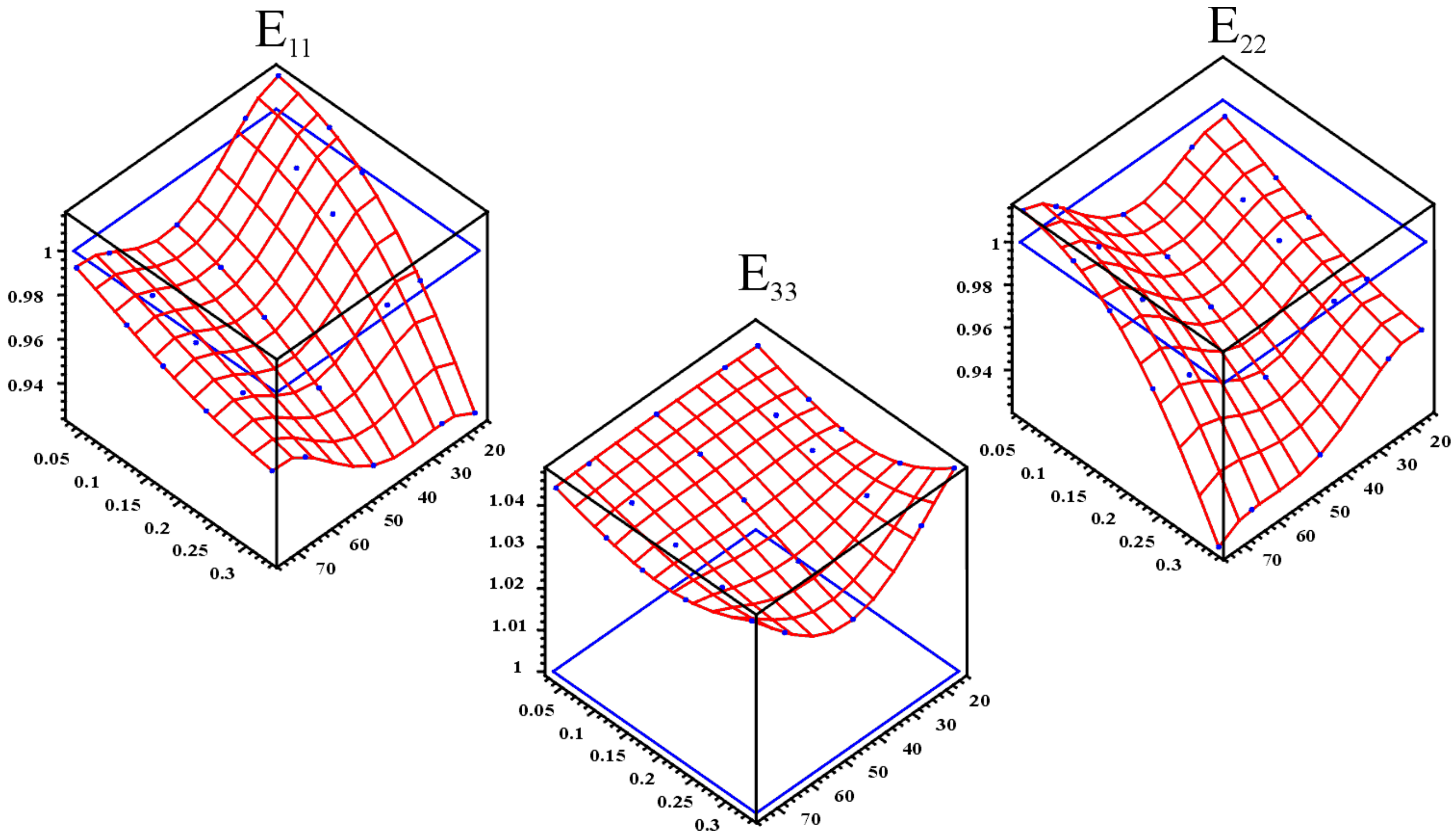

(a) Variation of longitudinal and transverse moduli

Figure 3.4. Normalized effective properties vs braid angle (BA) and waviness ratio (WR) for AS4/411-350 material

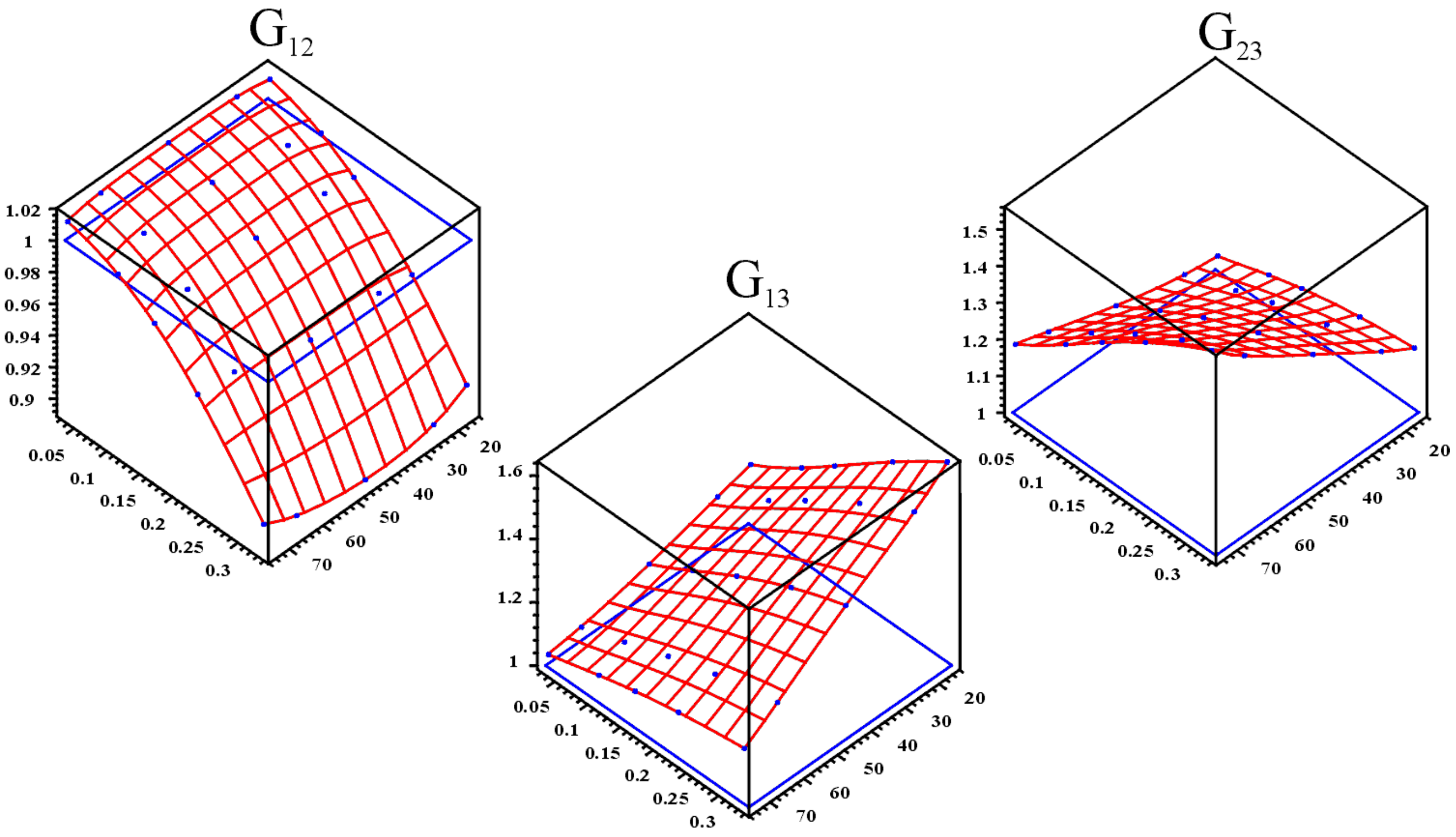

(b) Variation of shear moduli

Figure 3.4. Continued

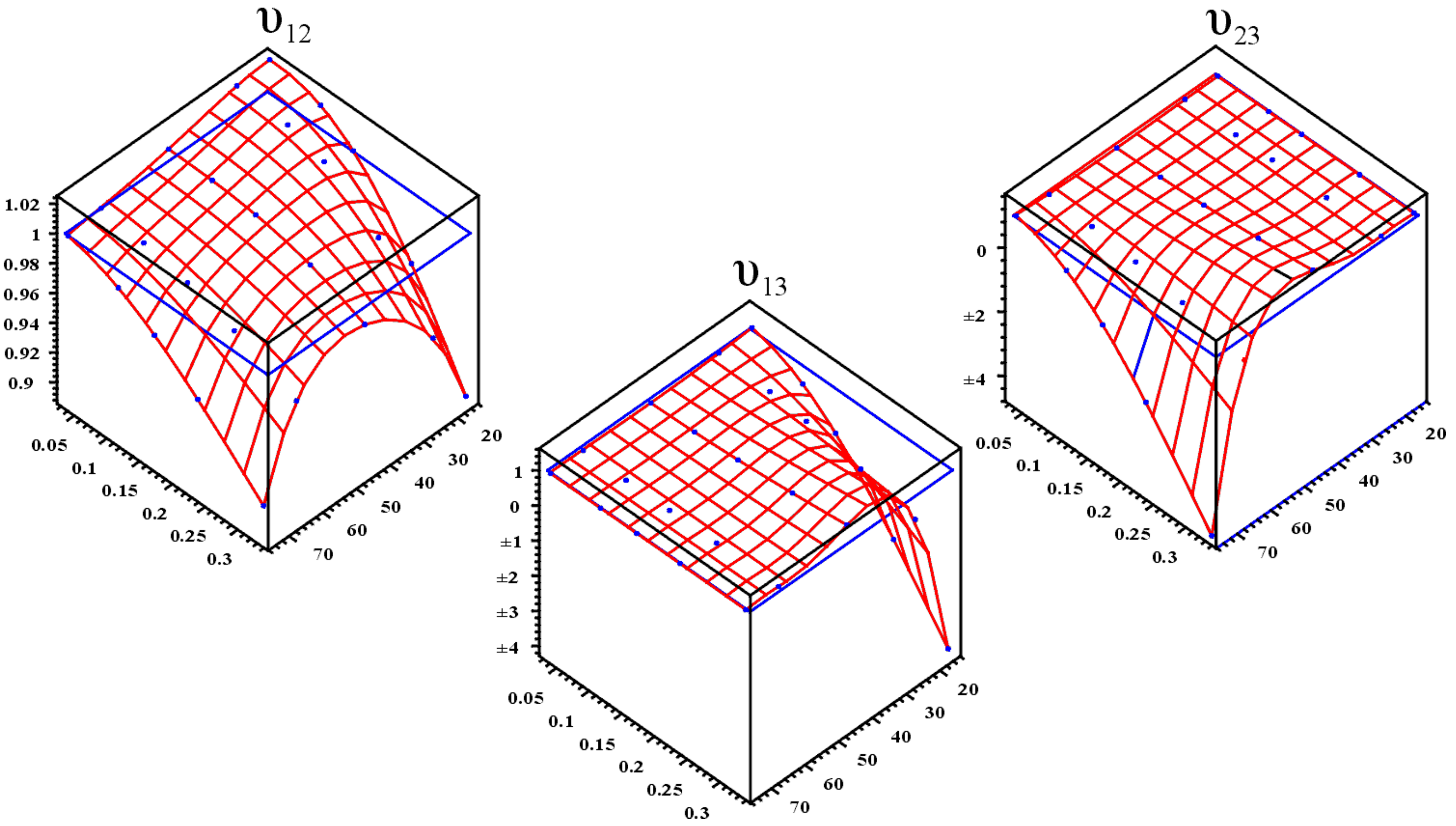

(b) Variation of Poisson’s ratio

Figure 3.4. Continued

materials. The range for the braid angle is 20º~70º for S2/SC-15 and 15º~75º for AS4/411-350.

Figure 3.3 shows that for S2/SC-15 material system, E_{11}, E_{22}, E_{33} and G_{12} decrease while G_{23}, G_{13}, ν_{23} and ν_{13} increases with an increase in waviness ratio for all braid angles. The ν_{12} remains almost constant with waviness ratio for all braid angles. Figure 3.4 shows that for the AS4/411-350 material system, E_{11}, E_{22}, G_{12} and υ_{12} decrease while transverse shear moduli G_{23} and G_{13} increase with an increase in waviness ratio. The E_{33}, ν_{23} and ν_{13} remain almost constant with waviness ratio. It should be noted here that there are cases in which the reference laminate value is extremely small, for example, for ν_{13} and ν_{23} at certain braid angles for AS4/411-350. As a result, a small deviation will result in an extremely large normalized value.

Further, it can be noted from Figures 3.3 and 3.4 that even for very low waviness ratio, the values do not converge to the values predicted by the full 3D laminate model. This is due to the fact that, although the 3D laminate model can account for the braid angle effect, it cannot account for the effect of material distribution in the +θ and –θ tows.

For the sake of discussion, the sensitivity herein is defined as the maximum variation of the normalized effective properties over the range that the parameters (i.e. braid angle and waviness ratio) can change, and is measured by

$$S_E = \left| E^{\max} - E^{\min} \right| * 100\%$$

where $E^{\min}$ and $E^{\max}$ are the *normalized* minimum and maximum property values for the range in which the parameters vary. This simple measure will provide information as to which properties are more sensitive than the others over the considered parameter range.

The sensitivity for both the material systems to change in braid angle and waviness ratio is shown in Table 3.1. For both the material systems, the sensitivity for

Table 3.1. Sensitivity [a] of effective properties to change of braid angle (BA) and waviness ratio (WR)

	BA	WR	S_{E11}	S_{E22}	S_{G12}	S_{v12}	S_{E33}	S_{G13}	S_{G23}	S_{v13}	S_{v23}
S2/SC-15	20°~70°	0.03 to 0.33	20.1	28.1	19.4	20.7	9.1	83.2	77.3	34.4	50.8
AS4/411-350	15°~75°		9.1	9.4	12.6	13.4	1.9	59.1	51.0	554.2	607.5
S2/SC-15	20°~70°	0.03 to 0.11	11.9	15.0	6.0	13.6	4.0	31.9	31.2	8.1	8.9
AS4/411-350	15°~75°		4.1	4.1	1.6	3.4	0.5	25.2	24.7	59.0	61.9

[a] Sensitivity is defined as $S_E=|E^{max} - E^{min}|*100\%$, where E^{min} and E^{max} are the *normalized* minimum and maximum property values for the range in which the parameters vary.

the full range (0.03 – 0.3) of waviness ratio and more realistic range of waviness ratio (0.03 -0.11) is listed separately. The range for the braid angle is 20°~70° for S2/SC-15 and 15°~75° for AS4/411-350. It shows that for any effective property listed, the AS4/411-350 carbon fiber/epoxy material is less sensitive than the S2/SC-15 glass fiber / epoxy material for the same range of waviness ratio (except for the surge in v_{13} and v_{23}, which is due to normalization by nearly zero laminate value). For example, the sensitivity of the in-plane modulus E_{11} is 20.1% for S2/SC-15 for the range of waviness from 0.03 to 0.33, which is about twice as much as for AS4/411-350 (9.1%), even though the AS4/411-350 has a wider range of braid angle.

For S2/SC-15, the sensitivity of all in-plane properties is less than 29% whereas for the AS4/411-350, the sensitivity is less than 15%. The sensitivity of out-of-plane properties can be as high as 83% for S2/SC-15 and 59% for AS4/411-350. It can be seen that the transverse properties (G_{13}, G_{23}, v_{13} and v_{23}) are significantly more sensitive than the in-plane properties (E_{11}, E_{22}, G_{12} and v_{12}). But the out-of-plane modulus E_{33} has the smallest sensitivity (<10% for all the ranges of braid angle and waviness), which means E_{33} is almost insensitive to the change of braid angle and waviness ratio. This insensitivity is because of the fact that through-the-thickness behavior is mainly dominated by the matrix properties.

For the more realistic range of waviness of 0.03 to 0.11, the sensitivity of effective properties decreases significantly. The sensitivity of the in-plane properties is less than 15% for the glass fiber/epoxy resin, while for the carbon fiber/epoxy AS4/411-350, the in-plane properties are quite insensitive (less than 5%) to the change of braid angle and waviness ratio. The out-of-plane modulus E_{33} now becomes almost insensitive (≤4%) to the change of braid angle and waviness for both material systems. However, the transverse properties (G_{13}, G_{23}, v_{13} and v_{23}) are still very sensitive (> 25%) to the braid angle and waviness for both material systems, even though the waviness is small.

3.3 Deviation of the properties from reference laminate values

The deviation of the properties from the respective property of the reference laminate is measured by (E^{extreme} – 1)*100%, where E^{extreme} is either E^{min} or E^{max}, which are the *normalized* minimum and maximum property values for the range in which the parameters vary. Therefore there are lower and upper deviations from laminate theory that correspond to E^{min} and E^{max}. The deviation of properties from laminate theory is plotted in Figures 3.5 – 3.6. The smaller the deviation band, the less is the sensitivity to changes in braid angle and waviness ratio. The closer the extremity of the band to zero, the less is the deviation from laminate theory.

For the full range of waviness ratio (0.03 – 0.11), the deviation of the finite element results from the laminate results for the effective properties is shown in Figure 3.5 for both the material systems. In general, the out-of-plane properties have higher deviation than in-plane properties. Maximum deviation is observed for out-of-plane shear moduli for both the material systems (ignoring the high deviation of out-of-plane Poisson's ratios for the reason mentioned earlier). The maximum deviation is 87% for the S2/SC-15 and around 63% for AS4/411-350 material system and is for G_{13}. The largest deviation (absolute value) of in-plane properties is 11.2% for the AS4/411-350, and 29.1% for the S2/SC-15. In general, the glass fiber/epoxy material has a larger deviation than the carbon fiber/epoxy material for almost all the properties. Since out-of-

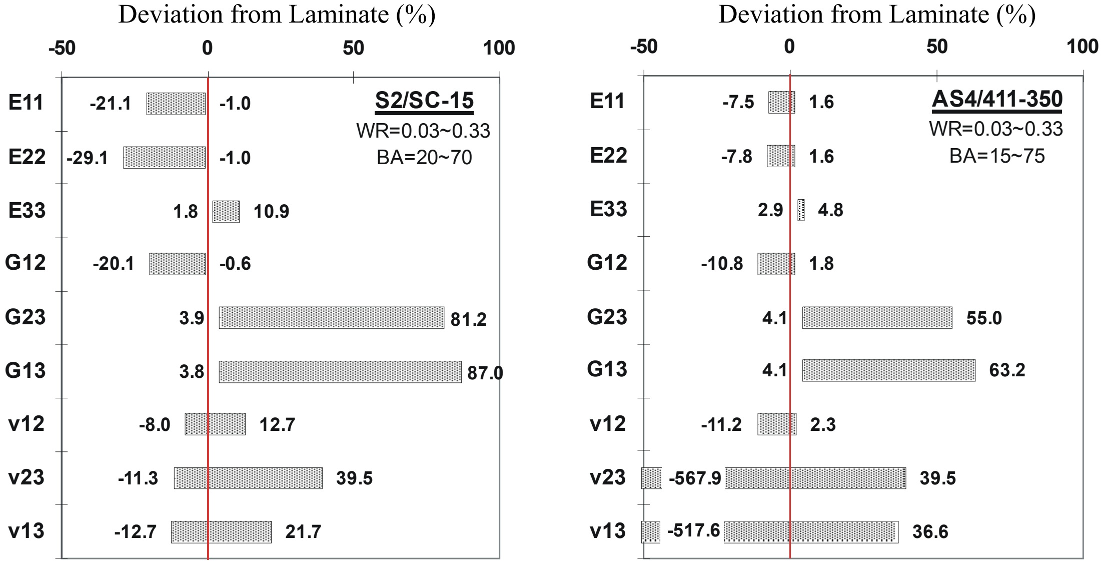

Figure 3.5. Deviation of 3D finite element results from the laminate results. The range of waviness ratio is from 0.03 to 0.33

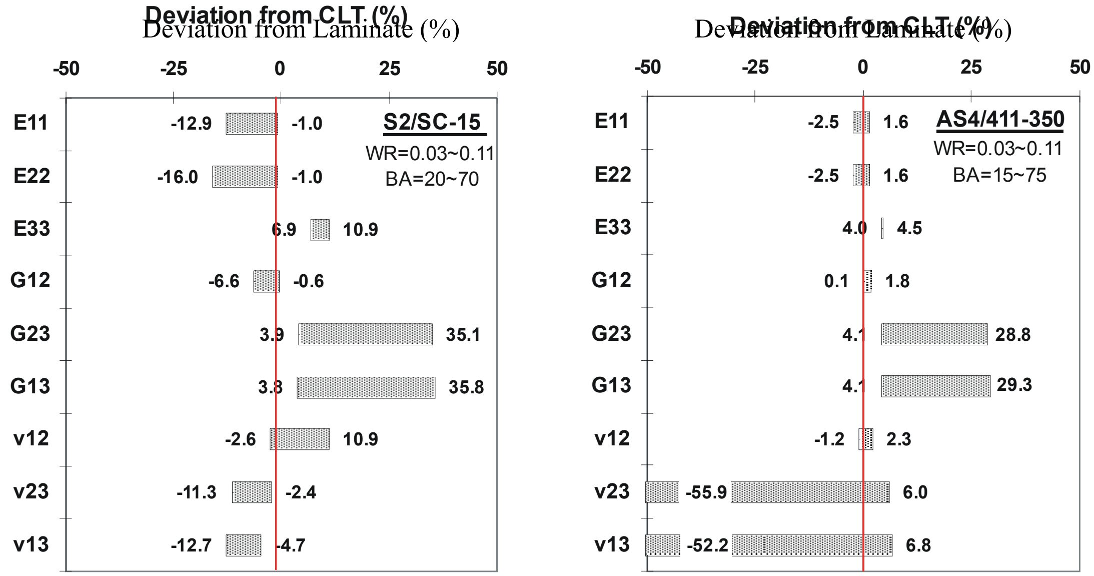

Figure 3.6. Deviation of 3D finite element results from the laminate results. The range of waviness ratio is from 0.03 to 0.11

plane moduli E_{33} has a small deviation from the laminate value, it can be predicted easily using 3-D laminate analysis. The modulus E_{33} has the narrowest deviation band as compared to the other properties for the respective material system. This is consistent with its lowest sensitivity observed in Table 3.1. For the two material systems used in this study, the E33 is larger than the laminate value as obvious from Figure 3.3 and 3.4. In general, the E33 can be more than, equal to, or less than the laminate value, depending on the material system used. For example, for the material system used in [22], the E33 is smaller than the laminate value.

In Figure 3.6, the deviation is shown for the reduced waviness ratio range (0.03~0.11). As the waviness ratio range is reduced, the deviation band (range from lower to upper deviation) also shrinks as compared to Figure 3.6. For AS4/411-350, the in-plane properties ((E_{11}, E_{22}, G_{12} and ν_{12}) can be predicted quite accurately with a maximum error of 2.5%. One does not even have to do three-dimensional laminate analysis to predict in-plane properties of the braids as ordinary laminate theory does a good job to predict the in-plane properties. For the S2/SC-15 material system, the in-plane properties have larger deviation from the laminate predictions. For this material system, the deviation can be as large as 16%, which suggests that simple laminate model may not be a good choice for approximation. So it can be concluded that the use of laminate theory to approximate the properties of the braids is contingent upon the material system under investigation. For the transverse shear properties (G_{13} and G_{23}), the deviation is larger than 29% for both material systems, which suggests the necessity for a more accurate simple analytical model than 3D laminate theory.

3.4 Complementary braids

The properties of complementary braids differ from each other due to an imbalance in material architecture. Here we will see this difference quantitatively. This section discusses the difference in corresponding properties of complementary braids due to different material interlace patterns along the x and y directions.

The values of E11, G23 and ν23 for a particular braid with braid angle ±θ, differ from values of E22, G13 and ν13 respectively for a braid with a corresponding complementary braid angle. The difference is attributed to the fact that the interlace pattern in the X1-direction of a braid with braid angle ±θ is not the same as that in the X2-direction of one with braid angle of ±(90-θ). To illustrate this lets consider twill and a 2x2-45° braid. The material architecture of a 2x2 braid is nominally the same as a twill weave when the braid angle is ±45°. It was observed that the value of $E_{11}^{'}$ and $E_{22}^{'}$ is exactly same (=26.8 GPa) for a twill weave [3] as shown in Figure 3.7. This is due to the fact that material architecture is identical along x and y-axes. Intuitively one would expect the same for a 2x2, ±45° braid also. But, in the case of 2x2 braid, there exists a difference of approximately 3% in the values of E11 and E22 as shown in Figure 3.7(a) (E11 = 12.7 GPa and E22 = 12.3 GPa).

This is because the interlace pattern is same for twill in the X1 and X2 direction, but is different for braid in the two directions. This is shown in Figure 3.7. A + sign in Figure 3.7 (b) indicates a warp tow on the top of a fill tow and a – sign indicates a fill tow on the top of warp tow. As shown in the figure, the pattern is the same (+,+,-,-) in the X1 and X2 direction. Hence the properties in both directions are same. Now lets see the pattern in braids. A + sign in Figure 3.7(c) indicates a +θ braid tow on the top of a –θ tow and a – sign indicates a –θ tow on the top of +θ tow. In Figure 3.7(c), we see the architecture along X2 direction. The figure shows that the pattern is: one +θ tow on top and then one –θ tows on top (+,-,+,-) and repetition of this. On the other hand in X1 direction, all -θ tows are on top. So we see that the braid pattern is different in two directions and hence the property difference exists. Due to the same reason, the value of E11, G23 and ν23 for a particular braid differ from values of E22, G13 and ν13 respectively for a braid with a corresponding complementary braid angle.

Figure 3.8 and 3.9 shows the effect of unbalance in material architecture on the effective properties. The percentage difference is defined here as:

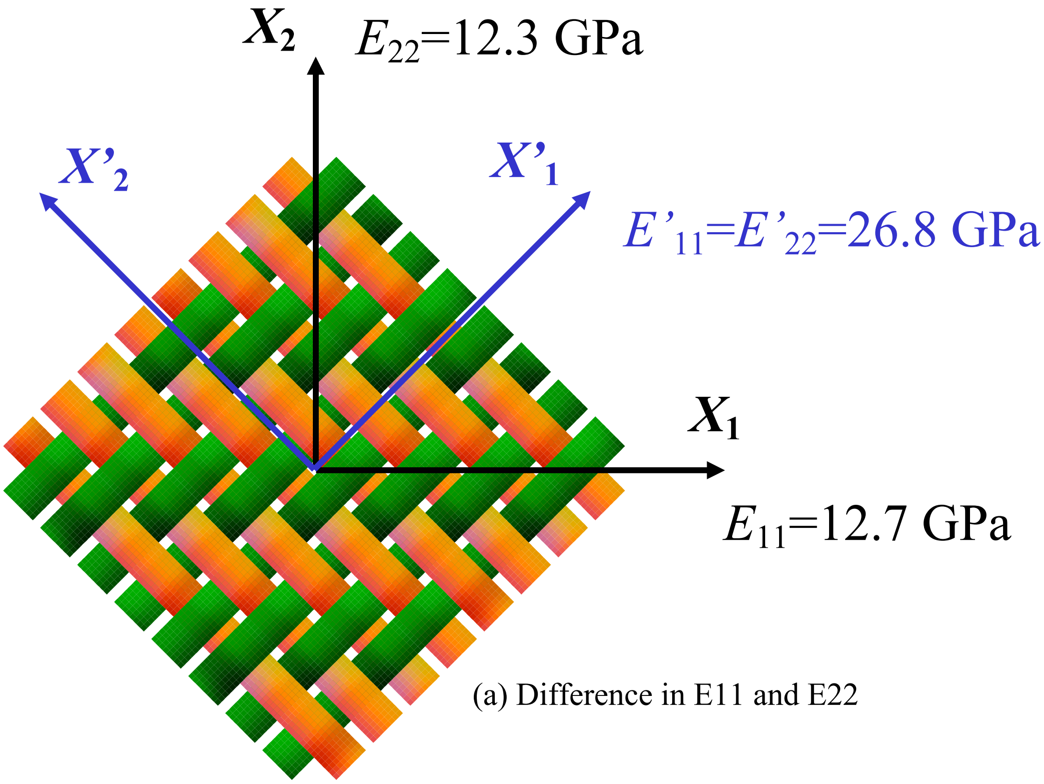

(a) Difference in E11 and E22

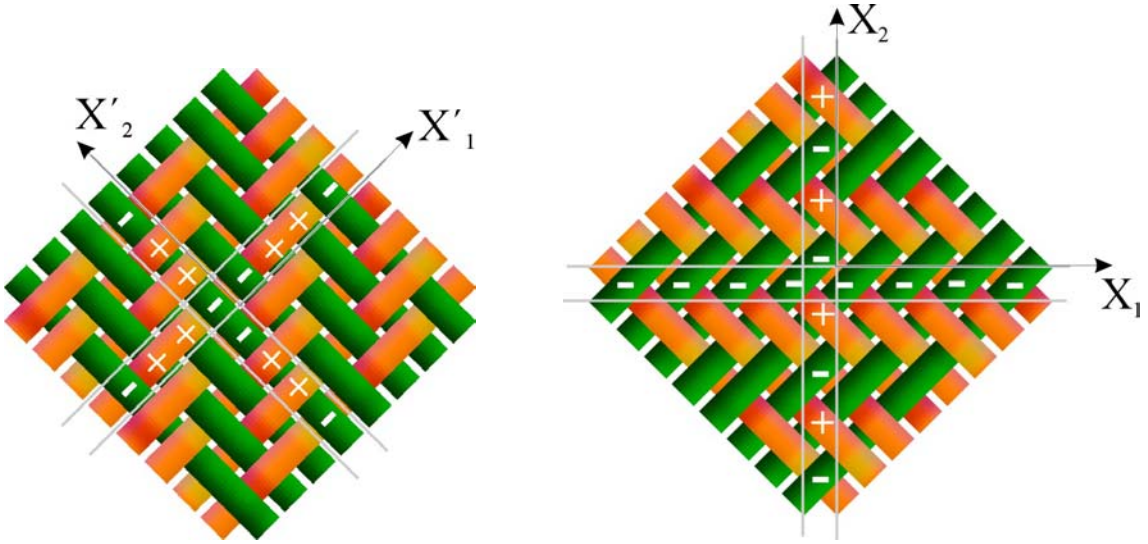

(b) Twill weave has same microstructure in two directions

(c) A 2x2 braid has different microstructure in two directions

Figure 3.7. Difference in properties of complementary braids

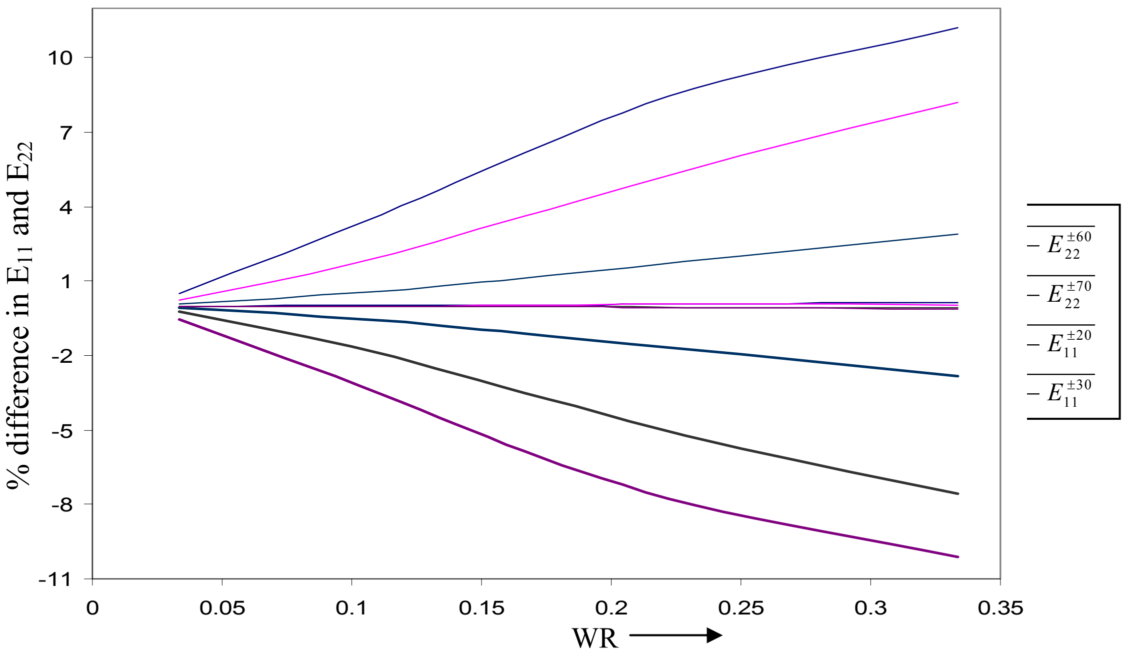

(a) Difference in E_{11} and E_{22}

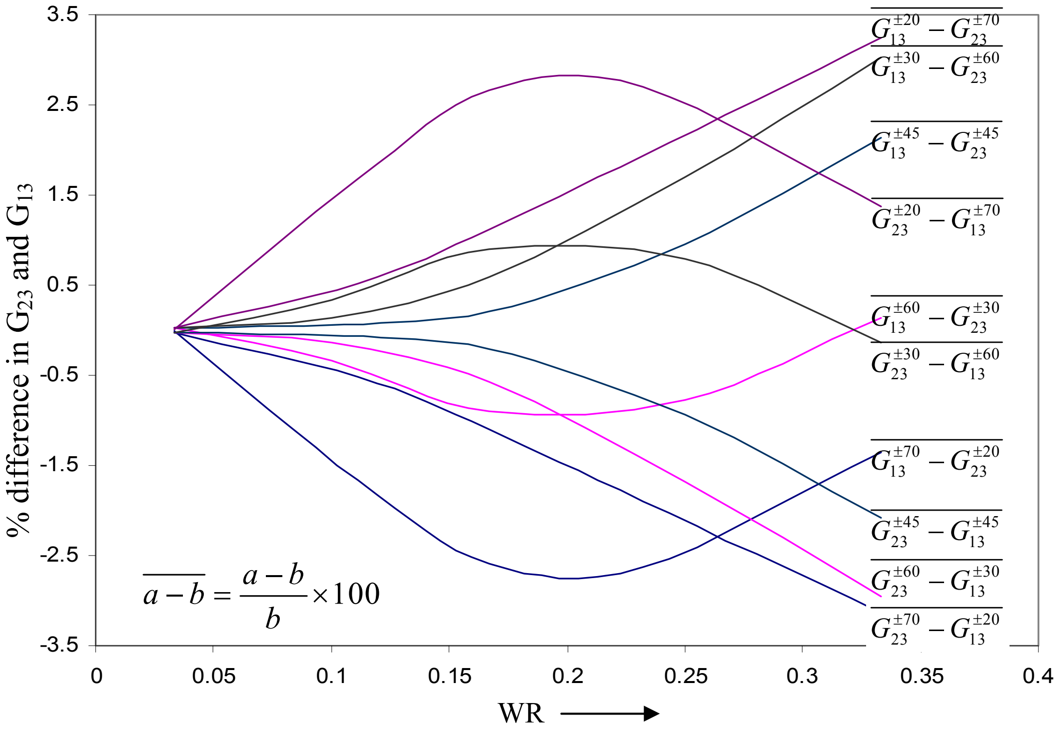

(b) Difference in G_{23} and G_{13}

Figure 3.8. Effect of interlacing on difference in complementary pairs for S2/SC-15

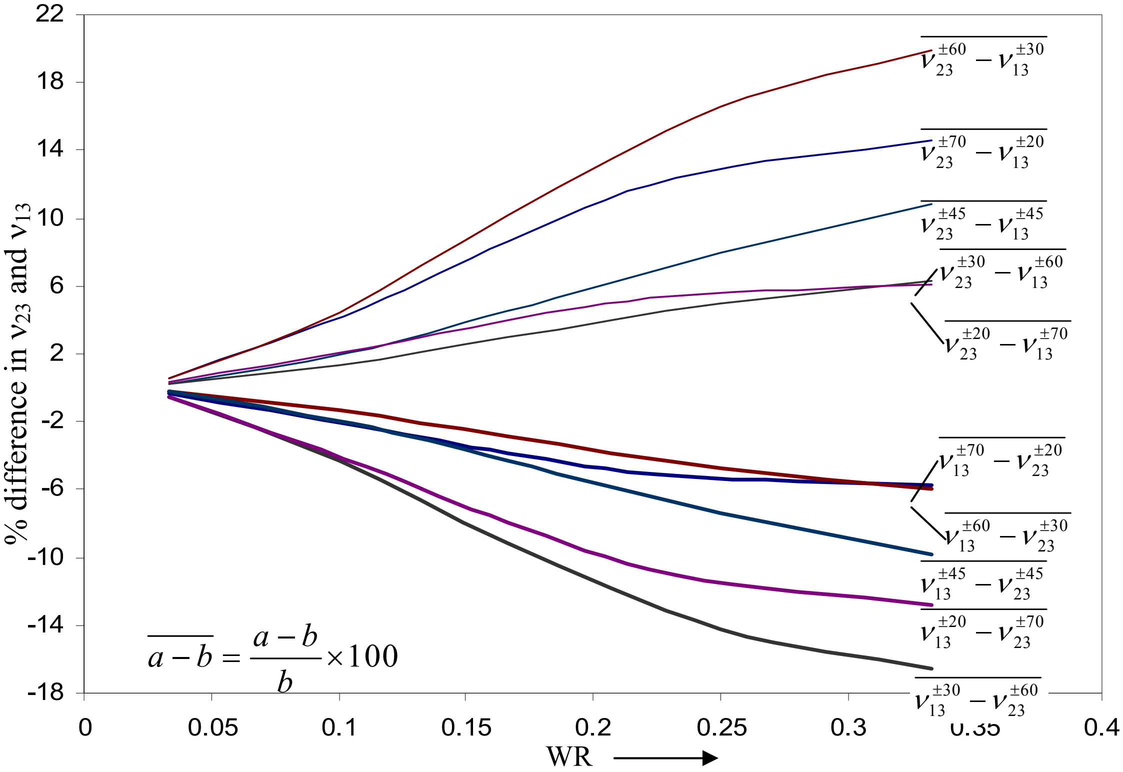

(c) difference in ν_{23} and ν_{13}

Figure 3.8. Continued

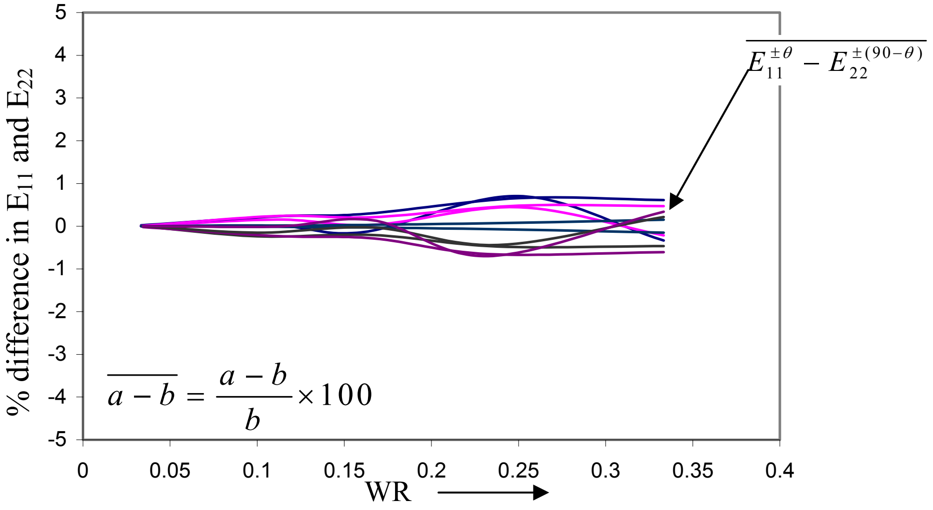

(a) Difference in E_{11} and E_{22}

Figure 3.9. Effect of interlacing on difference in complementary pairs for AS4/411350

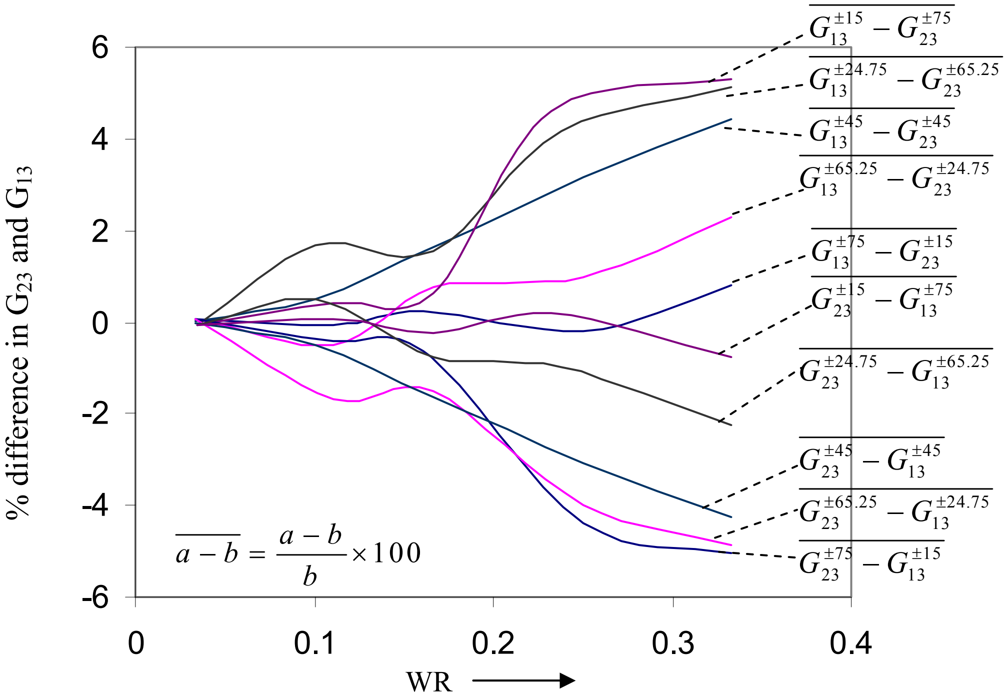

(b) Difference in G_{23} and G_{13}

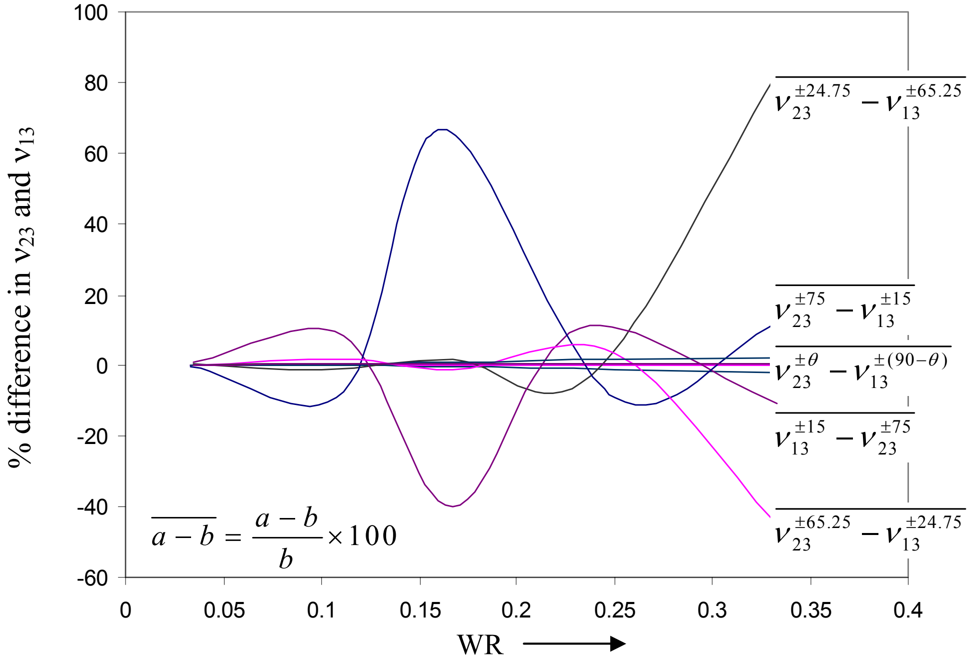

(c) difference in ν_{23} and ν_{13}

Figure 3.9. Continued

$$\text{Percentage difference} = \frac{P_c^{\pm(90-\theta)} - P^{\pm\theta}}{P^{\pm\theta}} \times 100$$

where P is the property for ±θ braid (E_{11}, E_{22}, υ_{23}, υ_{13}, G_{23}, G_{13}) and Pc is the complementary property for ±(90-θ) braid. Variation of the percentage difference is plotted versus waviness ratio for different braid angles. Figure 3.8 shows the effect of unbalance in material architecture on E_{11}, E_{22}, υ_{23}, υ_{13}, G_{23}, G_{13} for S2/SC-15 material system. We see that, as the WR increases, the difference in complementary properties for E_{11}, E_{22}, υ_{23}, υ_{13} increases. But for G_{23}, G_{13}, the difference increases first and then starts decreasing being maximum in the middle range of waviness ratio. For AS4/411-350 material system, the difference is shown in Figure 3.9. The difference in E_{11} and E_{22} is very small for this material system. As the waviness ratio increase, the difference is <1% as is obvious from Figure 3.9 (a). The difference in G_{23} and G_{13} increases with waviness ratio generally. For υ_{23} and υ_{13}, the complementary properties differ considerably only for very large or very small braid angles (for example 15, 24.75, 65.25, 75 here).

A summary of the above results is shown in Figure 3.10. Figure 3.10(a) shows the difference in complementary braids for the full range of WR (0.03~0.33). The larger the band (range from lower to upper difference), the larger is the difference in complementary properties. In general, the glass fiber/epoxy material has a larger range of difference than the carbon fiber/epoxy material for E11 and E22 and carbon/epoxy material system has larger range of difference for v23 and v13. The band is approximately the same for G23 and G13 for the two material systems. The largest difference exists for v23 and v13. For S2/SC-15, the largest difference is ~20% for v13 in the considered range of braid angle (20°-70°) and waviness ratio (0.03~0.33). For AS4/411-350 material, the largest difference is ~82% for v23 in the considered range of braid angle (15°-75°) and waviness ratio (0.03~0.33).

Figure 3.10(b) shows the difference for the reduced waviness range (0.03~0.11). As expected, when the range of waviness is reduced, the difference bands (range from

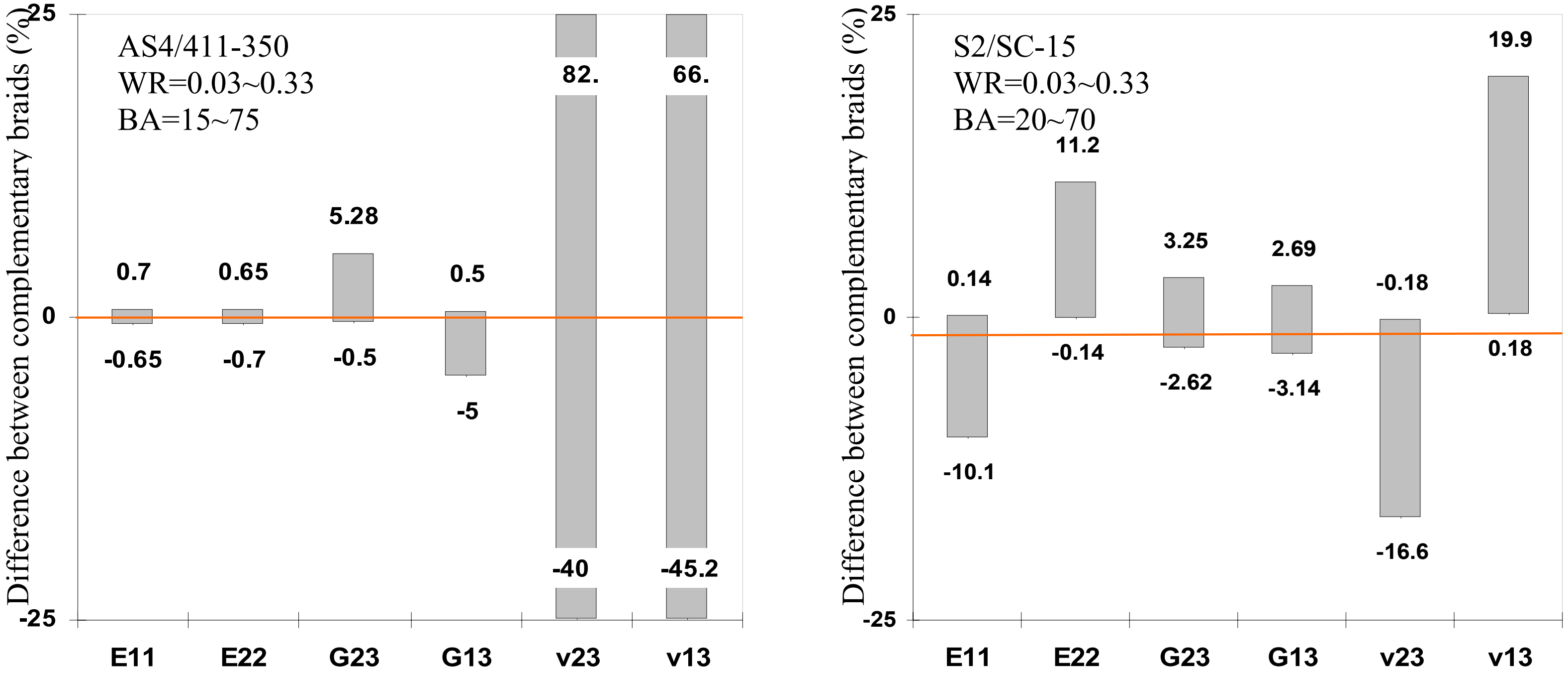

(a) Full range of waviness ratio

Figure 3.10. Percentage difference between complementary braids

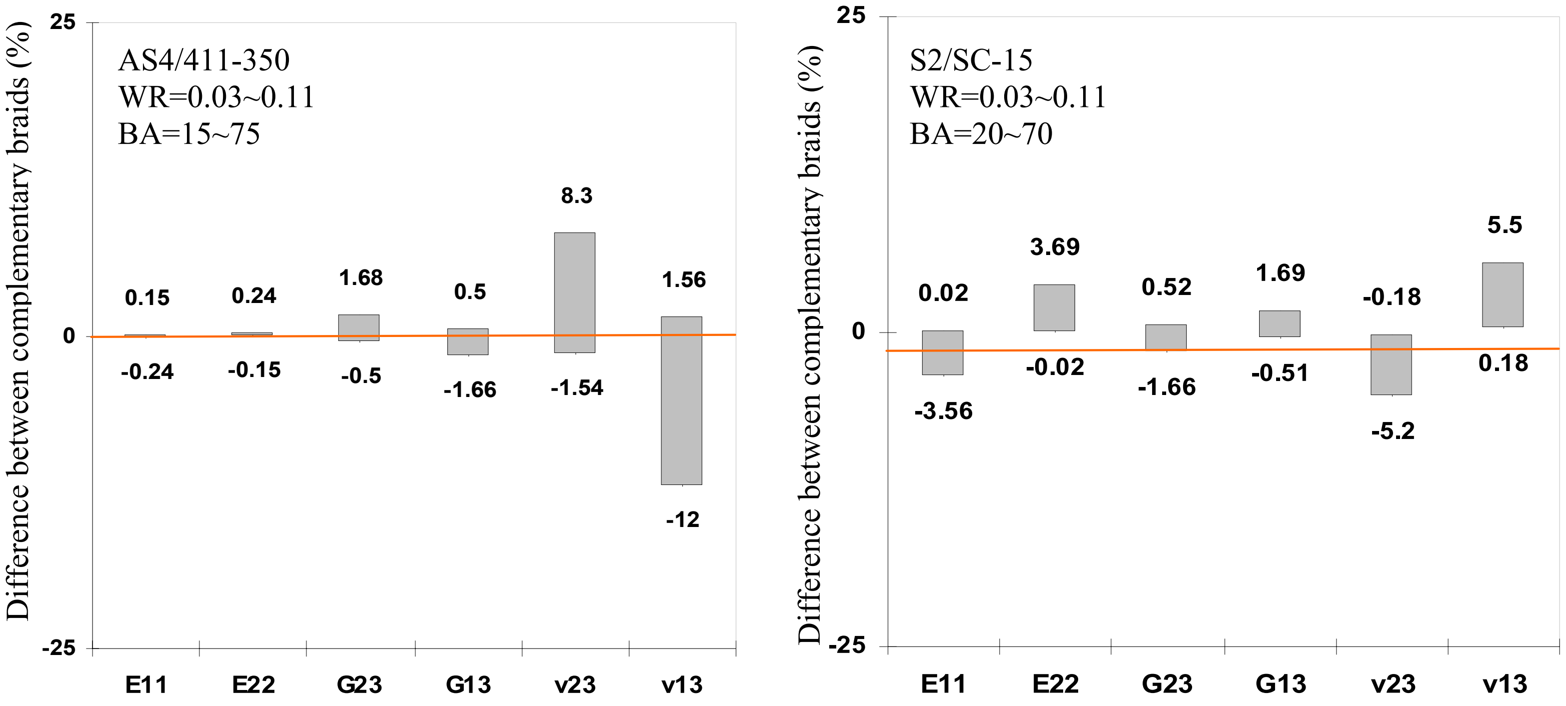

(b) Smaller range of waviness ratio

Figure 3.10. Continued

lower to upper difference) also shrink as compared to Figure 3.10(a). The E11, E22, G23 and G13 have the largest difference <4%, which is very small. For the S2/SC-15 glass fiber/ epoxy, the difference for v23 and v13 is <6% while for the AS4/411-350 carbon fiber/epoxy material system, the difference in these two properties can still be as high as 12%.

The purpose of the discussion is to see which material architecture would provide us the best material properties. For example, both E11 and E22 of a ±θ braid are higher than those of a ±(90-θ) braid, where θ is greater than 45° for the S2/SC-15 glass fiber/ epoxy. Although the difference is considerably high only for high waviness ratio, yet given a choice, it might be advantageous to use braided materials having braid angles ±θ rather than ±(90-θ), where θ is greater than 45° to get higher values of both E11 and E22 for this particular material system. However, there is not much difference between E11 and E22 of AS4/411-350 material system. So one has to check the property difference for a particular material system and an intelligent selection can be made. However, the manufacturing difficulty for large braid angles might impose a constraint on getting this kind of advantage.

3.5 Effect of stacking sequence

Two stacking sequences were shown in Figure 2.15. Exhaustive parametric studies were conducted for symmetric stacking of the tows. It was decided to do spot checking for the effective properties if tows were simply stacked and see if the results differ from symmetric stacking or not. All the analysis was not redone for simple stacking and only the spot-checking was done to save time and avoid large amount of data management. The results produced by simple stacking do not differ much from those of symmetric stacking for S2/SC-15 glass/epoxy material system and hence exhaustive parametric studies were not needed. For the AS4/411-350 material system, the results differ. Some of the results with percentage difference are tabulated below to see how much difference between symmetric and simple stacking exists.

Table 3.2. Effect of stacking sequence for AS4/411-350 material system (WR=1/3)

	±15° braid			±75° braid		
	Stacking sequence			Stacking sequence		
Property	Symmetric	Simple	% difference	Symmetric	Simple	% difference
E11 (GPa)	98.1	94.4	3.9	7.93	7.92	0.12
υ12	0.926	0.905	2.3	0.07	0.07	~0
υ13	0.212	0.192	10.4	0.362	0.364	-0.55
E22 (GPa)	7.88	7.87	0.13	97.8	95.4	2.5
υ23	0.363	0.364	-0.27	0.238	0.226	5.3

We see that the percentage difference between the predictions of symmetric sequence and simple stacking is less than 4% for modulus and can be as high as 10% for Poisson's ratio.

3.6 Comparison of predictions with experimental data

A comparison was made with some of the preliminary experimental results in [53]. The experimental results are listed in Table 3.3. The specimens were tested for various properties. The braid angle of each specimen varies within ±1° of 25°. The average braid angle is ±25.17°. Hence the braid angle used for finite element results was ±25.17°. The only modulus and Poisson's ratio available for comparison are E11 and ν12, respectively. The finite element results are listed in Table 3.4 along with experimental values for comparison. It can be seen that the predicted value of E11 falls within the range of experimental results whereas in-plane Poisson's ratio is a little bit on the high side.

Table 3.3. Experimental results

Specimen	1	2	3
Area, mm^2 (in^2)	129.03(0.20)	123.95(0.191)	128.06(0.197)
Failure Load, KN (Kips)	88.25(19.84)	75.55(16.99)	81.78(18.39)
Ultimate Tensile Strength, MPa (Ksi)	683.31(99.11)	612.52(88.84)	638.59(92.62)
% Elongation at Failure	1.108	0.997	1.160
Modulus, GPa (Msi)	71.33(10.35)	68.52(9.94)	63.71(9.24)
Poisson's Ratio	1.22	1.17	1.16
Braid Angle	24.52	25.05	25.95

Table 3.4. Comparison with finite element results

	FEM Prediction	Experiment		
		Specimen 1	Specimen 2	Specimen 3
E_{11} (GPa)	64.67	71.33	68.52	63.71
E_{22} (GPa)	8.69	-	-	-
E_{33} (GPa)	8.26	-	-	-
G_{12} (GPa)	21.82	-	-	-
G_{23} (GPa)	2.75	-	-	-
G_{13} (GPa)	3.55	-	-	-
ν_{12}	1.532	1.22	1.17	1.16
ν_{23}	0.313	-	-	-
ν_{13}	-0.226	-	-	-

3.7 Stress distribution

The knowledge of the stress state that exists in both tows and in the matrix is imperative for predicting potential damage initiation locations. Although the moduli predictions are simple, the prediction of stress state is difficult as a full three dimensional stress state exists in matrix as well as in tows even for a simple uniaxial loading case. Hence the stress analysis tends to be complex. The cause of this complexity is the complex architecture of braids. The tows are undulated about each other and they interact with adjacent tows. Due to the presence of $+\theta$, $-\theta$ tows, and matrix pockets the architecture is inhomogeneous. As discussed earlier, the moduli can be predicted to a good degree of accuracy using simple theories like laminate plate theory, but the stress state can not be predicted using simple theories. When we apply simple loading like $<\sigma_{xx}>$, a full three dimensional stress state will exist in both matrix and tows, but laminate analysis will predict the presence of only in-plane stresses. Out-of-plane stresses may play a significant role in failure. The characteristic stress distributions will be discussed here. Only preliminary results will be presented here and the future studies will be performed to predict damage under both static and fatigue loading.

Since simple loading produces all the six components of the stress both in matrix and tows, only in-plane extension along the longitudinal axis of the braid will be considered. Some stress contours will be shown in both the tows as well as in matrix. It is impossible to show the stress contour plots for all the stress components at all locations. Moreover the stress contours do not give information about the state of stress inside the upper layer of tow or matrix. One has to slice the tow or matrix to see the interior, which increases the number of stress contours even more. Hence the results will be discussed using several types of techniques like:

- Stress contours
- Location and magnitude of peaks
- Volume distribution curves

Figure 3.11 shows all six components of stress for the loading case $<\sigma_{xx}>$ for S2/SC-15 material system with braid angle ±24.74° and waviness ratio = 1/3. The applied stress is unity. All the components are normalized by the applied stress. It clearly shows that all the components exist even for simple loading. The location and value of stress concentrations vary for each stress component. For example, the peak stress for σ_{11} is tensile and its value 3.13 and it lies near the edge of the tow in the undulating region. The peak stress for σ_{22} is compressive and its value is 0.41 and it lies in the center of the tow in the undulating region. Similarly other stress components have their respective values and locations. The damage initiation will be governed by the values of tensile, compressive and shear strengths of the lamina. So, even a lower value of a particular stress component as compared to the other components may play a significant role in the damage mechanism.

Figure 3.12 illustrates the stress distributions in both matrix and $\pm\theta$ tows. In Figure 3.12 (a) the contours are shown for S2/SC-15 material system with braid angle ±24.74° and waviness ratio = 1/3 and Figure 3.12 (b) corresponds to AS4/411-350 material system with braid angle ±24.74° and waviness ratio = 1/3. The contours are shown only for the σ_{33} stress component. The figures show that the distribution is complex not only in tows, but in matrix also. The straight regions of the tow also have stress gradients. It should be emphasized at this point that a simple analysis like one with laminate plate theory will show σ_{33} to be equal to zero both in the matrix and the tows, which is obviously not the case here. It can be seen from Figure 3.12 that peak stresses are located in the matrix. Hence, the damage might initiate in matrix. It is clear at this point that the stress distribution is quite complex in braids. Even after obtaining the detailed stress distribution data, its interpretation also offers a major challenge.

Figure 3.13 shows the variation of σ_{33} stress contours with change in braid angle for the S2/SC-15 material system. The contours are shown for $+\theta$ tow for all the cases. The contours are normalized by the applied stress $<\sigma_{xx}>$ in all the braids. It can be seen that the location of σ_{33} concentrations change from tension to compression as we go from smaller braid angle (±20°) to larger braid angle (±70°). Moreover the peaks change location from the center of the tow to the edge of the tow with increase in braid angle. So it can be expected that in ±20° braid tow the failure will be due to tensile stress and will initiate at the center of the tow and in ±70° braid tow the failure will be due compressive stress with initiation location at the edge of the tow if at all failure occurs due to σ_{33}. One problem with this kind of prediction is that the magnitudes of peak stresses are sensitive to mesh refinement. And moreover the peak stresses occur only in tiny regions. Then the question arises whether these peak stresses in tiny regions can cause failure since we have already homogenized the fiber and matrix properties. To overcome this problem, the stress data is represented in the form of volume distribution curves. The volume distribution curves tell how much volume of the tow has stresses that exceed a particular value, thereby giving a quantitative measure of the localization of the stress concentrations.

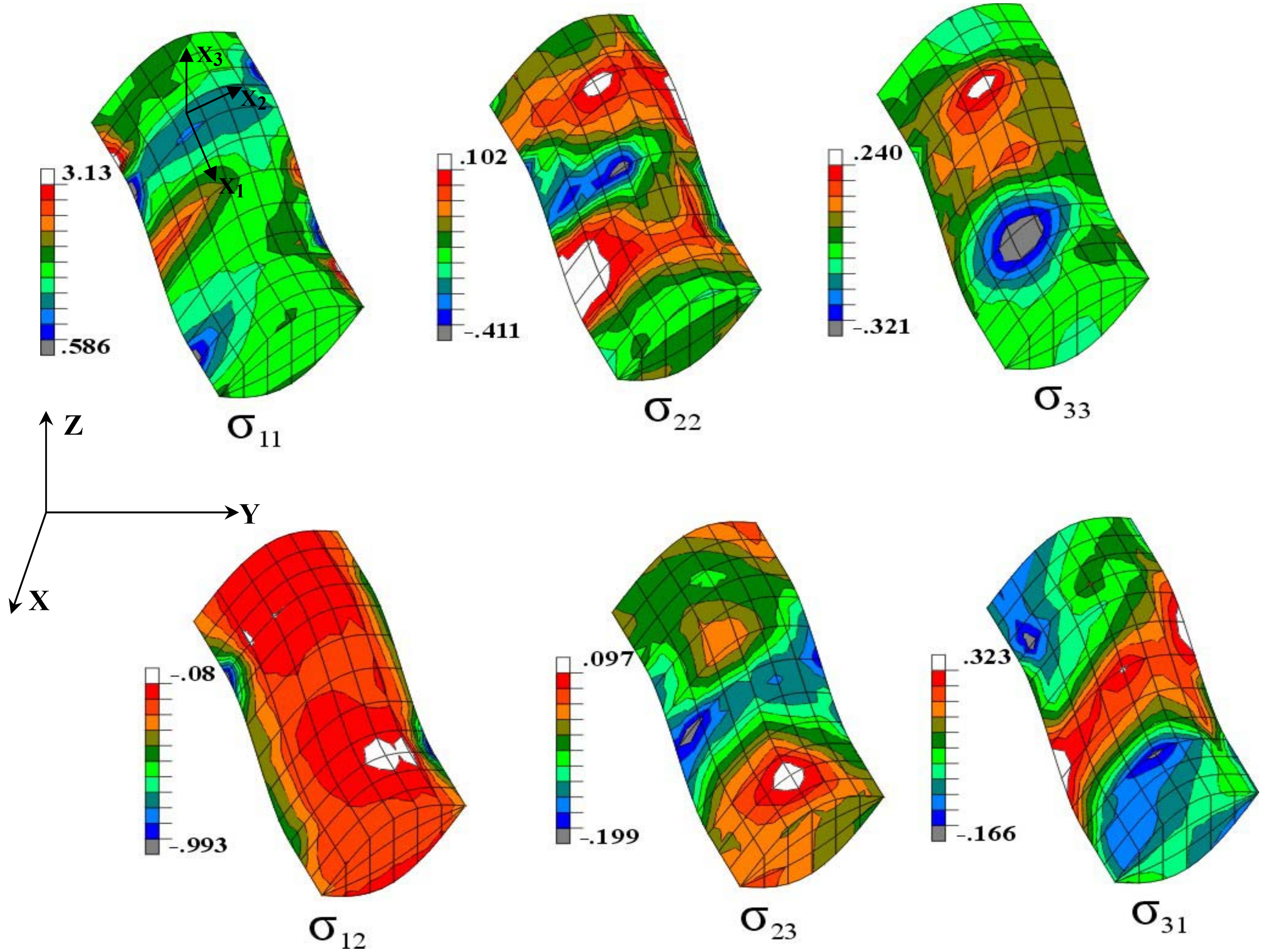

Figure 3.11. Uniaxial loading ($< \sigma_{xx} > = 1$) of ±24.75º braid (S2/SC-15) (WR=1/3)

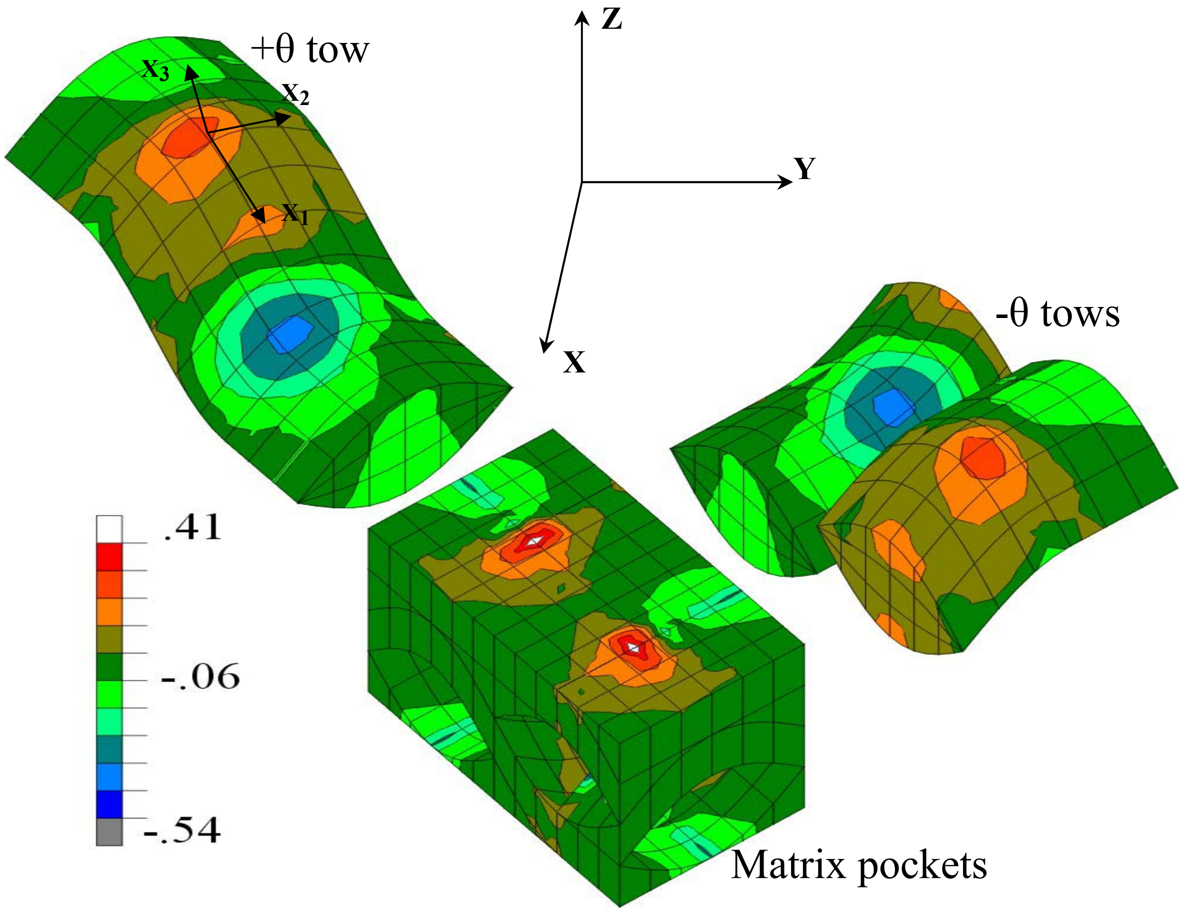

(a) S2/SC-15 material system

Figure 3.12. Normalized stress contours for σ_{33} (uni-axial loading ($< \sigma_{xx} > = 1$) of ±24.75º braid with WR=1/3)

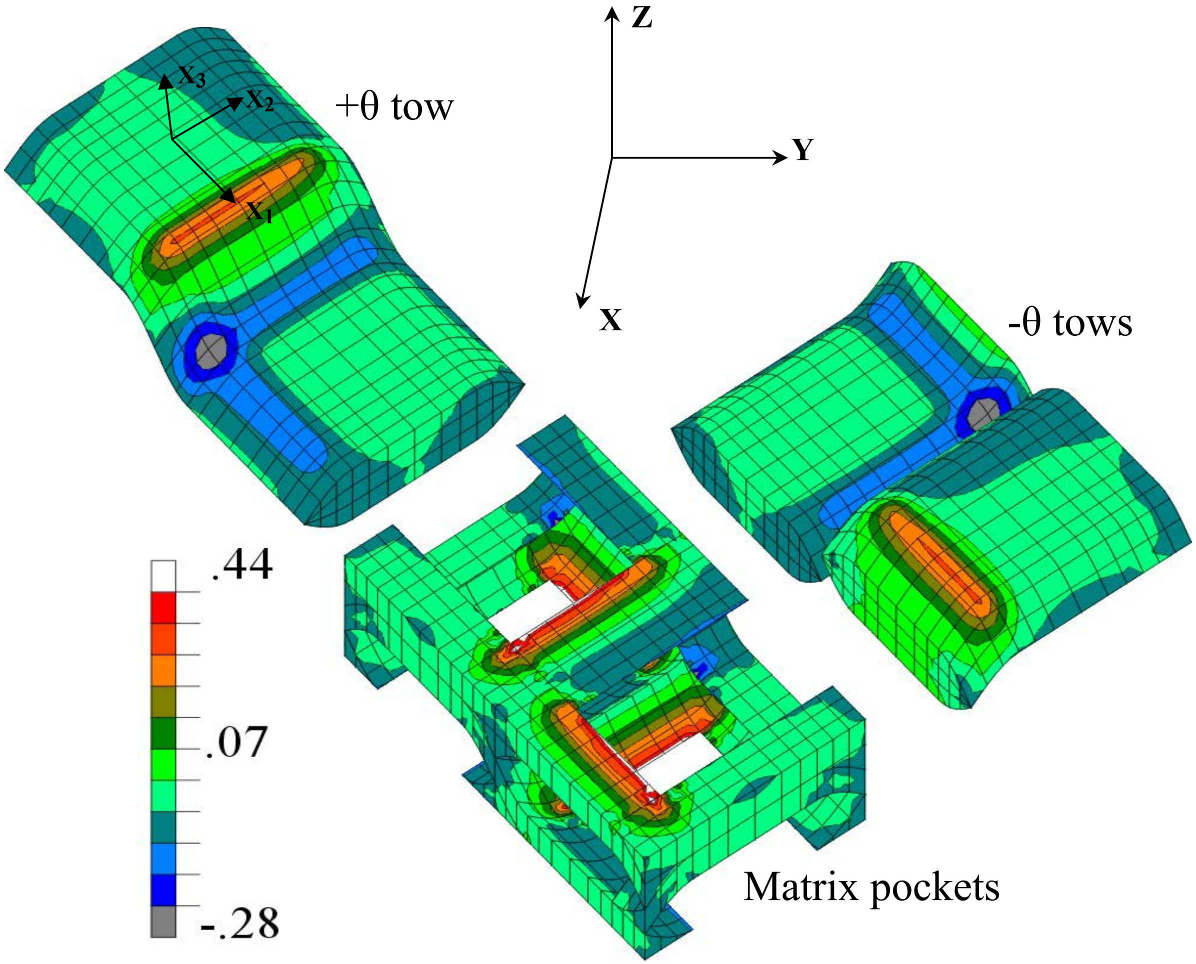

(b) AS4/411-350 material system

Figure 3.12. Continued

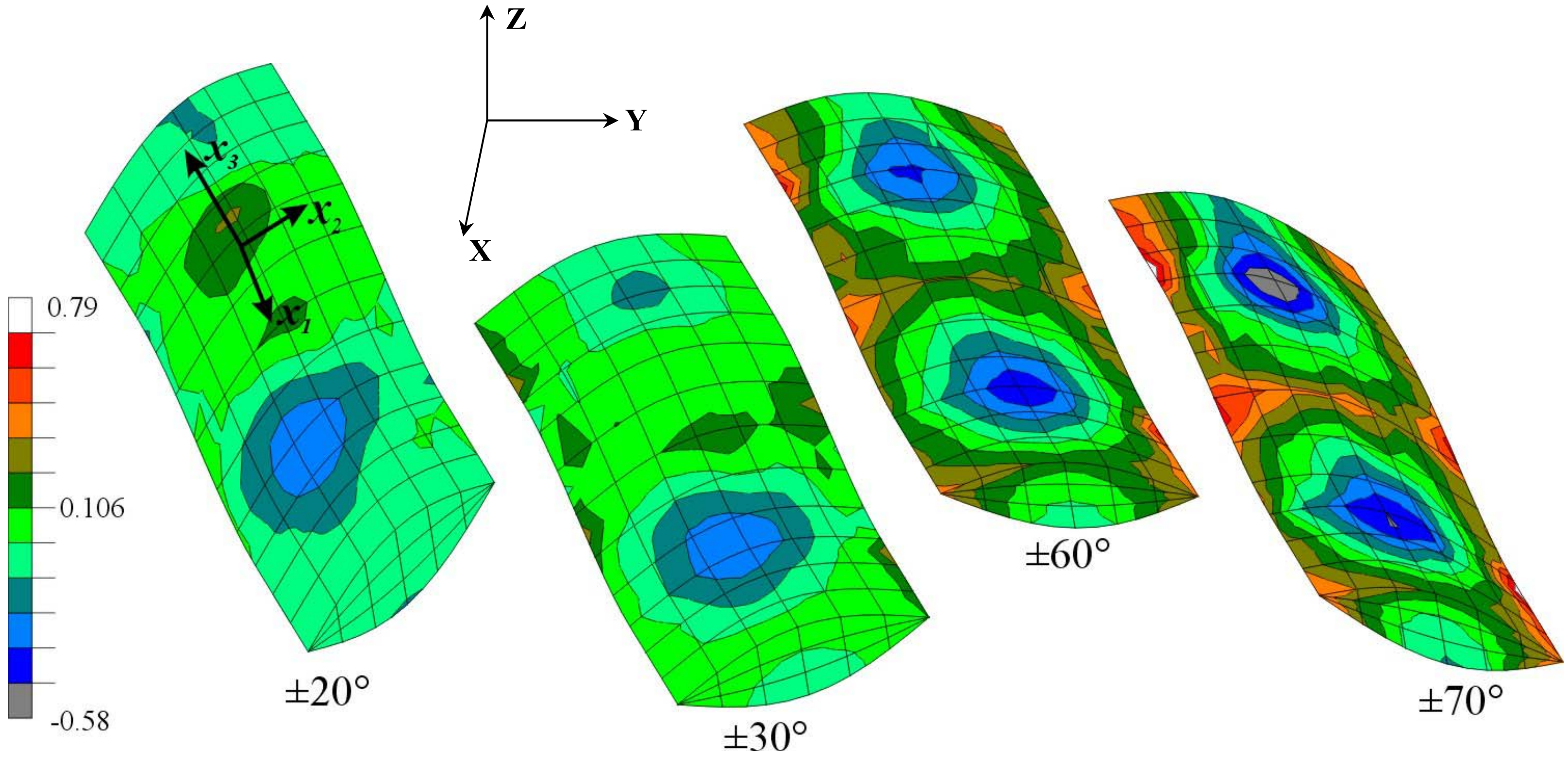

Figure 3.13. Effect of braid angle on σ_{33} stress concentration.

Uniaxial loading ($< \sigma_{xx} > = 1$) of S2/SC-15 (WR=1/3)

Figure 3.14 shows the volume distribution graphs in the +θ tow for the σ22 stress component when the applied load is <σxx> = 329 MPa for all the braids. By imposing the same applied stress the volume averaged strain $<\varepsilon_{xx}>$ is different for different braids. The volume distributions are plotted for different braids. Along with different braids the volume distribution plots are also shown for equivalent laminate models. Dotted lines show laminate results. The ±20° braid has both compressive as well as tensile stresses in the tow whereas ±45° and ±70° braid have only tensile stresses in the tow. It can be seen that a ±20° braid has compressive stresses in more than 95% of the volume whereas ±45° and ±70° braid have only tensile stresses in the entire volume of the tow. It can also be seen that the stress state predicted by 3D braid analysis differs considerably from laminate analysis as approximately 30% of the volume in ±45° and ±70° braid has larger stresses than the laminate values. Figure 3.15 shows a similar plot for the σ_{31} stress component. It can be seen that for ±20° braid, more than 30% of the volume has shear stresses σ_{31} more than 40MPa, whereas the volume having shear stress σ_{31} > 40MPa is negligibly small for ±45° and ±70° braid. Further, the laminate analysis predicts zero value of σ_{31} stress whereas braid analysis showed a wide variation.

It was seen that the stress state in braids is quite complex and all the six components of stress exist even for simple loading cases. Stress contour plots give a good visualization but they do not give complete quantitative information about the stresses as in many cases a tiny fraction of the tow has stresses near the peak values. It needs further study to see whether such tiny localized fractions are significant or not. Volume distribution plots are another way to have a quantitative measure of the stresses. Experimental data about the damage initiation loads and locations would be helpful to asses the accuracy of the predictions.

All the parametric studies were done using an inexpensive personal computer. The maximum runtimes for one particular case are listed below for two computers: one having a Pentium II 400 MHz CPU and one with a Pentium IV 2.4 GHz CPU. It can be seen that equation solving time for a typical case is less than 2 minutes with 2.4 GHz PC and is approximately six times less than that with a 400 MHz PC.

Table 3.5. Runtimes on a personal computer for one case

	Pentium II 400 MHz CPU		Pentium IV 2400 MHz CPU	
Material system	S2/SC-15	AS4/411-350	S2/SC-15	AS4/411-350
Mesh generation time	21 sec	01 min, 06 sec	07 sec	14 sec
Equation solving time	02 min, 45 sec	11 min, 31 sec	28 sec	01 min, 56 sec

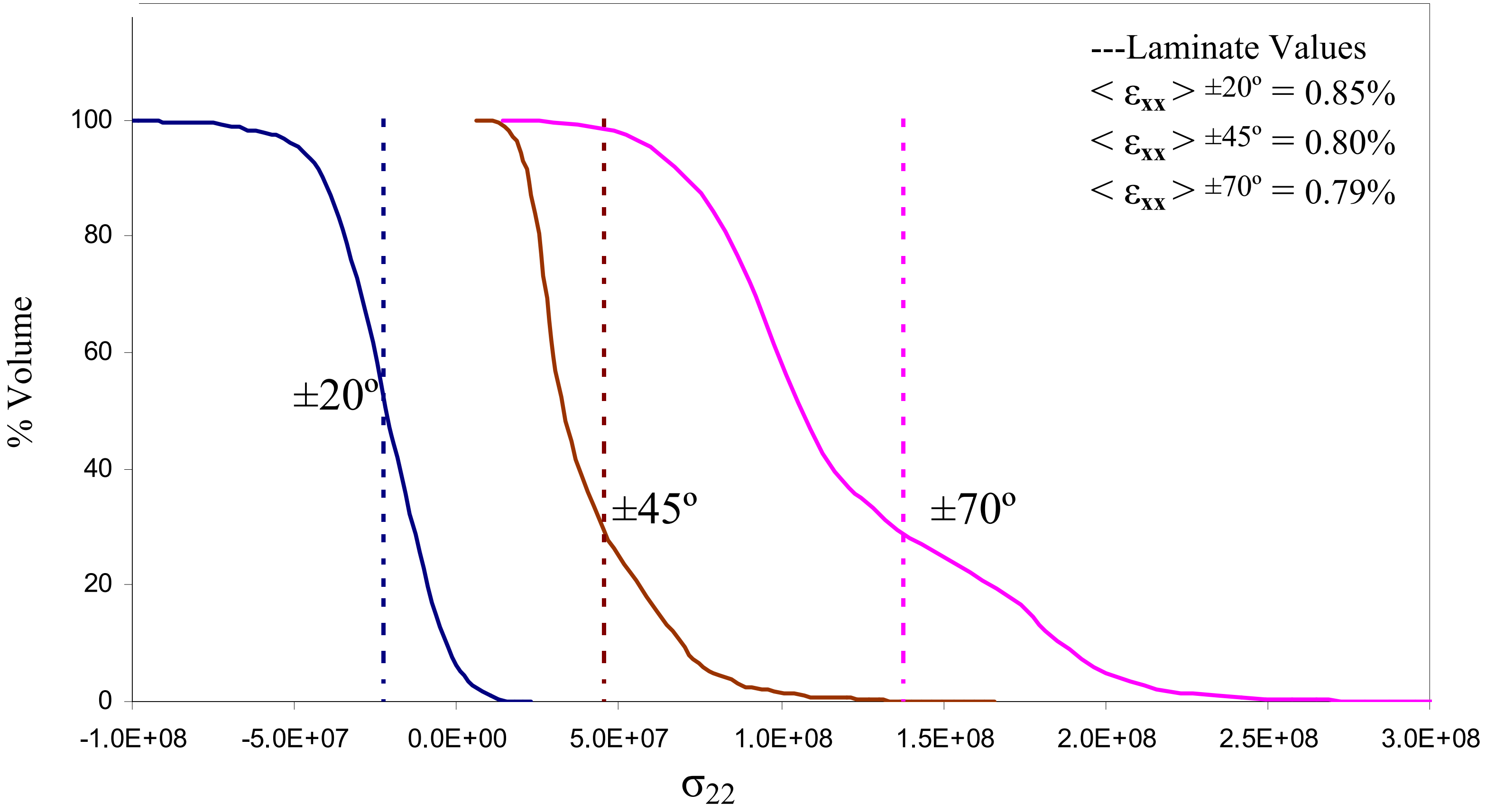

Figure 3.14. σ_{22} volume distribution in tow of different braids (WR=1/3).

Uniaxial loading ($< \sigma_{xx} >$ = 3.29E+08 for all braids) (S2/SC-15)

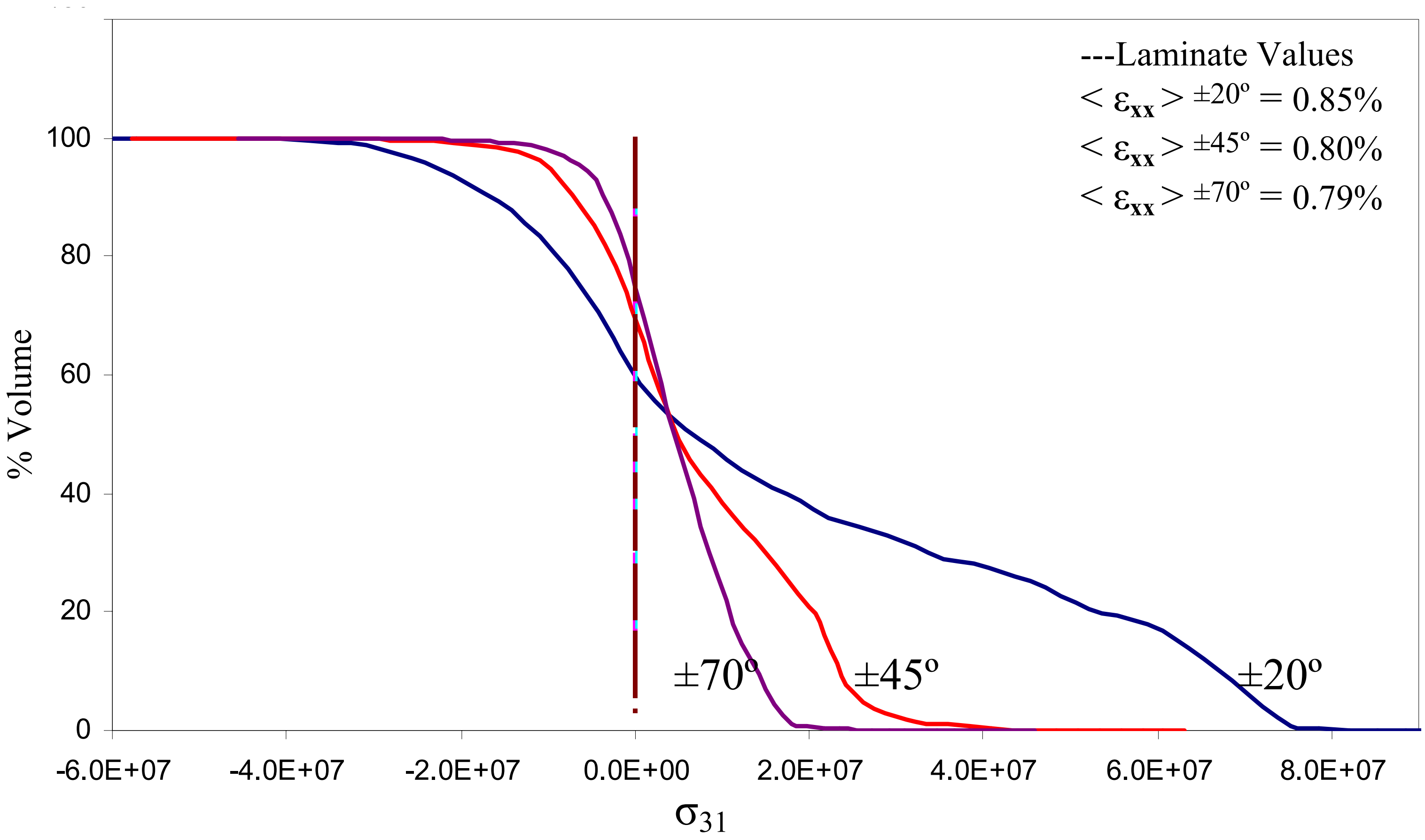

Figure 3.15. σ_{31} volume distribution in tow of different braids (WR=1/3).

Uniaxial loading ($< \sigma_{xx} > = 3.29E+08$ for all braids) (S2/SC-15)

3.8 Summary

Parametric studies were performed to see the effect of various parameters on the effective engineering properties of the 2x2 braids. First of all the effect of waviness ratio and braid angle was studied for two material systems: S2/SC-15 and AS4/411-350. Three-dimensional effective properties were obtained for two typical material systems using finite element based micromechanics. The properties were also predicted for an equivalent laminate configuration using three-dimensional finite element analysis. The purpose was two-fold: 1) Filter out the orientation effect of the tows (in +θ and –θ direction) by normalizing with laminate values so that exclusive effect of braid architecture and waviness ratio could be observed. 2) To compare the results of finite element analysis of braids with laminate results to see how much difference it makes if one uses simple analyses like laminate theory to predict properties of the braids. The results were presented and examined in terms of sensitivity of the properties to the change of braid angle and waviness ratio and the deviation of the proprieties from the value predicted by laminate theory.

The properties of complementary braids differ from each other due to unbalance in material architecture that exists in braids. The properties of the complementary braids were compared to see which material architecture would provide us the best material properties.

The effect of stacking sequence (simple and symmetric) was determined for braids. It was seen that for both the material systems the difference between the effective engineering properties of the simple stacking and symmetric stacking of mats was very small.

A full three-dimensional stress state exists in both the tows and matrix in the braids even for very simple loading. The stress analysis is complex due to the tow undulation. The stress distributions were predicted to find the location and value of peak stresses. The effect of braid angle on the location and magnitude of braids was determined.

4. CONCLUSIONS AND FUTURE WORK

4.1 Conclusions

In this chapter, the conclusions of the modeling for 2x2 braids and the results of parametric studies are presented. Finally, the scope for further research is discussed.

4.1.1 Modeling of 2x2 braids

The twill weave and the 2x2 braids have some similarities. As a matter of fact, away from boundaries, the twill looks exactly the same as the 2x2 braid when the braid angle is ±45°. The tows in the twill weave are always orthogonal whereas they are not in the case of the 2x2 braided (except for ±45° braid). Direct model generation for 2x2 braids is difficult. A mapping technique was developed to exploit the similarities that exist between the twill and the braid to generate models of the 2x2 braid from the previously developed [3] models of the twill. The tow cross-section of the 2x2 braid varies unusually and does not remain constant as we move along the braided tow. Although the cross-section shapes vary, but the cross-sectional area remains constant therefore there is not a concern about "*disappearing*" volume of the material. Periodicity that exists in the braid microstructure can be exploited to find the boundary conditions for the full unit cell. The analysis region can be further decreased by utilizing the symmetries that exist within a unit cell. The symmetry operations of mirroring and rotation were used to decrease the analysis region to one-fourth of the unit-cell for the symmetric stacking of the mats and to one-half for the simple stacking of the mats. The boundary conditions are not intuitively obvious and involve numerous multipoint constraint relationships for different faces of the analysis region.

4.1.2 Effective properties

All the effective properties of the 2x2 braids were obtained using the three-dimensional finite element analysis. The analysis showed that the material was orthotropic. The effect of different parameters like waviness ratio, braid angle and stacking sequence on effective properties was studied for two material systems: S2/SC-15 and AS4/411-350. An equivalent laminate configuration was used to filter out the effects of the braid angle that can be predicted by laminate theory. The effective properties were normalized by the respective properties of the reference laminate. The results were presented and examined in terms of sensitivity of the properties to the change of braid angle and waviness ratio and the deviation of the proprieties from the value predicted by laminate theory.

It was found that the in-plane properties of AS4/411-350 material systems were not very sensitive to the change of braid angle and waviness ratio whereas those of S2/SC-15 were more sensitive. The transverse properties (G_{13}, G_{23}, ν_{13} and ν_{23}) were found to be fairly sensitive to the change of braid angle and waviness for both material systems. The out-of-plane modulus E_{33} is almost insensitive to the change of the braid angle and waviness ratio because the through–thickness behavior of the 2x2 biaxial braid is mainly dominated by the matrix properties. It was seen that all the effective properties of the S2/SC-15 material system were considerably more sensitive than those of AS4/411-350 material system. So it can be concluded that the sensitivity to changes in waviness ratio and braid angle is affected by the material system.

In the realistic range of waviness ratio (0.03 to 0.11), which is more representative of most structural 2D braids, the sensitivity of the effective properties drops significantly. In particular, the in-plane properties of carbon fiber/epoxy (AS4/411-350) can be predicted very well by simple laminate model. However, for the glass fiber/epoxy (S2/SC-15), the laminate simplification can produce as large as 16% error for the in-plane properties of the 2x2 biaxial braids.

The most sensitive effective properties were found to be the transverse properties (G_{13}, G_{23}, ν_{13} and ν_{23}). This suggests that the simple laminate theory cannot be used to get reasonable approximation for the transverse properties of the braid. On the other hand, it shows that the G_{13} and G_{23} are more than 29% larger than the laminate value for both material systems considered, which means 29% increase in transverse shear modulus can be achieved using the 2x2 biaxial braid as compared to the equivalent angle-ply laminate. This can be significant for structural applications in which higher G_{13} and G_{23} are desirable.

The properties of complementary braids differ from each other due to unbalance in material architecture that exists in braids. The difference between the complementary properties was found for both the material systems and it was seen that the maximum difference in modulus is ~11% for the full range of waviness ratio. For the realistic range of waviness ratio, the difference between complementary moduli is negligibly small. The E11, E22, G23 and G13 have largest differences <4%, which is very small for both the material systems. For the glass fiber/ epoxy, the difference for v23 and v13 is <6% while for the AS4/411-350 carbon fiber/epoxy material system, the difference in these two properties can still be as high as 12%.

For the 2x2 braid, two stacking sequences were considered: Simple stacking and symmetric stacking. The effect of stacking sequence on the effective properties was found. It was observed that the difference between effective properties of the simple stacking and symmetric stacking for S2/SC-15 glass/epoxy material system was negligibly small. For the AS4/411-350 material system, the results do differ, and the difference can go as high as ~10%.

4.1.3 Stress distribution

For braids, a full three-dimensional stress states exists in both the tows and in the matrix even for simple uniaxial loading, thereby making their stress analysis to be complex. The cause of this complexity is the complex architecture of braids. These stress states cannot be predicted using simple analysis like laminate theory.

The location and value of stress concentrations vary for each stress component. For example, for uniaxial loading ($< \sigma_{\mathbf{xx}} > = 1$) of ±24.75º braid for S2/SC-15 material system with WR=1/3, the normalized σ11 peak stress in the tow is tensile and its value 3.13 and it lies near the edge of the tow in the undulating region. The peak stress for σ22 is compressive and its value is 0.41 and it lies in the center of the tow in the undulating region.

The effect of braid angle on stress peaks was studied and it was seen that the braid angle changes not only the location of peaks but can reverse their sign (e.g. tension to compressive) also.

4.2 Future work

The microstructure of 2x2 braids has been well understood in this work and effective engineering properties were predicted. The prediction of stress distributions in braids lays the foundation for damage predictions. The following studies can further be performed based on the present work:

1. Develop simple formulas to be able to use classical laminate theory for predicting the effective engineering properties of the braids.
2. Progressive failure analysis of the braids remains to be performed.
3. Initiation and growth of damage under fatigue.
4. To generate two important curves to characterize the tension-tension fatigue behavior of braided composites
    1. Stress-fatigue life (S/S_u-N_f) diagram.
    2. Stiffness degradation over the entire fatigue life of the specimens

REFERENCES

1. Mouritz, A. P., M. K. Bannister, P. J. Falzon and K. H. Leong. 1999. "Review of applications for advanced three-dimensional fiber textile composites," *Composites: Part A: Applied Science and Manufacturing,* 30: 1445-1461.

2. Whitcomb, J. D. and J. Noh. 1999. "Routine three -dimensional analysis of woven composites," presented at the *12th International Conference of Composite Materials* (ICCM-12), Paris, France, July 1999.

3. Tang, X. December 2001. "Micromechanics of 2D woven composites," Ph.D. Dissertation, Department of Aerospace Engineering, Texas A&M University, College Station, TX.

4. Byun, J.-H. 2000. "The analytical characterization of 2-D braided textile composites," *Composites Science and Technology*, 60: 705-716.

5. Wu, W. L., M. Kotaki, A. Fujita, H. Hamada, M. Inoda, and Z. I. Maekawa. 1993. "Mechanical properties of warp-knitted, fabric-reinforced composites," *Journal of Reinforced Plastics and Composites*, 12: 1096-1110.

6. Tan, P., L. Tong and G. P. Steven. 1997. "Modelling for predicting the mechanical properties of textile composites - A review," *Composites Part A,* 28A: 903-922.

7. Cox, B. N. and G. Flanagan. 1997. "Handbook of analytical methods for textile composites," NASA CR 4570.

8. Whitcomb, J. D. and A. D. Kelkar. 2002. "Modeling and performance evaluation of braided composites," FAA annual report of Grant No. DTFA03-01-C00033.

9. A&P Technology Inc. 2000. "Frequently asked questions," available at http://www.braider.com [accessed in June 2002].

10. Dexter, B. H. 1998. "Development of textile reinforced composites for aircraft structures," in proceedings of *TexComp 4 conference,* Kyoto, Japan. pp. O-32-1 bis O-32-8.

11. Bystrom, J., N. Jakebsons and J. Varna. 2000. “An evaluation of different models for predictions of elastic properties of woven composites,” *Composites Part B*, 31B: 7-20.

12. Ko, F.K. 1989, “Three dimensional Fabrics for composites,” *Textile Structural Composites: Series 3*, Chou, T.W. and F. K. Ko, Editors, Elsevier Science, New York.

13. Miravete, A. 1999. *3-D textile reinforcements in composite materials.* Woodhead Publishing Limited, Cambridge, England.

14. Ishikawa, T. and T. W. Chou. 1982. "Stiffness and strength behavior of woven fabric composites," *Journal of Material Science*, 17: 3211-3220.

15. Ishikawa, T., M. Matsushima and Y. Hayashi. 1985. "Experimental confirmation of the theory of elastic moduli of fabric composites,” *Journal of Composite Materials*, 19: 443-458.

16. Naik, N. K. and P. S. Shembekar. 1992. "Elastic behavior of woven fabric composites: I - Lamina analysis," *Journal of Composite Materials,* 26: 2196-2225.

17. Naik, N. K. and V. K. Ganesh. 1993. “Prediction of thermal expansion coefficients of plain weave fabric composites”, *Composite Structures*, 26: 139-154.

18. Hahn, H. T. and R. Pandey. 1994. “A micromechanics model for thermoelastic properties of plain weave fabric composites,” *Journal of Engineering Material Technology,* 116: 517-523.

19. Vandeurzen, Ph., J. Inens and I. Verpoest. 1996. “A critical comparison of analytical and numerical (FEM) models for the predictions of the mechanical properties of woven fabric composites,” in proceedings of *TexComp-3 Conference,* Aachen, Germany, pp. 12/1-11.

20. Naik, R. A. 1995. "Failure analysis of woven and braided fabric reinforced composites," *Journal of Composite Materials*, 29: 2334-2363.

21. Paumelle, P., A. Hassim and F. Léné. 1990. “Composites with woven reinforcements: calculation and parametric analysis of the properties of homogeneous equivalent,” *La Recherche Aérospatiale,* 1: 1-12.
22. Paumelle, P., A. Hassim and F. Léné. 1991. “Microstress analysis in woven composite structures,” *La Recherche Aérospatiale,* 6: 47-62.
23. Blackketter, D. M., D. E. Walrath and A. C. Hansen. 1993. "Modeling damage in a plain weave fabric-reinforced composite material," *Journal of Composites Technology & Research*, 15(2): 136-142.
24. Whitcomb, J. D. and X. Tang. 2001. "Effective moduli of woven composite," *Journal of Composite Materials*, 35(23): 2127-2144.
25. Whitcomb, J. D., J. Noh and C. D. Chapman. 1999. "Evaluation of various approximate analyses for plain weave composites," *Journal of Composite Materials*, 33 (21).
26. Whitcomb, J. D. and X. Tang. 1999. "Effect of tow architecture on stresses in woven composites," in *40th AIAA/ ASME/ ASCE/ AHS/ASC Structures, Structural Dynamics and Materials Conference.* AIAA-99-1479 pp.1-10.
27. Whitcomb, J. D. 1991. “Three dimensional stress analysis of plain weave composites,” NASA TM 101672, November 1989. Composite Materials: Fatigue and Fracture, Third Volume, T.K. O'Brien, ed., ASTM STP 1110, pp. 417-438, 1991.
28. Whitcomb, J. D., C. D. Chapman and X. Tang. 2000. “Derivation of boundary conditions for micromechanics analyses of plain and satin weave composites,” *Journal of Composite Materials,* 34(9): 724-747.
29. Tang, X. and J. D. Whitcomb. 2003. “General techniques for exploiting periodicity and symmetries in micromechanics analysis of textile composites,” *Journal of Composite Materials,* in press.

30. Vandurzen, Ph., J. Ivens and I. Verpoest. 1996. "A three-dimensional micromechanical analysis of woven-fabric composites: I. Geometric analysis," *Composites Science and Technology*, 56: 1303-1315.
31. Vandurzen, Ph., J. Ivens and I. Verpoest. 1996. "A three-dimensional micromechanical analysis of woven-fabric composites: I. Elastic analysis," *Composites Science and Technology*, 56:1317-1327.
32. Ma, C. L., J. M. Yang and T. W. Chou. 1986. "Elastic stiffness of three-dimensional braided textile structure composites," in *Composite Materials: Testing and Design (Seventh Conference),* ASTM 893.
33. Yang, J. M., C. L. Ma and T. W. Chou. 1986. "Fiber inclination model of three-dimensional textile structural composites," *Journal of Composite Materials*, 20(5): 472-483.
34. Byun, J.-H., T. J. Whitney, G. W. Du and T. W. Chou. 1991. "Analytical characterization of two-step braided composites," *Journal of Composite Materials*, 25(12): 1599-1618.
35. Naik, R. A., P. G. Ifju, and J. E. Masters. 1994. “Effect of fiber architecture parameters on deformation fields and elastic moduli of 2-D braided composites,” *Journal of Composite Materials*, 28(7): 656-681.
36. Yang, J. M. and T. W. Chou. 1989. "Thermo elastic analysis of triaxial woven fabric composites in textile structural composites,” in *Textile structural Composites: Composite Materials Series 3*, Chou T. W. and Ko F. R. editors, Elsevier Science, Amsterdam, Chapter 8.
37. Masters, J. E., R. L. Foye, C. M. Pastore and Y. A. Gowayed. 1993. “Mechanical properties of triaxially braided composites: experimental and analytical results,” *Journal of Composite Technology,* 15: 112-122.
38. Smith, L. V. and S. R. Swanson. 1993. “Response of braided composites under compressive loading,” *Composite Engineering* 3: 1165-1184.

39. D'Amato, E. 2001. “Finite element modeling of textile composites,” *Composite Structure,* 54: 467-475.

40. Fujita, A., Z. Mackawa, H. Hamada and A. Yokoama. 1992. “Mechanical behavior and fracture mechanism in flat braided composites. Part I: Braided flat bar,” *Journal of Reinforced Plastic Composites,* 11: 600-617.

41. Fujita, A., Z. Mackawa, H. Hamada and A. Yokoama. 1992. “Mechanical behavior and fracture mechanism in flat braided composites. Part 2: Braided flat bar with a circular hole,” *Journal of Reinforced Plastic Composites* 11: 618-632.

42. Fujita, A., Z. Mackawa and H. Hamada. 1993. “Tensile properties of carbon fiber triaxial woven fabric composite,” *Journal of Composite Materials*, 27(15): 1428-1442.

43. Fujita, A., Z. Mackawa, H. Hamada and E. Ohno. 1994. “Mechanical behavior and fracture mechanism in flat braided composites. Part III: Mechanically fastened joint in flat braided bar,” *Journal of Reinforced Plastic Composites* 13: 740-755.

44. Dadkah, M. S., J. G. Flintoff and B. N. Cox. 1995. “Simple models for triaxially braided composites,” *Composites* 26: 561-577.

45. Fedro, M. J. and K. Willden. 1991. “Characterization and manufacturing of braided composites for large commercial aircraft structures,” *NASA CP* 3154: 387-429.

46. Falzon, P. J. and I. Herszberg. 1998. “Mechanical performance of 2-D braided carbon/epoxy composites,” *Composites Science and Technology*, 58: 253-265.

47. Kollegal, M. G. and S. Sridharan. 2000. "Strength prediction of plain woven fabrics," *Journal of Composite Materials*, 34(3): 240-257.

48. Chapman, C. D. 1997. "Prediction of moduli and strength of woven carbon-carbon composites using object-oriented finite element analysis," Ph.D. Dissertation, Department of Aerospace Engineering, Texas A&M University, College Station.

49. Whitcomb, J. D. and X. Tang. 2000. "Predication of progressive failure of woven composites," in *Proceedings of the ASME*, Aerospace Division, AD-Vol. 63: 21-29.

50. Vandurzen, P., J. Ivens and I. Verpoest. 1998. "Micro-stress analysis of woven fabric composites", *Journal of Composites Materials,* 32(7): 623-651.
51. Vandurzen, P., J. Ivens and I. Verpoest. 1997. "TexComp: a 3D analysis tool for 2D woven fabric composites," *SAMPE J*, 25-33.
52. Whitcomb, J. D. 2002. “Characterization of structural behavior and properties of braided composites,” presented in *ASME Conference,* Nov. 2002.
53. Kelkar, A. D., J. S. Tate, J. D. Whitcomb and X. Tang. 2003. “Performance evaluation and modeling of braided composites,” in *AIAA Conference* 2003-1475.
54. J. N. Reddy and A. Miravete. 1995. *Practical Analysis of Composite Laminates*, ISBN # 0-8493-9401-5, CRC Press Inc, FL.

VITA

Deepak Goyal was born in India. He obtained his Bachelor of Engineering degree (with honors) in mechanical engineering from Punjab Engineering College, Panjab University, Chandigarh, India in May 2000. Before joining Texas A&M University in fall 2001, he taught a couple of undergraduate level engineering course and worked as a graduate engineer trainee in Daewoo Motors India limited. Upon completion of his master's work, he plans to pursue a PhD degree to further this research.

His permanent address is:
K. No. 15, Near TV Tower,
Model Town,
Bathinda (Pb) – 151001
INDIA.
Phone: (91)-164-2218853
e-mail: dee@tamu.edu
anndee108@yahoo.com